Master thesis in Hydroacoustics

Investigation of the possibilities for seabottom characterization using echosounder data

Anja Heggen

Department of Physics and Technology
University of Bergen
November 2009

Acknowledgements

First of all I want to thank my supervisor Halvor Hobæk for always taking the time to answer my questions and helping me out whenever I needed help in the laboratory. I also want to thank lecturers and fellow students in the acoustics group for two great years, both educationally and socially. Especially, I want to thank fellow student Espen Storheim for teaching me how to use LaTeX and always being very helpful with answering any questions I had along the way. I also want to thank my good friend Ane Marte for proofreading this thesis, making sure that the commas were in the right places and the sentences understandable. Last but not least, my family and Paul Robert deserve thanks for their unfailing love and support, keeping my motivation up to get through the process of writing this master thesis, which admittedly seemed to be an impossible task at times.

Contents

Chapter 1

Introduction

1.1 Objective

This thesis focuses mainly on using the information present in the first echo returned from the seafloor, using a normal-incidence echosounder, to characterize or classify the seabed. This is done using a monostatic setup in a water-tank in the laboratory. Monostatic means that the same transducer is used both as source and receiver. Starting out with looking at the returned echo from a perfect reflector metal plate, the next step was to measure the response from known bottom types, like sand and clay, to see how this affected the returned signal. Looking at the basic principles of scattering from surfaces, and doing measurements in a controlled laboratory environment, one wanted to look into the possibilities of characterizing the bottom. The returned signal is amongst other things dependent on water-depth, e.g. the distance between the seafloor and the transducer. This is an artifact that have nothing to do with the specific seabed type. Hence, another objective was to look at how the changing of depths can be compensated for.

1.2 Background and motivation

Up until acoustic techniques were introduced after World War I, water-depths were measured using a leadline. The hydrographers operating the leadline always had a feel for what type of seabed was underneath, based on the responsiveness of the line as the lead struck the bottom [1]. The bottom type was therefore often written down next to the water-depth. As acoustic techniques for determining the water-depth became available, less emphasis was put on bottom classification. In recent years however, advances in technology have made it possible to develop acoustic methods for classification of the bottom. The motivation for this work is that it is cost-efficient in terms of both time and effort compared to other methods, like using divers or analyzing bottom grabs or core samples, as the sediment type can change dramatically even over short distances. Large-scale acoustic mapping of the seabed and marine habitat started in the late 1970s throughout the world [2]. The applications for acoustic classification of the seabed are many, including [3]:

- pipeline and cable layout

- oil rig site investigations

- military operations, i.e. mine hunting

- habitat mapping and protection

- dredging of harbours and channels

Sound propagation in shallow water (less than 200 m depth) is highly influenced by sediment type, due to repeated interaction with the seabed. Hence, knowledge of the sediment types in the area is important for prediction of propagation loss or acoustic backscatter [4]. When searching for targets on or buried in the ocean bottom, knowledge of sediment type is also of importance, as this is the dominating masking reverberation against which the target must be detected.

A single-beam echosounder is standard equipment on most vessels. However, single-beam echosounders only provide information of the seabed immediately below the surveying vessel. The area insonified is called the sonar footprint [2]. The size of the footprint depends on the distance beetween the transducer and the seabed, the local slope of the seabed and the beam-width of the transducer. Other traditional techniques for acoustic mapping of the seabed include multibeam echosounders and sidescan sonars [2]. These systems cover more area than the single-beam echosounder. However, they are complementary to the single-beam echosounder, and these three instruments are generally used in combination. Multibeam systems principally give a general overview of the bathymetry (water-depth) and topography (surface shapes and features) of the seafloor, while sidescan sonars show smaller features of the topography generally at higher frequencies.

The signal from a single-beam echosounder, returning to the transducer after interaction with the seafloor, is amongst other things dependent on the type of seafloor sediment. Therefore, analysis of the shape and energy characteristics of the returned signal can be used to determine the sediment type [4]. Because of the high frequency ranges used by most single-beam echosounders, this method usually just gives the sediment type of a thin surface layer of the seabed, due to the high amount of absorption in the sediments at these frequencies. Analysis of the returned signals obtained by echosounders at sea, have been done with varied results. To do the analysis, acoustic 'bottom classification devices' have been developed. Examples of such systems are QTC-View and RoxAnn. These devices can be mounted onto the echosounders on boats, without disturbing the regular operation of the echosounders [3]. Companies developing these systems, regard their processing as proprietary. Hence, the algorithms used for classification are more or less unknown, and methods vary from one manufacturer to another [4]. These methods are also dependent on calibration of the specific echosounder to be used over known sediment types, a process called ground truthing. This can be done by physical sampling, bottom grabs or core sampling, or by observations done by divers or underwater cameras. These bottom classification methods are therefore empirical and not absolute. Classification, using these systems, can be done in one of two ways:

- Supervised classification method: Best fit of a dataset to a ground truthed model. This means that the specific echosounder is calibrated over known sediments before the classification process starts.

- Unsupervised classification method: Automated classification process which uses implemented algorithms to group similar echo signatures together, called clustering. The analyst must then determine whether the number of different groups is realistic and what type of bottom each group represents [1]. The latter can be done by taking bottom samples at representative sites within each classification zone.

While seabed classification is the organization of the seafloor and direct subsurface into seabed types or classes, e.g. mud, silt, gravel and sand, seabed characterization is a more accurate method as it attempts to extract information about the actual geoacoustic parameters of the seafloor, e.g. grain size, roughness, sound speed, attenuation, etc. As mentioned, classification is empirically based, which means that it simply relies on the observation that certain features of the echo signals are correlated with the sediment type [5]. The idea behind the use of a particular feature may be based on theoretical assumptions, but this theory is not used in the

signal processing or classification. In characterization of the seabed, values of the different parameters of the bottom are determined using a theoretical, physical model [6]. Either the features of the measured data can be used directly for estimation, or the measured data can be compared with data generated by a numerical model and the optimal parameter set can be found through a global search. The latter characterization method is called inversion [6].

The returned echo from the seafloor is dependent upon different parameters, which make the tasks of classification and characterization more complex. It depends not only on bottom parameters, such as roughness, density, sound speed and attenuation, but also on source characteristics, like pulse characteristics (shape, spectrum, and duration) and directivity pattern, and the distance between the transducer and the seafloor surface [7]. For this reason, the calibration or ground truthing needs to be done with the specific echosounder system that is going to be used for classification. It is also important to find a method to compensate for the changes in the signal due to changing water-depths. Pouliquen [8] has done some work on compensating for depth, which will be discussed later.

The theory of acoustic scattering is well understood, however, applications in complex, real-world environments often reveal the limits of scattering models [9]. In characterization of the geological properties of the seabed, there is currently no single model that can describe the seabed unambigously only from its acoustic characteristics, as features of the acoustic response may have more than one explanation [9]. Difficulties include ping-to-ping variability, and the identification of which echo parameters are best suited to discriminate between various seafloors [5]. Looking closer at the theoretical basis of scattering from surfaces, and doing measurements of scattering in a controlled laboratory environment, might give new insights. In addition, this work was inspired from the personal contact with Ms. Noela Sánchez-Carnero at University of Coruña, Spain, and Dr. Victor Espinosa at University of Valencia, Spain.

1.3   Previous Work

There seem to be an endless amount of literature on the subjects of characterization and classification of the seabed, and a lot of different methods to go about this have been proposed. It has been impossible in the timespan of this master thesis to get an overview of all the literature in the field, as well as to take a closer look at all of the different methods and theories. However, a few of the works that were found and looked into are mentioned below.

In the book High-Frequency Seafloor Acoustics [10], the authors have reviewed data collected from different published studies, where monostatic setups were used. This work shows that backscattered strength from the ocean floors (e.g. sand, mud and rock) depends on grazing angle by Lamberts law for angles less than 60°. However, for the specular and close to specular directions, the value of the backscatter has a higher value than that obtained using Lamberts law, which shows that scattering from these seafloors is not entirely diffuse. It is concluded that scattering strength is not a good classification factor alone, as the variation in echoes from the same seabed type is almost as large as, and in some cases larger than, the variation amongst different seabed types.

Pouliquen *et al.* [7] also emphasize the point that total or average backscattering strength, which have been measured and modelled for many years from different seafloors, show no consistency. They claim that a detailed study requires observation of the whole time series of the backscattered signal, because the total backscattering strength depends on which component dominates the scattering. The authors have developed a time-domain model for the acoustic seafloor backscattering that generates the raw pressure time series separately for the volume and surface echoes. This time-domain model is based on the Kirchhoff approximation to the Helmholtz-Kirchhoff integral equation of wave scattering from random rough surfaces and on the Small Perturbation theory for the seafloor volume.

Different scaled tank experiments have been conducted at the University of Bath during the last decades, to look at seabed and target scattering at high frequencies. Some of these experiments are summarized in an article written by Blondel and Pace [9]. The experiments include acoustic propagation and penetration in sediments, monostatic imaging and the influence of seabed parameters on the full scattered waveform, and bistatic imaging geometries looking at the relative influence of seabed types and different targets. The authors discuss the physical parameters that need to be scaled in such experiments, like the transmission frequency (or acoustic wavelength), the signal propagation, and the signal scattering on sediments (e.g. grain size). In one of the monostatic experiments the backscattering coefficients from three types of marine sediments were measured for different grazing angles. These measurements moderately coincided with predictions based on the Helmholtz-Kirchhoff integral, and showed that volume scattering is not particularly significant for high-frequency scattering from coarser sediments (e.g. gravel).

Pouliquen and Lurton [11] use a comparison between measured and theoretically modelled echo patterns in the time domain to classify the bottom. The reference signals are calculated for a given transducer and a set of different water-depths and bottom types, using a theoretical model based on the Kirchhoff approximation for both interface and volume contributions. The authors found that the total energy of the returned signal was not a good discriminator, due to signal variation for a given bottom type. However, the envelope shape was found to give a better characteristic of the sediment type. The time integral of the amplitude normalised with the total energy of the echo was used, and the average of several echoes was compared to the theoretical signal envelopes.

Berntsen *et al.* [6] argue that a model based method should be used in characterization and classification of the seabed, to properly account for the environmental conditions (e.g. water-depth) and the actual sonar system used (e.g. beam-width and frequency). The authors use a method based on the properties of the coherent backscattered time signal to characterize the seabed, and therefore stacks (i.e. align and average) the echo signals from many different randomly rough surfaces to reduce the incoherent field. Kirchhoff theory is used to find an analytical expression for the mean scattered field (i.e. coherent field) for a surface that has Gaussian roughness statistics. The authors then use the frequency-shift of the coherent signal to estimate the roughness of the seabed, and further use the analytical expression to estimate the impedance of the seafloor. This method is further discussed in section 3.2.3. The work is done using a parametric sonar, which emits two primary beams at frequencies close to each other. A secondary beam at the difference frequency, as well as one at the sum frequency, are then generated in the water column. The difference frequency beam has the advantages of: no side-lobes, a narrower beam than can be achieved by direct generation of the difference frequency at the same physical size, broad bandwidth and near constant beam-width over a broad frequency band. The authors claim that these properties are essential for the characterization method used in their work. Since the coherent signal is used, the method is limited to low-frequency signals and near normal incidence. However, a suggestion is made that these limitations might be reduced by including the effects of the incoherent scattering in the estimation technique. The authors found that the estimation technique worked well on simulated data, and concluded that it seemed to work well for field data as well. Work on field data was however still in progress.

Biffard *et al.* [12] have surveyed methods of removing the artifacts of the echoes caused by properties that have nothing to do with the actual seabed properties, like water-depth, system parameters and seabed slope, while discussing methods for seabed classification. In this work, field data and simulations attained by the time-domain model developed by Pouliquen *et al.* [7], referred to as BORIS, are presented. Again, using the frequency shifts of the echo signals for rough surfaces, with respect to the transmitted signal, is mentioned as a method

for characterization. It is concluded that the distribution of the frequency shifts in field data indicates useful sediment discrimination, however, the ground truth available was uncertain and therefore not compared to these field data. In this work phase-alignment and averaging of echo signals are discussed. Phase-matching, either by cross-correlations of the region near the bottom pick or rising zero-crossings within one cycle of the bottom pick, is proposed. But both techniques were found to enhance the coherent amplitude at moderate to high roughness for BORIS data. Further, it is claimed that the shape, duration and relative strengths of the coherent and average incoherent echoes are strong indicators of seabed roughness, and therefore that full-waveform stacking has potential for seabed classification. A method to compensate for depth on echo shapes and durations, is to adjust the length of the transmit pulse proportional to the depth of the previous ping. This is a method discussed by Pouliquen [8]. Biffard *et al.* express that they do not know of any commercial echosounder that allows this degree of control over the pulse length. On the contrary, Pouliquen claims that this function is available in most commercial echosounders. Rolf Korneliussen at the Norwegian Institute of Marine Research could tell us that Simrad echosounders allow adjustment of the pulse length by a factor two.

In work done by van Walree *et al.* [5], features extracted from echosounder bottom returns are compared with the ground truth in a North Sea survey area. Echo envelopes are analysed for two single-beam echosounders, at frequencies of 66 kHz and 150 kHz, and it is shown that a set of six energetic, statistical, spectral and fractal parameters carries useful information that can be used in characterization or classification of the seabed. A quantitative comparison of the individual parameters with the mean grain size, where four different sediment classes were examined, revealed significant correlations. The 150 kHz transducer was found to provide better discrimination between main sediment types. Some of the parameters mentioned in the work by van Walree *et al.* have been calculated for the echo data collected in this master thesis, and will be discussed later.

Tegowski and Lubniewski [13] calculated spectral moments for echo pulses acquired in the Southern Baltic Sea. They found that the spectral width, which gives a measure of the spectral power density around the dominant frequency, could be used to describe the structure of sediment layers. The echo parameters spectral width, spectral skewness and fractal dimensions were used for classification by application of cluster analysis.

1.4 Thesis Outline

The background and motivation for this thesis have been presented, and a short outline of the thesis follows here. The results of each of the sets of measurements are discussed in the respective chapters and the main points are then discussed in the concluding chapter.

Chapter 2 deals with different concepts that are relevant for the work in this thesis. First the piston source model is outlined, and then reflection of plane waves at plane boundaries is discussed. Further, more specific topics are brought up; the basic concepts of scattering of sound from the seafloor and echo-prolongation as a function of depth. Also a short discussion of the Hilbert transform is included.

Chapter 3 goes further into the discussion of scattering from surfaces. Reflection of sound from a plane reflector is considered, and a physical model for calculation of the backscattered signal from a plane reflector, based on the Helmholtz-Kirchhoff integral, is outlined. This model is further used to simulate the pressure field from a plane reflector and look at the increase in echo duration as a function of depth. Further, scattering from random rough surfaces is looked into.

Chapter 4 discusses the experimental setup used for the measurements done in this work. It also includes measurements done to find the properties of the transducers. A method of

finding the impulse response of the transducers is considered, so that the simulated pressure signals, found by the physical model discussed in chapter 3, can be compared to the electrical measured signals. In addition, the methods used for stacking signals, i.e. phase-aligning and averaging, to account for signal fluctuation is discussed. The intensity curves of the signals are also mentioned in this chapter.

Chapter 5 deals with the measurements from the copper reflector. While only the first of these measurements were taken before measuring on sand and clay, the later copper reflector measurements are also discussed here. The measurement setup is explained and then the results are summarized and discussed.

Chapter 6 deals with measurements from different sand surfaces: fine sand, coarse sand and gravel. Two different transducers were used for these measurements. Both individual and stacked signals are considered here. Also depth correction steps to make the echoes depth independent are applied to some of the data from the sand surfaces in this chapter.

Chapter 7 discusses the measurements from the clay surface. Again, the setup is outlined before discussing the results of the measurements. Both individual and stacked measurements are considered for the clay surface.

Chapter 8 considers different echo parameters based on energy statistics and spectral moments that are mentioned in the literature. These are calculated for some of the intensity and pressure echo envelopes from the different sediment surfaces, and the results are discussed.

Chapter 9 summarizes the main results in this work, and discusses ideas for further work related to classification and characterization of the seabed.

Appendix A deals with uncertainty calculations. Expressions for the uncertainties in the effective angle and effective burst lengths discussed in chapter 2 are found and the uncertainties in the directivity measurements are discussed.

Appendix B outlines the Helmholtz-Kirchhoff theorem following [14]. It was left out of Chapter 3, and is included here instead.

Appendix C contains the MATLAB-scripts used in this work, both for communication with instruments, control of the motor system and calculation of different parameters.

Chapter 2

Background theory

2.1 The piston source

The piston source model is often used to model the sound field of a transducer. A piston, with radius a, is mounted on a flat rigid baffle of infinite extent. The radiating surface of the piston oscillates uniformly with speed $U_0 e^{i\omega t}$ in the z-direction, see figure 2.1 [15].
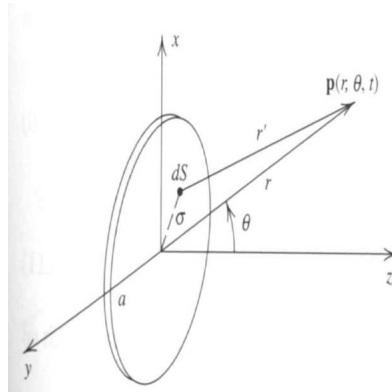
Figure 2.1: Geometry used in deriving the acoustic field of a baffled circular plane piston, copied from [15].

The pressure at any given field point can be found by the equation

$$\mathbf{p}(r, \theta, t) = i\rho_0 c \frac{U_0}{\lambda} \int_S \frac{1}{r'} e^{i(\omega t - kr')} \, \mathrm{d}S, \tag{2.1}$$

where ρ_0 is the density of the acoustic medium, c is the soundspeed in the acoustic medium, U_0 is the amplitude of the speed at which the piston surface is vibrating, λ is the wavelength of the sound in the acoustic medium, $\omega = 2\pi f$ is the angular frequency at which the source is vibrating and r' is the distance from the infinitesimal element $\mathrm{d}S$, on the piston surface, to the field point. The integral is taken over the region $\sigma \leq a$. This integral is difficult to solve for general field points. However, for two regions closed-form solutions can be found, namely on the acoustic axis (the z-axis in figure 2.1) and in the far field.
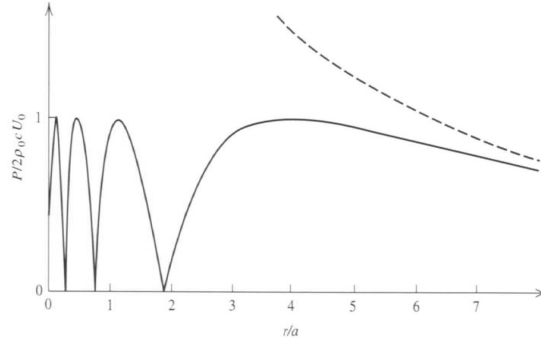
Figure 2.2: Axial pressure amplitude for a baffled circular plane piston of radius a radiating sound of wave number k with $ka=8\pi$, copied from [15].

On the acoustic axis in the near field, the amplitude fluctuates due to interference effects, while in the far field the acoustic pressure amplitude decreases monotonically, approaching a $1/r$ dependence, as seen in figure 2.2. The solid line is calculated from the exact theory, while the dashed line is the far field approximation extrapolated into the near field. In the far field of a piston source, the closed-form solution of the integral in equation (2.1) is given by [15, 16]

$$\mathbf{p}(r,\theta,t) = \frac{i}{2}\rho_0 c U_0 \frac{a}{r} ka \left[\frac{2 J_1(ka \sin(\theta))}{ka \sin(\theta)} \right] e^{i(\omega t - kr)}, \tag{2.2}$$

where J_1 is a Besselfunction of the first kind and first order, θ is the angle away from the acoustic axis and k is the wave number. The amplitude of the sound pressure can be divided into two parts, one giving the pressure amplitude on the acoustic axis and one containing the angular dependence

$$|\mathbf{p}(r,\theta)| = P_{ax}(r) D(\theta) = \frac{\rho_0 c k a^2 U_0}{2r} \left[\frac{2 J_1(ka \sin(\theta))}{ka \sin(\theta)} \right]. \tag{2.3}$$

The pressure is largest on the acoustic axis, $\theta = 0$, where the expression giving the angular dependence equals 1. Pressure nodes are located at angles θ_m, given by $ka \sin(\theta_m) = j_{1m}$, where $m = 1, 2, 3, \dots$. j_{1m} are values of the argument J_1 which reduce the Besselfunction to zero, $J_1(j_{1m}) = 0$. These values can be looked up in tables, for example in reference [15]. Figure 2.3 shows an example where pressure nodes are located at angles $22.5\,^\circ$ and $44.5\,^\circ$.
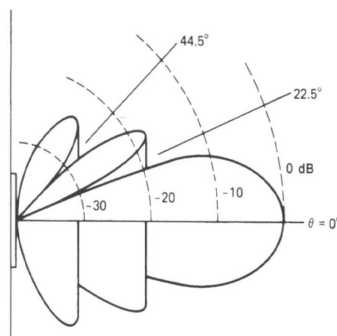

Figure 2.3: Beam-pattern for a circular plane piston of radius a radiating sound with $ka = 10$, copied from [15].

Pressure lobes are located between the nodal surfaces. The angular locations and relative strengths of the acoustic pressure maxima in these lobes are given by the relative maxima

8

of $D(\theta)$ [15], and therefore depends on the relationship between the wavelength of the sound compared to the radius of the source. When the wavelength is much smaller than the radius, $ka \gg 1$, the beam-pattern will have many sidelobes and a narrow main lobe. When the wavelength is of about the same size as the source radius, however, the main lobe will have a larger angular width, and there will be fewer sidelobes.

Assuming that most of the sound energy is located in the main lobe, one can use the angular width of this lobe as a measure of how large an area of the seafloor will be insonified at a given water-depth. When referring to the beam-width of the transducer, different angles can be used as a reference, for example the θ_{-3dB} angle, which specifies the angle at which the intensity has dropped to half the value of the intensity on the acoustic axis. However, in this work the angle of the first minima is used as a measure of the transducers beam-width. This is found using equation (2.3), looking up the table value for j_{11}. This gives the half angle of the beam, which has to be multiplied by two to find the total beam-width.

Due to the fluctuating amplitude in the near field, it is important to do the measurements in the far field. One can be certain of being in the far field when one is located at a distance from the source greater than the Rayleigh distance for the particular transducer. This distance is given by $R = A/\lambda = \pi a^2 f/c$, where a is the radius of the source, f is the frequency at which the piston is driven, and c is the soundspeed in the acoustic medium.

2.2 Plane wave reflection at a plane boundary

When an acoustic wave encounters a boundary between two media, reflected and transmitted waves are generated. A simplified situation is to look at this problem for plane waves, hitting an infinite plane boundary, where the media on both sides are fluids. The pressure amplitudes and intensities of the reflected and transmitted waves, relative to the incident wave, depend on the characteristic acoustic impedances and speeds of sound in the two media, and also the angle of incidence of the incoming wave. The angle of incidence is defined as the angle between the incoming wave and the normal vector of the plane surface. The characteristic acoustic impedance of a fluid media is given by $z = \rho c$, where ρ is the equilibrium density of the fluid and c is the soundspeed in the fluid.

The incident, reflected and transmitted waves, can be expressed by [15, 17]

$$P_i = A_1 e^{i(k_1(x \cos \theta_i + y \sin \theta_i) - \omega t)}, \tag{2.4}$$

$$P_r = B_2 e^{i(k_1(-x \cos \theta_i + y \sin \theta_i) - \omega t)}, \tag{2.5}$$

$$P_t = A_2 e^{i(k_2(x \cos \theta_t + y \sin \theta_t) - \omega t)}, \tag{2.6}$$

where A_1, B_2 and A_2 are the amplitudes of the respective waves, while θ_i, θ_r and θ_t are the angles of the respective waves from the surface normal. The three waves have to satisfy certain conditions on the boundary between the two fluids:

1. Continuity of pressure: The interface itself has no mass (to accelerate), hence the forces on one side of the boundary must be balanced by the forces on the other side of the boundary.

2. Continuity of the normal component of the velocity: At the boundary the same fluid particles are in contact at any given time, no vacuum is created.

For oblique incidence, the directions of the waves must be known in order to apply the second condition. The directions can be found by considering that the phases of the three waves must move at the same speed along the boundary. This consideration shows that the angle of

reflection equals the angle of incidence ($\theta_r = \theta_i$, specular reflection), while the direction of the transmitted wave is given by Snells law

$$\frac{c_1}{\sin \theta_i} = \frac{c_2}{\sin \theta_t}, \tag{2.7}$$

where c_1 and c_2 are the soundspeeds in media 1 and media 2 respectively. Application of the boundary conditions, using the expressions for the three waves, yields the Rayleigh coefficient of reflection, as well as the coefficient of transmission [15, 17]

$$\Re = \frac{z_2 \cos \theta_i - z_1 \cos \theta_t}{z_2 \cos \theta_i + z_1 \cos \theta_t}, \tag{2.8}$$

$$T = \frac{2z_2 \cos \theta_i}{z_2 \cos \theta_i + z_1 \cos \theta_t}. \tag{2.9}$$

2.3   Scattering of a sound pulse from the seafloor

A normal-incidence echosounder transmits a pulse of soundwaves, of a certain length and at a known frequency towards the seabed. Compressional waves propagate spherically towards the bottom. The wavefront first hits the bottom in a point, as shown in figure 2.4 a). The area insonified then grows into a circle of increasing radius, as more of the wavefront reaches the bottom, see figure 2.4 b). When the back end of the pulse also reaches the bottom, the area insonified turns into an annulus, which increases in radius until the front of the pulse reaches the boundary of the beam-pattern, this is illustrated in figure 2.4 c). However, for a long pulse and/or a narrow beam-pattern, the front end of the pulse may reach the boundary of the beam-pattern before the back end of the pulse reaches the bottom. In this case the annulus will not have an increasing outer radius. When the front end of the pulse reaches the boundary of the beam-pattern, the footprint decreases as the inner radius expands, until the pulse completely enters the bottom, see figure 2.4 d). This consideration is based on the simplification of a well-defined, cone-shaped beam-pattern. The signal pulse length, the transducer beam-width and the water-depth determine the size of the acoustic footprint and the wavefront curvature at the sediment interface.

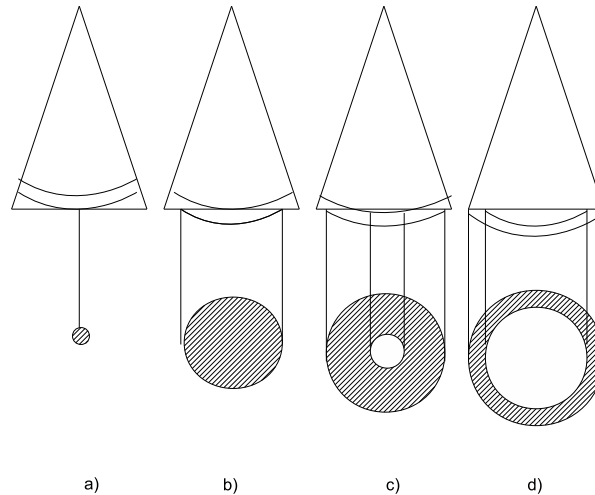a)   b)   c)   d)

Figure 2.4: Progression of the insonification of the seabed.

A fraction of the sound hitting the bottom at normal incidence is reflected back to the source, this is called the specular component. This reflected part of the return has the same

frequency content as the transmit pulse, and is therefore also called the coherent component. Due to bottom roughness some of the sound entering at an angle relative to the normal might hit facets that are perpendicular to the incoming sound, and hence also be reflected coherently back to the source [12]. In addition, the return consists of an incoherent component due to scattering by bottom roughness and from volume inhomogeneties in the sediments. The backscatter from the annuli is delayed relative to the initial bottom return. Which component(s) dominate the scatter therefore affects the shape and duration of the echo.

The coherent part of the echo is stable, while the incoherent component is chaotic due to interference effects. The incoherent component causes ping-to-ping variability, which masks echo shape and other characteristics that can be used to discriminate among seabed types. Here stacking full-waveform echoes, aligning and averaging, is the usual remedy. In the stacking process the 'random-walk' phases of the incoherent component average out, leaving the coherent component of the signal. Envelope stacking is a traditional technique for improvement of signal variability, however, compared to the full-waveform stacking, this technique does not reduce the incoherent component, but rather expresses the sum of the coherent and incoherent components [12]. The echo envelopes can be found by the absolute value of the Hilbert transformed echo time series. By stacking the full-waveform series and then finding the envelope, the average coherent amplitude can be found. Stacking the envelopes give the total amplitude, hence by subtraction it should then be possible to also find the amplitude of the incoherent signal. This method is used by Biffard *et al.* [12] to find out whether the coherent or the incoherent component dominates the scattering process from surfaces of different roughness.

2.4 Echo-prolongation as a function of depth

As already mentioned, characteristics of the returned echo from the seafloor is also dependent on water-depth, the distance between the source/receiver (in a monostatic case) and the seafloor. Changes in water-depth influence both shape and power of the returned signal due to spreading losses and absorption, and also leads to a prolongation or compression of the returned ping. Due to the constant beam-pattern of the transducer, a larger portion of the seafloor is insonified at larger water-depths. The sound backscattered at a certain time does not come from the same area for different water-depths, as the radii of the insonified annuli changes with depth. These effects will obscure the changes that are due to variation in the sediment type, and therefore a transformation to a reference water-depth is necessary before analyzing the echo [4]. For transformation to a reference water-depth, both time and power adjustments of the returned signals need to be made.

Changes in water-depth cause changes in start time and duration of the returned ping. This can be seen looking at the following geometrical consideration. It should be noted that this consideration is done for a flat seafloor, with no penetration into the bottom.

Figure 2.5: Geometric consideration of how different water-depths affect the ping length of the returned signal.

Assume a vertical sound beam with a half-angle beam-width θ, e.g. the -3 dB angle, as shown in figure 2.5. A burst of length D [mm] is transmitted perpendicularly down towards a flat bottom. As the center of the leading spherical wavefront first hits the bottom (point A in the figure), the outer part of the beam still has a distance Δ_1 to go before reaching the bottom. If the distance between the transducer and the bottom was even larger, the corresponding distance would be Δ_2. Therefore, an expression for the time taken to insonify the seafloor to the specific angle, e.g. θ_{-3dB}, after the start of the ping first hits the seafloor, is given by

$$\Delta t = \frac{\Delta}{c}, \tag{2.10}$$

where c is the speed of sound in water, while Δ is the additional path length for the outer part of the beam, which increases with increasing water-depth. This path length, Δ, can generally be expressed as

$$\Delta = \frac{r}{\cos \theta} - r = r \left(\frac{1}{\cos \theta} - 1 \right) = r\alpha, \tag{2.11}$$

where r is the vertical distance from the transducer to the seafloor bottom. Since θ is a constant for a given transducer, so is α. The return path back to the hydrophone will have the same delay. In addition, the echo duration will be dependent upon the initial pulse length, as the back end of the pulse will be delayed relative to the front end, by the burst length, D. Thus, the total duration of the returned echo is given by

$$\Delta T = \frac{D}{c} + \frac{2\alpha}{c} r. \tag{2.12}$$

Therefore, $\frac{\mathrm{d}(\Delta T)}{\mathrm{d}r} = \frac{2\alpha}{c}$ is a constant, and the duration of the returned signal from a flat bottom is a linear function of water-depth. This consideration assumes that parts of the beam entering at an angle away from the normal is reflected or scattered back to the transducer, that is not all of it is specularly reflected away from the transducer. Also, the scatter from the seabed volume is not accounted for here. In reality, the duration of the echo is not necessarily a linear function of water-depth.

12

2.4.1 Transformation to a reference water-depth

In the Acoustic Bottom Classification System (ABCS) program [4], a time adjustment is first made to account for the different path lengths traversed by the pulse for different depths, and then a power adjustment is made to account for the different amount of spherical spreading. Absorption of the echosounder ping occurs as it passes through the water. The amount of absorption is dependent on temperature, salinity and frequency, and also on the distance travelled by the pulse. The effect of absorption is small if the distance travelled by the first return of the echosounder ping is short [4].

Pouliquen [8] describes three steps required to make the echoes quasi depth-independent. The first two steps are the same steps mentioned above, namely time-scaling and power adjustment of the echoes. Time-scaling is done by bringing the echoes recorded at depth r to a reference depth H such that

$$t_0 = t\frac{H}{r}, \tag{2.13}$$

where t is the original time vector, while t_0 is the new time vector at the reference depth. This leads to a prolongation of echoes recorded for shallower depths than the reference depth, and a compression of echoes recorded for deeper depths than the reference depth. For the same seabed properties, the time-scaled echoes will then have the same length, while preserving the angular dependence of interface scattering [8]. In addition, Pouliquen suggests a third step, which needs to be applied before processing. That is to linearly increase the pulse length, τ, of the transmitted burst as depth increases, such that

$$\tau = \tau_0\frac{r}{H}, \tag{2.14}$$

where τ_0 is the pulse length used at the reference depth H. The pulse length scaling also preserves the angular dependence of interface scattering. Pouliquen tested these depth correction steps on simulated signal envelopes, and found that the first two steps were not sufficient to make the echoes aqcuired at different detphs equal. However, after application of the third step there was just a slight difference in echo shape for the echoes acquired at different depths. This difference is explained by the effect of macro-roughness, which does not increase linearly with depth, and by the fact that the correction steps are applied to the volume component of the scatter assuming no penetration into the seabed.

The equation for the total echo duration at a given depth, equation (2.12), can be written as

$$\Delta T = \frac{D}{c} + \frac{2\alpha}{c}r = \tau + 2\alpha t, \tag{2.15}$$

since $D/c = \tau$, i.e. the pulse length, and $r/c = t$, i.e. the time it takes for the burst to reach the bottom. Using Pouliquens correction steps for the time-scaling of the echoes and the pulse length adjustment, this expression turns into

$$\Delta T = (\tau_0 + 2\alpha t_0)\frac{r}{H} = \Delta T_0\frac{r}{H}, \tag{2.16}$$

where ΔT_0 is the echo duration at the reference depth. Under these assumptions, the echo duration at a given depth ΔT, can be scaled to

$$\Delta T_0 = \frac{H}{r}\Delta T. \tag{2.17}$$

2.4.2 Finding the effective angle and the effective burst length

Using the envelope of the reflected pulse, by Hilbert transformation of the time signal, the effective duration of the echo can be found. In the comparison here one has to consider that

the transducer also has a receiver directivity. If the transducer is assumed to be reciprocal, the directivity on reception is the same as the directivity on transmission. Hence, it is assumed that the total directivity can be expressed as $D_i D_r = D^2$. If one looks at the beam transmitted within the angle θ_{-3dB}, on reception the signal at this angle is reduced to the -6 dB level, and the signal within this angle should therefore lie between the 0 dB and -6 dB levels. The -6 dB level of the signal envelope can then be used as a measure for the effective duration of the returned echo, see figure 2.6. Likewise, the -14 dB level should be considered when one is interested in the beam transmitted within the -7 dB angle.
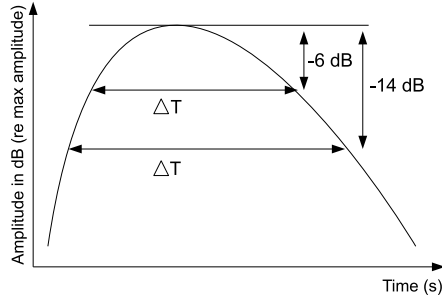

Figure 2.6: Finding the effective burst length.

Measuring the echoes at different water-depths, and then plotting the duration of the echoes (in seconds) versus water-depth (in meters), both the effective burst length, D, and the effective angle, θ, can be determined. The method of least squares to a line was used to find the linear relationship from the measurements, and thereby the coefficients in equation (2.12), where the offset is given by $b = D/c$, and the gradient is given by $m = 2\alpha/c$, see figure 2.7.
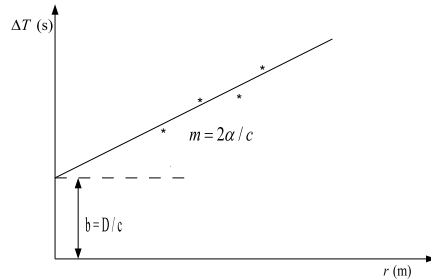

Figure 2.7: Relation between ΔT and water-depth.

For the two coefficients m and b we find the following standard deviations [18]

$$s_m = s_y \sqrt{\frac{n}{n\Sigma x_i^2 - (\Sigma x_i)^2}},\qquad(2.18)$$

$$s_b = s_y \sqrt{\frac{\Sigma x_i^2}{n\Sigma x_i^2 - (\Sigma x_i)^2}},\qquad(2.19)$$

where n is the number of samples, x is the specific water-depths where samples are collected, and s_y is the standard deviation of the measured echo durations from the fitted line, given by [18]

$$s_y = \sqrt{\frac{\Sigma(y_{\text{meas}} - y_{\text{fit}})^2}{n-2}}\qquad(2.20)$$

Here, the uncertainty in reading out the measured echo durations from the envelope plots are not considered. Some of the signal envelopes fluctuates more than others around the pressure levels considered. This leads to different uncertainties for the different depths, as well as for the different surfaces. This uncertainty could possibly be included by weighting the measurement points in the method of least squares, so that the points with the larger uncertainties are of less importance than the points with lower uncertainties when the linear graph is found. However, this was not done for the measurements in this master thesis. When the uncertainties in the echo durations were small compared to the distance between the measurement points and the linear graph, this uncertainty was assumed to have negligible effect on the coefficients calculated. When these uncertainties were large however, the coefficients were estimated by drawing two lines by hand that had the largest and smallest gradients possible, while still fitting with the measurement data including uncertainties. The mean of the coefficients for these two lines were then used to draw the linear graph. The uncertainty of the coefficients from the equations (2.18) and (2.19), as well as the uncertainty found from the difference in the coefficients for the two lines drawn, were then used to estimate the uncertainties in the coefficients of the linear plot. The uncertainty in the effective burst length D, the coefficient α and the effective angle θ could then be found from standard formulas for uncertainty, see appendix A.1.1.

2.5 The Hilbert transform

Examining the original time signal can be difficult due to the high-frequency components in the signal. Hilbert transformation of the signal make the process easier by removing high-frequency components, leaving the envelope of the received signal when the magnitude of the transformed signal is considered. The Hilbert transform of the signal is useful in finding the maximum amplitude of a time signal, as well as finding the time intervals where the signal is above a certain amplitude level relative to the maximum amplitude of the signal, e.g. the -6 dB level.

The Hilbert transform of a full-waveform echo gives a complex time series where the real part is the echo and the imaginary part is 90° phase-shifted [12]. This is called the analytic signal, since it contains no negative frequency components. The magnitude of the transformed signal, at any particular time, is the instantaneous amplitude. There is no delay and the echo bandwidth is preserved.

For a real time signal the definition of the Hilbert transform is given by [19]

$$\mathscr{H}[x(t)] = \overline{x}(t) = \frac{1}{\pi} \int_{-\infty}^{\infty} x(\tau) \frac{1}{t - \tau} \, \mathrm{d}\tau = \frac{1}{\pi t} * x(t) = h(t) * x(t). \tag{2.21}$$

The term transform is a bit misleading, as it is simply a convolution of the time signal with an impulse response, hence the domain after the transformation is still the time domain. The domain is not changed as it is when a Fourier transform or Laplace transform is used.

In this master thesis the Hilbert transform of the signals have been found using MATLAB. The signal envelopes were then found by plotting the dB value of the magnitude of the Hilbert transform, relative to the maximal amplitude.

Chapter 3

Scattering from surfaces

Intuitively, the first part of the returned signal from the seafloor at normal incidence should be contribution from the seafloor surface, the specular component reflected from the bottom. While contribution from scatterers in the seafloor volume and incoherent backscatter contributions from the surface, should affect the tail of the echo more. However, it is not possible to separate these two contributions with a time-cutoff approach. Also, one would expect a stronger echo signal from a hard bottom versus a softer bottom, due to the greater difference in characteristic impedance between the water and the sediment. However, surface roughness and volume inhomogeneties also need to be considered here [7]. A soft bottom with significant bottom roughness, could give a stronger echo than a smooth hard bottom. When the seafloor is smooth, it is mainly the beam near the normal direction that is reflected back to the transducer. However, for a rough bottom the pulse is reflected and scattered in several directions, hence the total energy at the transducer upon reflection may be larger than for a smooth bottom.

3.1   Reflection of a soundburst from a plane reflector

An attempt was made to model the return from a plane reflector, for comparison with the measured signal from the copper reflector.

In the far field, the sound pressure amplitude radiated from a plane sound source in a homogenous, isotropic fluid medium, can be written as a product of a factor dependent on the distance from the source on the acoustic axis and a factor dependent on the direction, as discussed in the piston source model in section 2.1

$$|p(\mathbf{r}, \theta)| = P_{ax}(r)D(\theta). \tag{3.1}$$

If the source is assumed to radiate sound in a circular symmetrical fashion about the sound axis, the directional factor can be expressed by

$$D(\theta) = \frac{2J_1(ka\sin(\theta))}{ka\sin(\theta)}, \tag{3.2}$$

where J_1 is the Besselfunction of the first kind and first order. In the far field the pressure amplitude along the sound axis varies according to the relation $P(R) = B/R$, when absorption is neglected. Here, r is replaced by R so as not to be confused with the distance vector $\mathbf{r}$ introduced in the next subsection, while B is a range independent constant, which can be determined by finding the pressure amplitude p_A, at a reference distance A from the transducer. Hence, in the far field the amplitude is inversely proportional to the distance from the source, as is the case for a spherically diverging wave. The incident soundwave on the reflective plane

17

can then be expressed as

$$p_{inc} = p_A \frac{A}{R} D(\theta) e^{i(kR - \omega t)}, \tag{3.3}$$

where k is the wavenumber and ω is the angular frequency. If the sound wave is a burst instead of a continous wave, equation (3.3) can be expressed by

$$p_{inc} = p_A \frac{A}{R} D(\theta) f(R - ct), \tag{3.4}$$

where $f(R - ct)$ also includes the modulation of the signal. The reflected field can then be found using the Helmholtz-Kirchhoff integral theorem.

The Helmholtz-Kirchhoff integral theorem is deduced in appendix B, following the method used in [14]. The Helmholtz-Kirchhoff integral is also deduced in [20] and [21], using a slightly different approach. The Helmholtz-Kirchhoff integral for a bounded medium containing no sources of sound, which is the case when sound is received and the source is not active, was found in equation (B.19), and is repeated here

$$p(\mathbf{r}) = \int_S \left(G(\mathbf{r}, \mathbf{r}_0) \nabla_0 p(\mathbf{r}_0) - p(\mathbf{r}_0) \nabla_0 G(\mathbf{r}, \mathbf{r}_0) \right) \cdot \mathrm{d}\mathbf{S_0}. \tag{3.5}$$

Here, $G(\mathbf{r}, \mathbf{r}_0)$ is the general Green's function, which is the sum of the free-field Green's function, $g(\mathbf{r}, \mathbf{r}_0)$, and an arbitrary function, $H(\mathbf{r})$, which satisfy the homogenous Helmholtz equation. The free-field Green's function is given by

$$g(\mathbf{r}, \mathbf{r}_0) = \frac{e^{ikR}}{4\pi R}, \tag{3.6}$$

where $R = |\mathbf{r} - \mathbf{r_0}|$ for a point source located in $\mathbf{r} = \mathbf{r_0}$. The free-field Green's function is a particular solution to the inhomogenous Helmholtz equation. By letting the field points $\mathbf{r_0}$ be located on the boundary of the volume, equation (3.5) becomes an integral equation that needs to be solved for the field and the normal derivative of the field on the boundary, and can be used to find the field in an arbitrary point, $\mathbf{r}$, inside the bounded volume. It should also be noted that $\nabla_0 = \partial/\partial \mathbf{n_0} = -(\partial/\partial z)\hat{\mathbf{z}}$, where $\mathbf{n_0}$ is the surface normal pointing out of the volume, while $\hat{\mathbf{z}}$ points in the opposite direction, as shown in figure 3.1.

Further, it is assumed that the volume is bounded by a plane and a hemisphere with radius approaching ∞. The pressure reflected from the boundary at infinity will not be received in finite time, and hence can be neglected. The following derivation is a modified version of the theory presented in [22]. The modification consists of replacing the assumption of $G = 0$ at the plane interface and tacitly introducing the reflection coefficient in the incident wave, with a more realistic Green's function. The final result is the same.
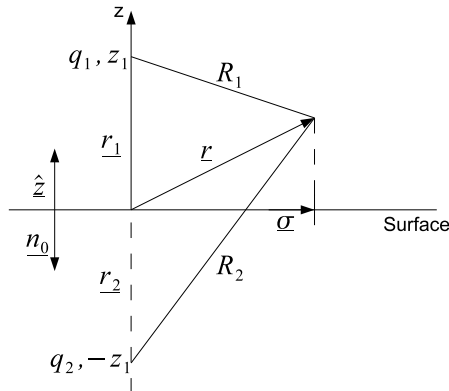

Figure 3.1: Geometry for a plane boundary, image source consideration.

In the plane the Kirchhoff approximation is used, which means that p in the integral of equation (3.5) can be replaced with p_{inc}, which is the field at the boundary if the boundary itself is not there. G and ∇G, however, have to fulfill the boundary conditions for the solution p. For a plane, perfectly reflecting surface, a mirror source of equal amplitude and phase can be placed in $-z_1$ referring to figure 3.1, leading to the general Green's function

$$G(\mathbf{r}, \mathbf{r}_1) = g_1 + g_2 = \frac{e^{ikR_1}}{4\pi R_1} + \frac{e^{ikR_2}}{4\pi R_2}, \tag{3.7}$$

where $R_1 = |\mathbf{r} - \mathbf{r}_1|$ and $R_2 = |\mathbf{r} - \mathbf{r}_2|$. $\mathbf{r}$ is a field point given by $\mathbf{r} = z\hat{\mathbf{z}} + \underline{\sigma}(\sigma, \phi)$, while $\mathbf{r}_1 = z_1\mathbf{z} + \underline{\sigma}_1(\sigma_1, \phi_1)$ is the source position and $\mathbf{r}_2 = -z_1\mathbf{z} + \underline{\sigma}_1(\sigma_1, \phi_1)$ is the image source position, see figure 3.1. If the source is placed directly above origo we get, without loss of generalisation, $\underline{\sigma}_1 = 0$, which leads to $R_1 = \sqrt{(z - z_1)^2 + \sigma^2}$ and $R_2 = \sqrt{(z + z_1)^2 + \sigma^2}$. For a point in the plane, $z = 0$, we get $R_1 = R_2 = R = \sqrt{z_1^2 + \sigma^2}$.

If the boundary is not perfectly rigid, the general Green's function must be modified. As an approximation, the general Green's function for any plane boundary can be expressed as $G = g_1 + \Re g_2$, where $\Re$ is the reflection coefficient, which is generally dependent of angle. Assuming that the reflector is located in the far-field of the source, the reflection coefficient for plane-waves, discussed in section 2.2, can be used. On the plane surface, $z = 0$, we therefore get for the general Green's function

$$G(\mathbf{r}, \mathbf{r}_1) = \frac{e^{ikR}}{R} + \Re\frac{e^{ikR}}{R} = (1 + \Re)\frac{e^{ikR}}{R}, \tag{3.8}$$

where the term $1/4\pi$ has been omitted for ease of notation. The gradients of the free-field Green's functions of the source and the image source are given by

$$\nabla g_1 = \frac{\partial}{\partial z}\left[\frac{e^{ikR_1}}{R_1}\right]\hat{\mathbf{z}} = \frac{ik\,(\partial R_1/\partial z)\,e^{ikR_1}R_1 - e^{ikR_1}\,(\partial R_1/\partial z)}{R_1^2}$$

$$= \frac{\partial R_1}{\partial z}\frac{e^{ikR_1}}{R_1}\left(ik - \frac{1}{R_1}\right)\hat{\mathbf{z}}, \tag{3.9}$$

$$\nabla g_2 = \frac{\partial R_2}{\partial z}\frac{e^{ikR_2}}{R_2}\left(ik - \frac{1}{R_2}\right)\hat{\mathbf{z}}. \tag{3.10}$$

Further, we have that

$$\frac{\partial R_1}{\partial z} = \frac{\partial}{\partial z}\left[(z - z_1)^2 + \sigma^2\right]^{1/2} = \frac{1}{2}2(z - z_1)[(z - z_1)^2 + \sigma^2]^{-1/2} = \frac{z - z_1}{R_1}, \tag{3.11}$$

$$\frac{\partial R_2}{\partial z} = \frac{\partial}{\partial z}\left[(z + z_1)^2 + \sigma^2\right]^{1/2} = \frac{1}{2}2(z + z_1)[(z + z_1)^2 + \sigma^2]^{-1/2} = \frac{z + z_1}{R_2}. \tag{3.12}$$

Since $z = 0$ and $R_1 = R_2 = R$ on the surface, we therefore get for the gradient of the general Green's function

$$\nabla_0 G(\mathbf{r}, \mathbf{r_1}) = \nabla_0 g_1 + \Re\nabla_0 g_2$$

$$= \frac{e^{ikR}}{R}\left(ik - \frac{1}{R}\right)\left[\frac{-z_1}{R} + \Re\frac{z_1}{R}\right]\hat{\mathbf{z}} = \cos\theta\frac{e^{ikR}}{R}\left(ik - \frac{1}{R}\right)(\Re - 1)\hat{\mathbf{z}}, \tag{3.13}$$

where $\cos\theta = z_1/R$. An expression for p_{inc} is given in equation (3.4), and the gradient of this expression can be written as

$$\nabla p_{inc} = Ap_A D(\theta)\frac{\partial}{\partial z}\left(\frac{e^{ikR}}{R}\right)\hat{\mathbf{z}} = Ap_A D(\theta)\frac{e^{ikR}}{R^2}\frac{\partial R}{\partial z}(ikR - 1)\hat{\mathbf{z}}. \tag{3.14}$$

On the boundary, $z = 0$, we have that $\partial R / \partial z = \partial R_1 / \partial z = -z_1/R = -\cos\theta$, and hence the gradient of the incoming field on the surface is given by

$$\nabla_0 p_{inc} = -A p_A D(\theta) \frac{e^{ikR}}{R^2} \cos\theta (ikR - 1)\hat{\mathbf{z}}, \tag{3.15}$$

or for a burst, where f includes the modulation of the signal

$$\nabla_0 p_{inc} = -A p_A D(\theta) \frac{\cos\theta}{R^2} (ikR - 1) f(R - ct)\hat{\mathbf{z}}. \tag{3.16}$$

Now, putting in all the expressions needed in equation (3.5), leads to the integral equation

$$p\left(\mathbf{r}\right) = \iint\limits_{\text{plane}} p_A A D(\theta)(ikR - 1)\frac{e^{ikR}}{R^3} f(R - ct) \cos\theta [-(1 + \Re) - (\Re - 1)]\hat{\mathbf{z}} \cdot \mathbf{n_0}\, \mathrm{d}S_0$$

$$= 2 p_A A \iint\limits_{\text{plane}} D(\theta) \Re f(R - ct) \cos\theta \frac{e^{ikR}}{R^3} (ikR - 1)\, \mathrm{d}S_0, \tag{3.17}$$

since $\hat{\mathbf{z}} \cdot \mathbf{n_0} = -1$. Assuming that the frequency spectrum of f has a narrow bandwidth, the same values for $D(\theta)$ and $\Re$ can be used for the whole frequency band of the burst. By assuming that p_{inc} is symmetric around the beam axis, the integration over $\mathrm{d}S_0 = 2\pi\sigma\, \mathrm{d}\sigma$ from 0 to ∞, can be replaced by integration over $2\pi R dR$ from z_1 to ∞, since $\sigma\, \mathrm{d}\sigma = R\, \mathrm{d}R$ from the definition of R. The term $1/4\pi$ was omitted from the Green's function, so 2π along with the factor 2 in front of the integral in equation (3.17) cancels out. Hence, the integral equation is now

$$p\left(\mathbf{r}\right) = p_A A \int\limits_{z_1}^{\infty} D(R) \Re(R) f(R - ct) \cos\theta(R) \frac{e^{ikR}}{R^2} (ikR - 1)\, \mathrm{d}R$$

$$\approx p_A A ik \int\limits_{z_1}^{\infty} D(R) \Re(R) f(R - ct) \cos\theta(R) \frac{e^{ikR}}{R}\, \mathrm{d}R, \tag{3.18}$$

since if $kR \gg 1$, the term $ik - 1/R$ can be approximated by ik. This equation gives the pressure at a single point on the receiver. To account for the finite size of the transducer area, the receiver directivity must be included. Assuming this to be the same as the transmit directivity, D in equation (3.18) should be squared. This equation was implemented in a numerical approach of calculating the pressure field reflected from a plane copper reflector using MATLAB, see appendix C.22.

3.1.1 Simulation of the pressure field reflected from a plane copper reflector

The signal transmitted by the transducer, measured with the needle hydrophone in a distance of 22 cm, was used to represent $f(R - ct)$ in equation (3.18). The parameters are set in the MATLAB-script `indata4`, the MATLAB-script `Ekko` then uses these parameters to calculate the pressure field at the transducer after reflection from the copper reflector, based on the integral in equation (3.18). The result of simulating the echo from the copper reflector, when the distance between the copper reflector and the transducer was set to 13 cm, is shown in figure 3.2.
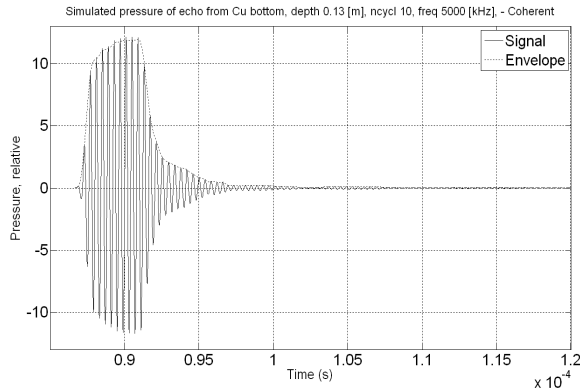
Figure 3.2: Simulated pressure echo from copper reflector with water-depth 13 cm.

The MATLAB-script `Ekko` was further used to simulate the echo pressure signals for different water-depths by changing the depth in `indata4`. The program `Env` was used to find the envelope of the simulated echo signals for each depth, and the echo duration at the -14 dB level, relative to the maximal amplitude, could then be found. The echo durations at each water-depth are summarized in table 3.1. The simulated echo duration as a function of water-depth is shown in figure 3.3.

Table 3.1: Simulated echo durations from a copper reflector, at the -14 dB level.

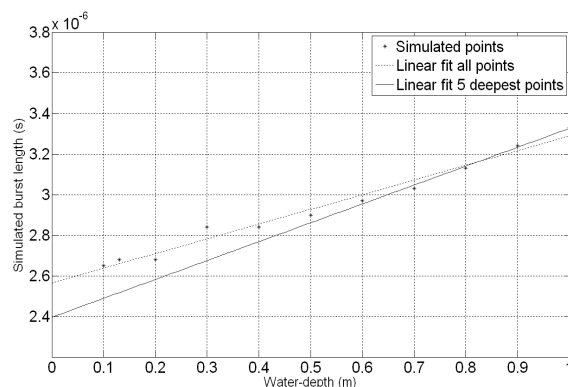| Water-depth [m]	0.1	0.13	0.2	0.3	0.4	0.5	0.6	0.7	0.8	0.9	1.0
Echo duration [μs]	2.65	2.68	2.68	2.84	2.84	2.9	2.97	3.03	3.13	3.24	3.33

Figure 3.3: Simulated echo duration as a function of water-depth

Curiously, there is a non-linear behaviour for small water-depths. A linear fit to all the data points, as well as a linear fit using the 5 largest distances only, are shown in figure 3.3. The parameters of the two lines, following the discussion in section 2.4, are $2\alpha/c = 7.24 \times 10^{-7}$ s/m and 9.3×10^{-7} s/m, respectively, with initial burst lengths $D/c = 2.56 \times 10^{-6}$ μs and 2.40×10^{-6} μs, respectively. The corresponding values of the θ_{-7dB} angles are then 1.89° and 2.14°. The θ_{-7dB} read from the directivity plot was 3.6°, hence the correspondence here is not very good. The real pulse length for 10 cycles of the 5 MHz transmitted burst is 2 μs, plus some more due to ringing in the transducer. Hence, the simulated initial burst length derived from

21

this plot is rather reasonable.

The calculations above are based on the echo pressure at the transducer. To compare this to the measured results from the copper reflector, the impulse response of the transducer must be known, this is further discussed in section 4.4. Convolving the simulated pressure with the impulse reponse, should return the simulated electrical signal. However, this was done assuming that the receiver response is equal to the transmitter response, i.e. assuming the transducer to be reciprocal. This assumption may not be correct, as is further discussed in section 4.4. Using the simulated electric signal, i.e. convolving the simulated echo pressure with the impulse response, to find the echo duration for different water-depths, gave an increase in burst length of about 1 µs compared to the results in figure 3.3. However, the linear plots still had approximately the same gradients.

3.2 Scattering from random rough surfaces

No real surface can be absolutely smooth, on some scale there is always a certain roughness. The problem of determining to which extent this roughness affects wave scattering behaviour has yet to be solved. Most of the work in this area can be put into one of two categories, either approximate, and hence of restricted applicability, or exact but formal, due to the complicated expressions resulting from this approach [23].

3.2.1 The Rayleigh criterion

Rayleigh was in 1877 the first to study wave scattering from random rough surfaces [23]. His work led to the so-called 'Rayleigh criterion', which can be used to determine the degree of roughness of a surface.
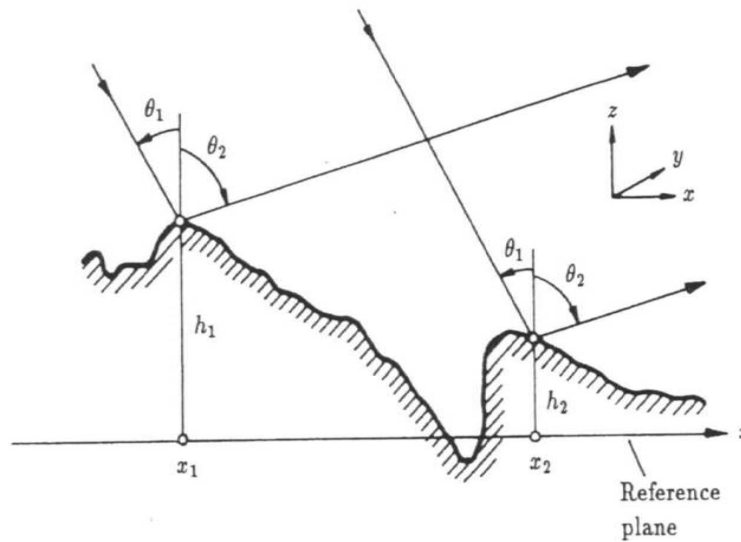

Figure 3.4: Diagram for determining the phase difference between to parallell rays scattered from different points on a rough surface, copied from [23].

A monochromatic wave incident at an angle θ_1 onto a rough surface, is scattered at an angle θ_2 in the azimuthal plane (i.e. the (x, z) plane of incidence), referring to figure 3.4. The phase difference between two rays scattered from different points on the surface at the same angle θ_2, with height difference $(h_1 - h_2)$ and difference in x-coordinates given by $(x_2 - x_1)$, is given

by

$$\Delta\phi = k[(h_1 - h_2)(\cos\theta_1 + \cos\theta_2) + (x_2 - x_1)(\sin\theta_1 - \sin\theta_2)], \qquad (3.19)$$

where k is the wave number of the incident and scattered waves. For specular scattering, i.e. $\theta_1 = \theta_2$, this phase difference becomes

$$\Delta\phi = 2k\Delta h \cos\theta_1. \qquad (3.20)$$

The phase difference determines the interference between these two rays. When $\Delta\phi \ll \pi$, the two waves have about the same phase, and will therefore interfere constructively. However, when $\Delta\phi \sim \pi$, the two waves are about 180° out of phase and will interfere destructively, cancelling out the scattered energy in the specular direction. When $\Delta\phi < \pi/2$ the surface is considered 'smooth' according to the 'Rayleigh criterion', otherwise it is 'rough'. Averaged across a surface, Δh is replaced by σ, which is the surface RMS deviation from smooth. By introducing the Rayleigh parameter, $R_a = k\sigma\cos\theta_1$, the 'Rayleigh criterion' for a 'smooth' surface can be stated as [23]

$$R_a < \pi/4. \qquad (3.21)$$

The 'Rayleigh criterion' illustrates an important point, namely that the 'effective roughness' of a scattering surface is not an intrinsic property of the surface, but also depends on the frequency and the angle of incidence of the incoming wave.

3.2.2 Phase considerations

Using Huygen's principle, the scatterers on the surface can be regarded as sources of secondary wavelets [23]. If a smooth surface is considered, where $h_1 = h_2$ everywhere, then equation (3.19) reduces to

$$\Delta\phi = k(x_2 - x_1)(\sin\theta_1 - \sin\theta_2). \qquad (3.22)$$

In the specular direction, $\theta_1 = \theta_2$, the phase difference between all these sources on the surface is zero, and the sources therefore constructively interfere to make a strong field in this direction. Away from this direction the phase difference is generally large, and contribution from different sources across the surface cancel out. Hence, for an infinite and smooth surface there is only scattering in the specular direction.

This result needs to be modified for a surface of finite extent, as strong scattering then occurs in and around the specular direction. As shown in figure 3.5 a) there is now a 'lobe' of scattered energy around the specular direction, the width of this lobe is dependent upon the dimensions of the surface relative to the wavelength of the incoming wave. This result is also found for a surface with $h_1 \neq h_2$ satisfying the 'Rayleigh criterion' for a smooth surface. As the phase difference is no longer negligible however, the amplitude of the specular field will be reduced, due to destructive interference, as illustrated in figure 3.5 b). This reduction can be approximated by $e^{-g/2}$, where g is given by [23]

$$g = 4k^2\sigma^2\cos^2\theta_1 = 4R_a^2, \qquad (3.23)$$

for specular scattering. The parameter g is therefore a measure of the roughness of a surface. It expresses the mean phase variations of a wave scattered from many points across the surface.
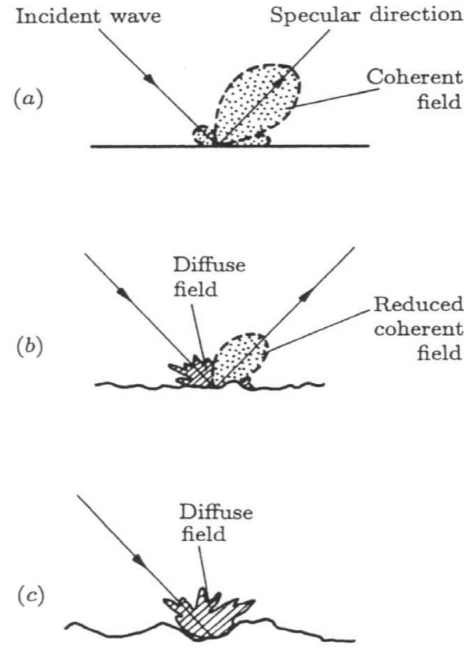
Figure 3.5: Coherent and diffuse scattering from finite and rough surfaces, copied from [23].

Considering scattering from a rough surface in other directions than the specular direction, the phase difference is given by equation (3.19). Because of the non-zero first term in this equation, there is no longer total destructive interference, as is the case for a smooth surface. Hence, energy is scattered into off-specular directions, illustrated in figure 3.5 c). The phase of this energy varies from 0 to 2π. In any direction the phase is determined by the height variations across the surface, and is not easy to predict unless the surface profile is known. The energy scattered in off-specular directions is often called the diffuse or incoherent field, since it is spread out over a wide range of angles and because it has no phase relationship with the incident wave. The specular scatter is similarly often called coherent, since it has a predictable and constant phase relative to the incoming wave.

3.2.3 Characterization using frequency shifts

The transmitted pulse has a nominal frequency, f, and a bandwidth of at least the reciprocal of the pulse length, τ. As the transmitted pulse is scattered from a rough seabed the bandwidth allows the power spectra of the pulse to be significantly altered [12]. In Kirchhoff approximation theory an analytic expression for the coherent specular amplitude, for a surface of Gaussian roughness, is given by

$$\langle \psi^{sc} \rangle = \psi_0^{sc} e^{-g/2}, \tag{3.24}$$

where g is given in equation (3.23) and ψ_0^{sc} is the pressure amplitude of the surface reflection from the same surface with zero roughness [12]. The angle-bracket mean is the average over different areas of the surface. Equation (3.24) shows that the coherent component of the echo is dependent on frequency, because g is a function of the wave-number. In the expression above, the effect of the impedance and the effect of the roughness is separated. ψ_0^{sc} is dependent on the characteristic impedance of the sediment relative to the the characteristic impedance of water, while the exponential term is dependent on the surface roughness [6]. For a broad-band

24

wavefield, the expression in equation (3.24) needs to be generalised as follows

$$\langle \psi^{sc}(\sigma) \rangle = \int\limits_{f=0}^{\infty} \psi_0^{sc}(f) e^{-g(f,\sigma)/2} \, \mathrm{d}f. \qquad (3.25)$$

As can be seen from equation (3.25), a change in roughness leads to a frequency shift of the returned signal. The power spectrum of the echo, is the product of the power spectrum of the scattered field from a smooth surface, which is similar to the power spectrum of the transmitted signal, and the roughness curve, which is the exponential term for a given roughness for different frequencies ($e^{-2k^2\sigma^2}$ plotted versus frequency). Berntsen *et al.* [6] calculate theoretical values for the frequency shift as a function of roughness and depth, with which they compare the frequency shift of the measured echo, to find the roughness.

In practice the non-specular coherent component, due to interactions with facets of the bottom that are normal to the incoming wave, but located at angles away from the acoustic axis, complicates this frequency dependence. The frequency shifts of the coherent and diffuse components of the echoes depend differently on roughness, hence it is important to consider the composition of the echoes [12]. Looking at the exponential term, this method only works if the roughness is not too large compared to the wave length of the transmitted signal, as the exponential term goes to zero. Also, calculation of the frequency shifts from the measured echo signals is not straightforward, as the frequency shifts are small and long time series are needed to obtain good enough resolution. Biffard *et al.* [12] use concatenation of successive, windowed echo time-series to calculate these shifts. The physical correctness of this approach is not discussed. Hence, this method was not looked further into in this master thesis.

Chapter 4

Experimental setup and method

4.1 Experimental setup

The main experimental setup used for the scattering measurements from different surfaces is shown in figure 4.1
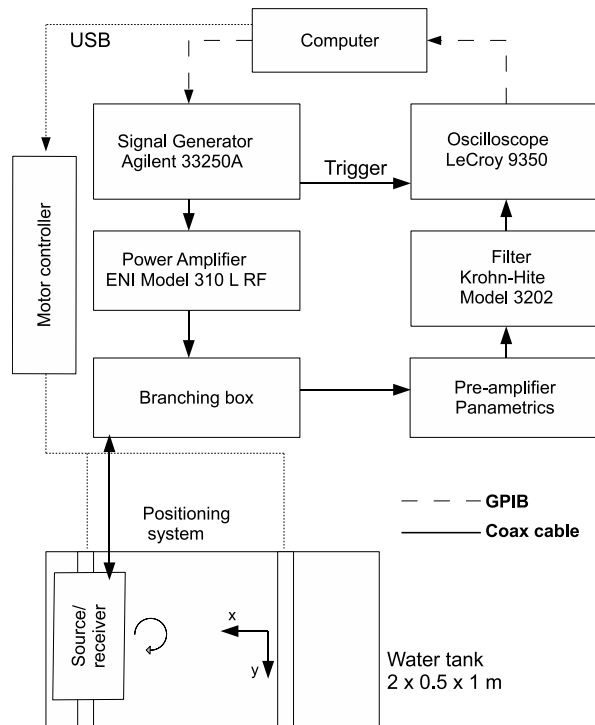

Figure 4.1: Block diagram of the experimental setup, water tank seen from above.

Both the signal generator and the oscilloscope could be controlled either manually or via the computer, using GPIB communication. The signal generator applied a 5 MHz (or later 1.4 MHz) sine-wave burst, consisting of between 10 to 30 cycles and with a peak-to-peak amplitude ranging from 0.2 V to 0.5 V. The burst period was set to 200 ms, making sure that no multiple echo effects occured. The signal was then amplified by a 50 dB power amplifier before being sent to the transducer via a branching box. The branching box was only used for the later measurements on copper and sand. For the earlier measurements the signal from the power amplifier went directly to the transducer. A monostatic setup, meaning that the same transducer is used both as source and receiver, was used for the main experiments. The

branching box makes the amplified signal go straight to the transducer, and thereby prevents the oscilloscope and power-amplifier from becoming saturated by the transmitted signal. When working as a sound source, the transducer transmits spherically diverging waves toward the scattering surface. When the sound is scattered back, the transducer works as a receiver, transforming the sound energy at the transducer surface to electrical energy. The received signal goes via the branching box to a pre-amplifier, which amplifies the signal to achieve better precision in the digitalization and to improve the signal-to-noise ratio. Low frequency noise, below 2 MHz, is then removed by a high-pass filter, before the oscilloscope digitizes the signal. The sample rate used by the LeCroy oscilloscope was ranging from 0.1 GHz, when 1000 points were sampled in a 10 μs window, to 20 MHz, when 1000 points were sampled in a 50 μs window. This is adequate for the echo bandwidths of the 5 and 1.4 MHz signals, to satisfy the Nyquist sampling theorem. The signals on the oscilloscope were read into the computer via the USB-GPIB adapter, and could then be further processed in MATLAB. A brief description of the instruments used can be found in tables 4.1 and 4.2.

Table 4.1: Instruments used in the main experimental setup.

Type	Producer	Model	Serial number
Signal generator	Agilent	33250A	-
Power amplifier	ENI	Model 310 L RF	H-102
Oscilloscope	LeCroy	9350	177531
Pre-amplifier	Panametrics	Ultrasonic Preamp 40/60 dB	5660B/1094
Filter	Krohn-Hite	Model 3202	H-107
Stationary PC	HP	dx5150 MT with Windows XP	122400
Branching box	home made	-	-

Table 4.2: Other instruments used in parts of the experiment.

Type	Producer	Model	Serial number
Impedance Analyzer	HP	4192A	176139
Needle hydrophone 0.2 mm	Precision Acoustics	-	-
Needle hydrophone 1.0 mm	Precision Acoustics	-	118
Power Supply 28 V	Oltronix	B300D	177234
Pre-amplifier	Panametrics	Ultrasonic Preamp 0.5 − 10 MHz	5670/1312

4.1.1 Transducer

First, an appropriate sound source needed to be found. The impedance analyzer was used to determine the resonance frequencies of some of the transducers in the acoustics laboratory. The field data one has for comparison is taken at a water-depth of about 50 m, with an echosounder operating at frequencies between 38 kHz and 200 kHz. The usual beam-width of commercial echosounders is around 7°. Since the greatest depths achievable in the laboratory tank is about 0.5 m, the scaling factor used was 100. Therefore, a sound source with a resonance frequency around 5 MHz was considered appropriate.

The transducer used in the experiment has a resonance frequency of about 5 MHz, found by measurements done with the impedance analyzer in air and in water. The impedance, Z, of a transducer, is given by the relation

$$Z = R + iX = |Z|e^{i\phi_Z}, \tag{4.1}$$

where R is the resistance, X is the reactance, $|Z|$ is the absolute value of the impedance and ϕ_Z is the phase displacement. The admittance is closely connected to the impedance by the relation

$$Y = 1/Z = G + iB = |Y|e^{i\phi_Y}, \tag{4.2}$$

where G is the conductance, B is the susceptance, $|Y|$ is the absolute value of the admittance and ϕ_Y is the phase displacement. According to the IEEE Std. 176-1987, the series resonance frequency of a piezoelectric transducer element is given by the frequency of the maximum conductance [16]. Hence, the conductance was measured for a range of frequencies with the impedance analyzer. For these measurements the transducer was placed inside the transducer housing and connected to the impedance analyzer using a 50 Ω coaxial cable. Measurements in air gave the result in figure 4.2 a). The resonance frequency is approximately 4.8 MHz. The measurements in water gave the result in figure 4.2 b). The resonance frequency here is 4.85 MHz. In all of the measurements done with this transducer, a 5 MHz burst was applied, as this was seen to give the largest response when the output signal was measured with a needle hydrophone. The discrepancy between the measured resonance frequency and the frequency giving the maximal response, can be explained by the fact that the other instruments and cables used in the setup also influence the resonance frequency.
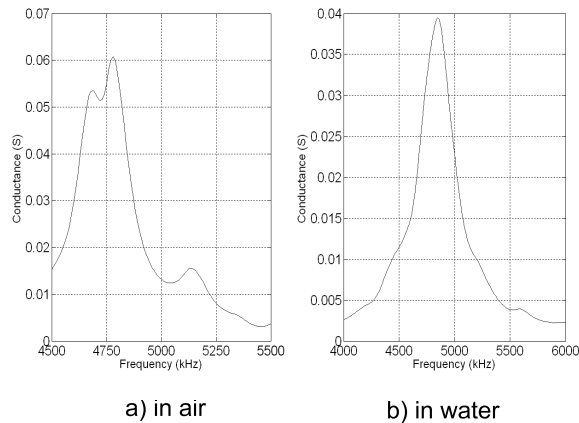

Figure 4.2: Conductance versus frequency for the 5 MHz transducer in air and in water.

The diameter of the source was measured to $d = 5.75$ mm, which gives a radius of $a = 2.875$ mm. The half angle beam-width of the source, given by the angle of the first minima, could then be calculated. The first pressure node is found by using the term in equation (2.3) that gives the angular dependence of the pressure amplitude. Looking up the table value for j_{11}, which is 3.83 [15], gives

$$\theta_1 = \sin^{-1}\left(\frac{3.83}{ka}\right) = \sin^{-1}\left(\frac{3.83}{2\pi a f/c}\right), \tag{4.3}$$

where the resonance frequency of 5 MHz and the sound speed in water, $c = 1500$ m/s, are used. This give a half angle beam-width of $\theta_1 = 3.65°$, which gives a total beam-width of 7.3°, close to the beam-width of commercial echosounders. Correspondingly, the θ_{-3dB}, θ_{-6dB} and

θ_{-7dB} angles can be calculated using the following equations [16]

$$\theta_{-3dB} \approx \sin^{-1}\left(\frac{1.616}{ka}\right) = \sin^{-1}\left(\frac{1.616}{2\pi af/c}\right), \tag{4.4}$$

$$\theta_{-6dB} \approx \sin^{-1}\left(\frac{2.215}{ka}\right) = \sin^{-1}\left(\frac{2.215}{2\pi af/c}\right), \tag{4.5}$$

$$\theta_{-7dB} \approx \sin^{-1}\left(\frac{2.38}{ka}\right) = \sin^{-1}\left(\frac{2.38}{2\pi af/c}\right). \tag{4.6}$$

The -3 dB angle is the angle away from the acoustic axis where the sound intensity is reduced by half relative to the sound intensity on the acoustic axis. The -6 dB angle is the angle where the pressure amplitude is reduced by half relative to the pressure amplitude on the acoustic axis. Putting in the same values for f and c as above, these equations give $\theta_{-3dB} = 1.54°$, $\theta_{-6dB} = 2.11°$ and $\theta_{-7dB} = 2.27°$. One can be certain of being in the far field of the transducer when one is located at a distance from the source greater than the Rayleigh distance for the particular transducer. This distance is given by $R = A/\lambda = \pi a^2 f/c$. The Rayleigh distance for the 5 MHz transducer is therefore $R = 8.7$ cm.

4.1.2 Transducer with larger beam-width and lower frequency

After doing measurements with the 5 MHz transducer on copper, sand and clay, it was considered to use a second transducer, with lower frequency and greater beam-width, to see how this influenced the received echo signal. Measurements were only done on sand surfaces with different grain size. A transducer marked with the resonance frequency 1.25 MHz was found. Using the impedance analyzer, the conductance was measured with frequency steps of 5 kHz in the relevant frequency range, both in air and in water. The measurements in air were done with the transducer connected to the impedance analyzer with electrical wires, while the measurements in water were done with the transducer inside the transducer housing, connected to the impedance analyzer with a 50 Ω coaxial cable. The results of the measurements done with the transducer placed in air and in water are shown in figure 4.3.
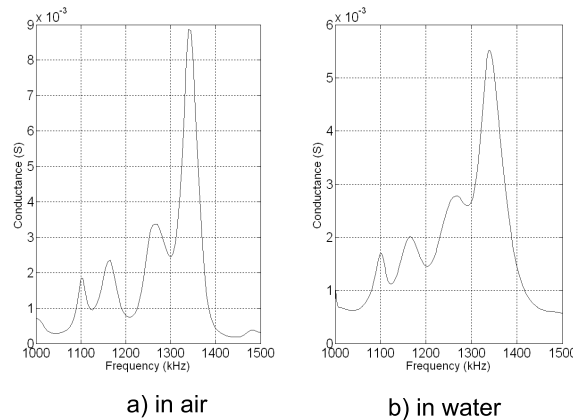

a) in air   b) in water

Figure 4.3: Conductance versus frequency for the 1.4 MHz transducer in air and in water.

From figure 4.3 the resonance frequency is found to be 1.34 MHz. However, for the measurements a 1.4 MHz burst was used, as this frequency seemed to give the maximal response when the signal from the transducer was measured with a needle hydrophone.

The diameter of the source was measured to $d = 8.28$ mm, which gives a radius of $a = 4.14$ mm. The half angle beam-width of the source, given by the angle of the first minima,

could then be calculated. The first pressure node is again found by using equation (4.3), where the resonance frequency of 1.4 MHz and the sound speed in water, $c = 1500$ m/s, are used. This give a half angle beam-width of $\theta_1 = 9.1°$, which gives a total beam-width of 18.2°. Using equations (4.4), (4.5) and (4.6), the θ_{-3dB}, θ_{-6dB} and θ_{-7dB} angles for this transducer could be calculated, leading to the results $\theta_{-3dB} = 3.82°$, $\theta_{-6dB} = 5.23°$ and $\theta_{-7dB} = 5.63°$. The Rayleigh distance for the 1.4 MHz transducer, given by $R = A/\lambda = \pi a^2 f/c$, is $R = 5$ cm.

4.1.3 Transducer setup and positioning system

The transducers are piezoceramic disks fitted into larger brass disks. There is no matching layer in front of the ceramic, except for a thin layer of adhesive silver, nor any backing layer, only air. A rough lay-out of the transducer construction is shown in figure 4.4.
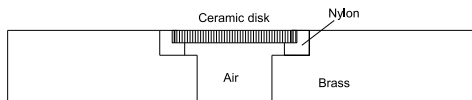
Figure 4.4: Rough lay-out of the transducer construction.

Electrodes were mounted on each side of the transducer, and the transducer was placed inside a waterproof housing. The housing is mounted on two rods, one containing the electrical wires and one with screw thread so that the transducer and the housing can be moved up or down the rod, thereby adjusting the height of the transducer above the bottom of the tank. The rods are attached to a wagon, which is then mounted to a horizontal rack crossing the top of the tank. The rack can be moved back and forth along the x-direction of the tank, referring to figure 4.5. This leaves possibility of adjusting the position of the transducer manually both in the x, y and z-directions of the tank, while the housing containing the transducer can be rotated by a motor controlled via the computer.
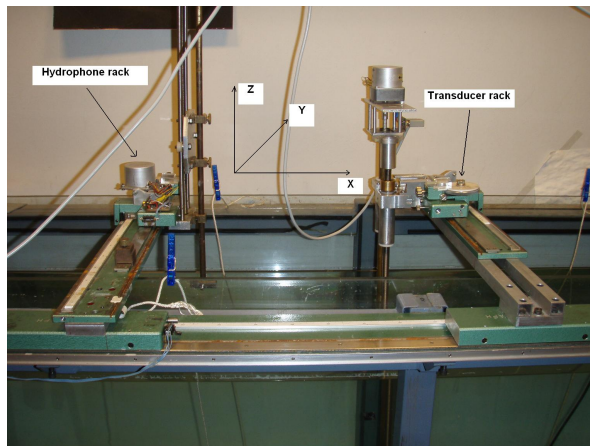

Figure 4.5: Racks for hydrophone and transducer.

When measuring the sound signal from the source, as well as for measuring the directivity of the transducers, a needle hydrophone was mounted to a rod, which was similarly as for the transducer rod, attached to a wagon mounted on another horizontal rack. The hydrophone could also be moved in the x, y, and z-directions, however, this movement could be achieved by using the motor system, controlled via the computer. MATLAB-scripts were used to set the number of steps and the speed of the movement. Three of the four motors have names that

correspond to the direction in which they move the hydrophone, while motor W rotates the transducer around an axis parallell to the y-axis in figure 4.5. Motor X moves the horizontal rack in steps of 0.1 mm. When the number of steps set have a positive sign, the horizontal rack moves in the negative x-direction. Motor Y moves the hydrophone wagon 0.1 mm along the horizontal rack for each step. For a positive number of steps it moves in the positive y-direction. Motor Z moves the hydrophone rod 0.0026 mm for each step. For a positive number of steps it moves in the negative z-direction. Movement in the opposite directions is achieved by adding a negative sign in front of the number of steps. Motor W rotates the transducer 90° when the number of steps is set to 7750, making 1° approximately 86 steps. The accuracy of the motors were checked by moving the hydrophone and rotating the transducer a fixed amount of steps back and forth, and then checking if it came back to the same position every time. For the X, Y and Z motors there seemed to be no deviation, so it is assumed that the uncertainty here is very small, approximately the length of one step. For the rotation, the transducer was rotated back and forth through 90°. The exact position of the transducer was difficult to measure, but it seemed to not come all the way back to the same spot. This is probably due to backlash in the cogwheel rotating the transducer, when the direction of the rotation is changed. The uncertainty here was estimated to approximately 1°.

4.2 Measuring the sound signal from the source

The first task was to measure the sound signal from the source. For the 5 MHz transducer, this was done by placing a 0.2 mm diameter needle hydrophone in the far field of the source. The signal measured by the needle hydrophone was then sent to the pre-amplifier and the filter before being digitized by the oscilloscope. For the 1.4 MHz transducer, a 1.0 mm diameter needle hydrophone was used. The signal from the needle hydrophone was now sent directly to the oscilloscope, without being pre-amplified or high-pass filtered. The branching box was used for the 1.4 MHz transducer, but not for the 5 MHz transducer. The needle hydrophone needs an applied DC voltage of 28 V.

The positioning system was used to align the needle hydrophone relative to the sound source, with the acoustic axis of the source pointing horizontally in the negative x-direction, referring to figure 4.5. The alignment was done by measuring the signal in two different positions from the source 15 cm apart, both in the far field of the transducer. When the receiver was placed in the position closest to the source, the needle hydrophone was moved in the y- and z-directions with steps of 1 mm and 0.5 mm, respectively. The rms-value of the signal amplitude was calculated in each position, and the hydrophone was moved to the position where it received the strongest signal. When the receiver was in the position furthermost from the source, the transducer was rotated with steps of approximately 0.3°, through a total angle of 4.6° around the acoustic axis. The transducer was rotated back to the position giving the strongest signal. This process was repeated until the same results were acquired time after time, which meant that the source and receiver were perfectly aligned.

A measurement of the signal on the acoustic axis was made in a distance of about 22.3 cm from the source for the 5 MHz transducer, and in a distance of about 20 cm for the 1.4 MHz transducer. With the source and receiver aligned, the directivity patterns for the transducers could be measured. This is discussed in the next section. For the measurements with the 1.4 MHz, which was done at a later time, motor Y driving the needle hydrophone in the y-direction seemed to be defect. It did not move the same distance every time, even though the same amount of steps were chosen. Therefore, it was considered to be better to move the hydrophone manually in the y-direction, using the positioning wheel on the hydrophone wagon to get the position accurate within 0.1 mm, see figure 4.6.
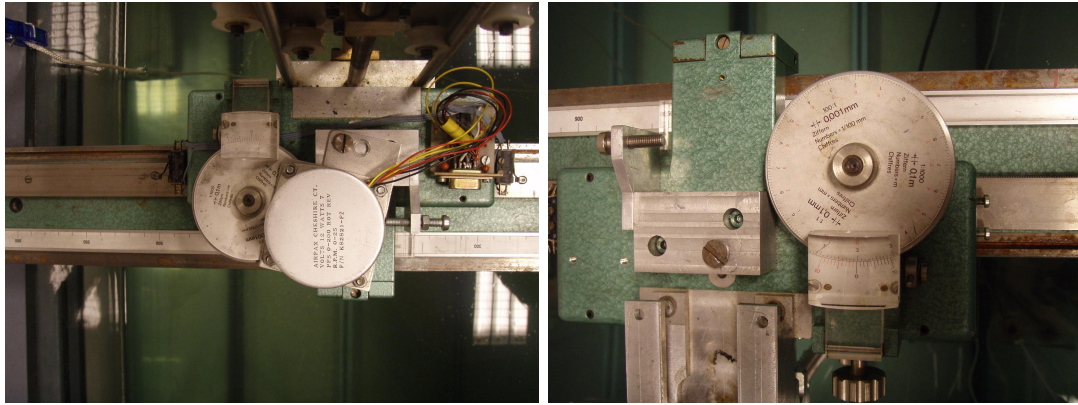
(a) Hydrophone rack.   (b) Transducer rack, showing the resolution of the scale.

Figure 4.6: Positioning wheel with high resolution scale.

4.3 Transducer directivity

The directivity measurements were done using the same setup discussed in section 4.2 for the respective transducers.

4.3.1 Directivity of the 5 MHz transducer

For the 5 MHz source, the directivity was measured using a 0.2 mm needle hydrophone placed approximately 20 cm from the source. For these measurements a 20 cycle, 5 MHz burst was used. The motor system moved the hydrophone in steps of 2 mm out to 44 mm on each side of the central acoustic axis, in the y-direction referring to figure 4.5. In each position the received signal was measured. A MATLAB-script calculated the rms-amplitude of the steady state part of the received signal, which could then be plotted as a function of position. Knowing the distance between the transducer and the hydrophone, as well as the distance from the acoustic axis for each measurement, a plot of the rms-amplitude in dB, relative to the rms-amplitude on the acoustic axis, as a function of angle away from the central acoustic axis could be made. This is shown in figure 4.7.
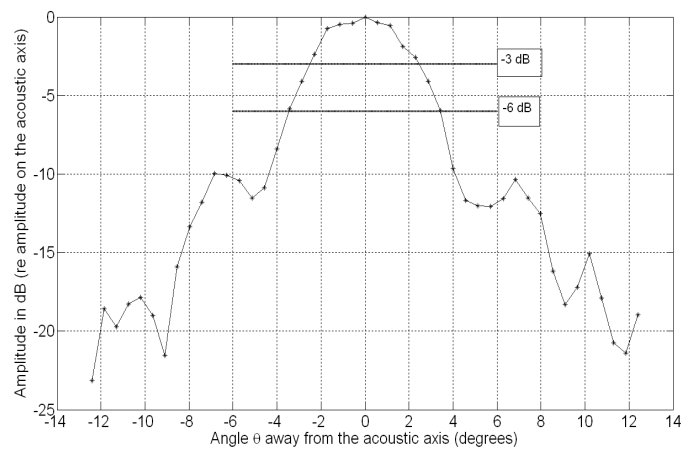
Figure 4.7: Directivity of the 5 MHz source.

33

In section 4.1.1 the angle of the first minima was calculated, and gave a result of $\theta_1 = 3.65°$. In the directivity plot the angle of the first minima seems to be a bit larger than the angle calculated, approximately 5°. From figure 4.7 it is also possible to read out θ_{-3dB}, θ_{-6dB} and θ_{-7dB}. These are given in table 4.3, along with the angles calculated in section 4.1.1.

Table 4.3: Angles found from the directivity plot versus calculated angles, for the 5 MHz transducer.

Angle	Calculated	From directivity plot
θ_1	3.65°	$5 \pm 0.6°$
θ_{-3dB}	1.54°	$2.5 \pm 0.6°$
θ_{-6dB}	2.11°	$3.45 \pm 0.6°$
θ_{-7dB}	2.27°	$3.6 \pm 0.6°$

The uncertainties was found using standard formulas for uncertainty, this is discussed in appendix A.1.2. All of the angles read from the directivity plot are a bit larger than the calculated values. This could indicate that the effective radius of the source is a bit less than the radius measured. Using for example equation (4.4) to solve for the radius a, and inserting the value $\theta_{-3dB} = 2.5 \pm 0.6°$, give an effective radius of 1.8 ± 0.5 mm.

4.3.2 Directivity of the 1.4 MHz transducer

For the 1.4 MHz source, the directivity was measured using a 1 mm needle hydrophone placed approximately 15 cm from the source on the acoustic axis. For these measurements a 20 cycle, 1.4 MHz burst was used. The needle hydrophone was moved in steps of 2 mm, out to 50 mm on each side of the acoustic axis. In each position the received signal was measured. The signal was averaged over 63 sweeps by the oscilloscope. Using a MATLAB-script, the rms-amplitude of the steady state of the signals was calculated, and the directivity could then be plotted following the same procedure discussed for the 5 MHz transducer.
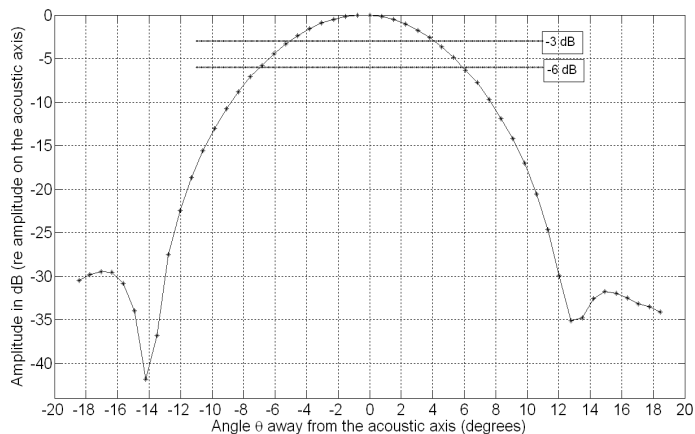

Figure 4.8: Directivity of the 1.4 MHz source.

From the directivity plot in figure 4.8, the main lobe seems to be a little bit shifted from the acoustic axis. The reason for this could be that the needle hydrophone was not accurately positioned before the directivity measurements were started. It is assumed that the main lobe should be symmetrical around the acoustic axis. The angles are found by adding the positive

34

and negative angles and then dividing the result by two. In section 4.1.2, the angle of the first minima was calculated to $\theta_1 = 9.1°$. In the directivity plot the angle of the first minima seem to be larger than the angle calculated, approximately 13.5°. From figure 4.8 it is also possible to read out θ_{-3dB}, θ_{-6dB} and θ_{-7dB}. These are given in table 4.4 along with the angles calculated in section 4.1.2.

Table 4.4: Angles found from the directivity plot versus calculated angles, for the 1.4 MHz transducer.

Angle	Calculated	From directivity plot
θ_1	9.1°	$13.5 \pm 0.4°$
θ_{-3dB}	3.82°	$4.6 \pm 0.4°$
θ_{-6dB}	5.23°	$6.4 \pm 0.4°$
θ_{-7dB}	5.63°	$7.0 \pm 0.4°$

All of the angles from the directivity plot are, as for the 5 MHz transducer, a bit larger than the calculated values. Using equation (4.4), solving for the radius a and inserting the value $\theta_{-3dB} = 4.6 \pm 0.4°$, give an effective radius of 3.4 ± 0.4 mm.

4.4 Recovering the impulse response of the transducer

In principle it should be easy to find the impulse response of the source. If 'h' is the impulse response of a system, then the system output is given by the convolution of the system input and the impulse response

$$s_{out} = s_{in} * h. \tag{4.7}$$

By deconvolution of the system input and the system output, it should then be straightforward to find the impulse response, 'h'. However, using measured signals of the input to the source and the output from the source, with built in functions for deconvolution in MATLAB, does not work due to the strong influence of the noise in the measured signals. A way around this is to use the Fourier and inverse Fourier transforms on the measured signals, and then only use the parts of the signals that are significant in relation to the noise. When the Fourier transforms of the input and output signals are found, the transfer function 'H' of the source can be found by division of the signal out on the signal in

$$H = S_{out}/S_{in}. \tag{4.8}$$

The impulse response, 'h', can then be found by taking the inverse Fourier transform of the transfer function, 'H'. N is the ratio between the maximum value of the input signal and noise, and can be set as a parameter in the program written by Halvor Hobæk to calculate the impulse response (see appendix C.19). Testing the program with different values of N, showed that $N = 60$ (for the 5 MHz transducer) and $N = 110$ (for the 1.4 MHz transducer) gave the best overall correspondence when the measured output signal is plotted against a reconstructed version, using the calculated impulse response and the measured input signal.

4.4.1 The impulse response for the 5 MHz transducer

The input signal was measured with the oscilloscope after being pre-amplified by the power amplifier. The output signal was measured with a 0.2 mm needle hydrophone in a distance of 22.3 cm from the source, going through the pre-amplifier and the filter before being digitized by the oscilloscope. Hence, the impulse response calculated is the impulse response of both the transducer, the pre-amplifier and the filter connected in series. The signals were sampled with

the same sampling frequency, 0.1 GHz. The measured signals were normalised, dividing by the maximal absolute value, and edited to start approximately at the same index. The m-file `imprespons(signalinn,signalut,60)` returns the impulse response, as well as a reconstructed version of the output signal, which is found by convolution of the measured input signal with the impulse response. The reconstructed output signal is compared with the original output signal. To better see the difference between these signals, the envelopes of the signals were found and plotted, by using the m-file `Env`.

(a) Reconstructed and original output signal.   (b) Reconstructed and original envelope.
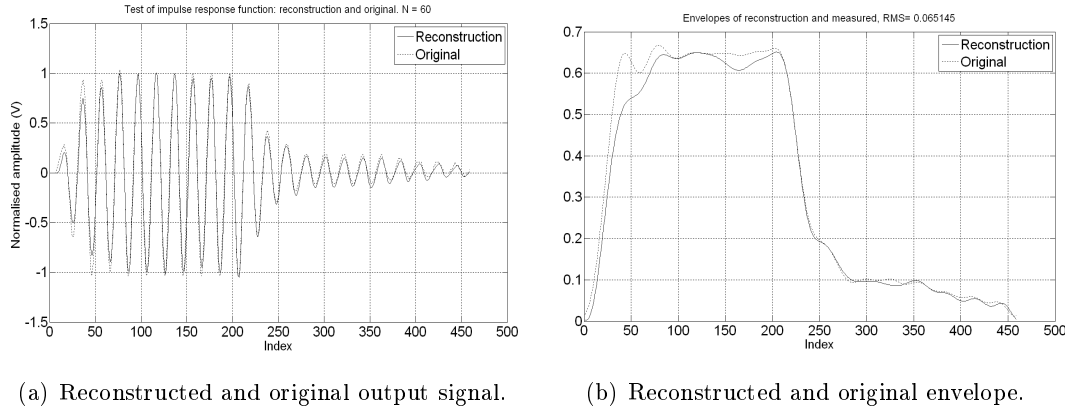
Figure 4.9: Reconstructed and original signals for 5 MHz transducer.

As seen in figure 4.9 the reconstructed signal looks like the original, however, the amplitude does not rise as steeply as the amplitude of the original output signal. This was considered a good enough match to further use the impulse response found by this method.

4.4.2 The impulse response for the 1.4 MHz transducer

For the 1.4 MHz transducer, the input signal was measured with the oscilloscope after being amplified by the power amplifier and going through the branching box. The signal applied was a burst containing twenty periods of a sine wave, with frequency 1.34 MHz. The output signal was now measured with a 1 mm needle hydrophone in a distance of 20 cm from the source, which was directly sent to the oscilloscope, without pre-amplification or filtering. The sampling frequency was the same for both the input and output signals, namely 20 MHz. The same m-file was used to find the impulse response and a reconstructed output signal for this transducer, as discussed in the previous subsection for the 5 MHz transducer. The difference is that the impulse response is now the response of the transducer alone, assuming that the needle hydrophone is independent of frequency for the frequency band of the received signal. Setting N to 110 was seen to give the best result for the reconstructed signal.

(a) Reconstructed and original output signal.
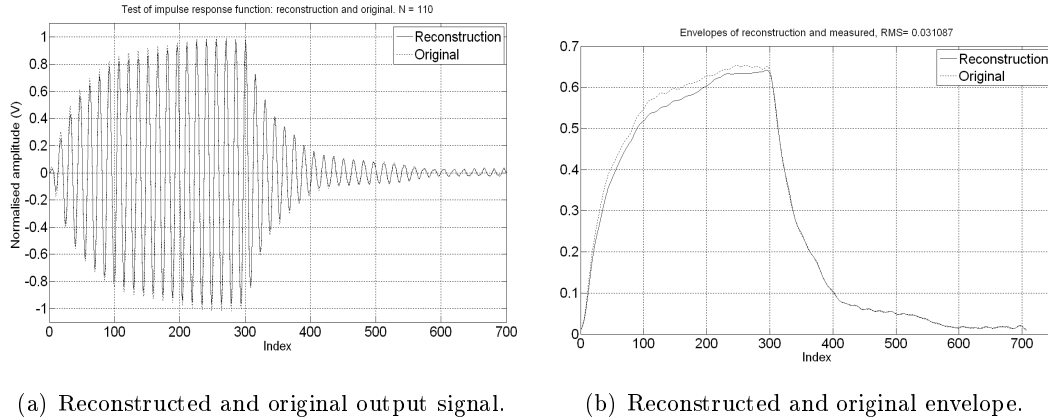

(b) Reconstructed and original envelope.

Figure 4.10: Reconstructed and original signals for 1.4 MHz transducer.

Again the original signal have a steeper rise than the reconstructed signal, otherwise they are very similar.

4.4.3 Using the impulse response to calculate the simulated electrical signal

The model for reflection at a plane boundary, discussed in section 3.1, was used to calculate the simulated echo pressure, with results shown in subsection 3.1.1 for a water-depth of 13 cm. However, to compare these simulations with the measured signals from the different surfaces, these echo signals have to be transformed to electrical signals that could be measured by the oscilloscope. Looking at the results for the 5 MHz transducer, convolution of the simulated signal with the impulse response found for the transducer, pre-amplifier and filter, returns the electrical simulated signal. This method is based on the assumption that the impulse response is reciprocal, as the response on reception is needed here while it is the transmitter response that is calculated. The m-file `impresanal` (see appendix C.20) returns the expected electrical signal, which can then be compared with the measured signal. The signals that were used to find the impulse response are shown in figure 4.11, while the simulated and measured signals from a copper reflector are compared in figure 4.12.

(a) Input signal.
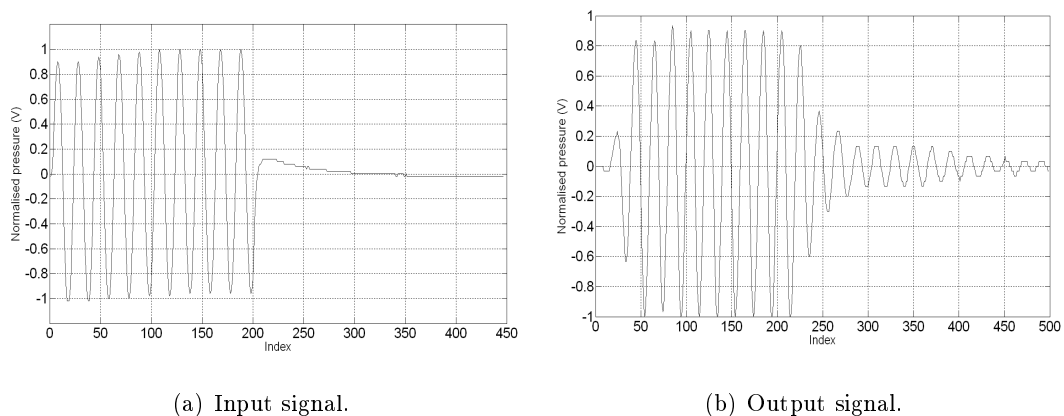
(b) Output signal.

Figure 4.11: The input and output signals to/from the transducer, used to calculate the impulse response.

37

(a) Simulated echo pressure.

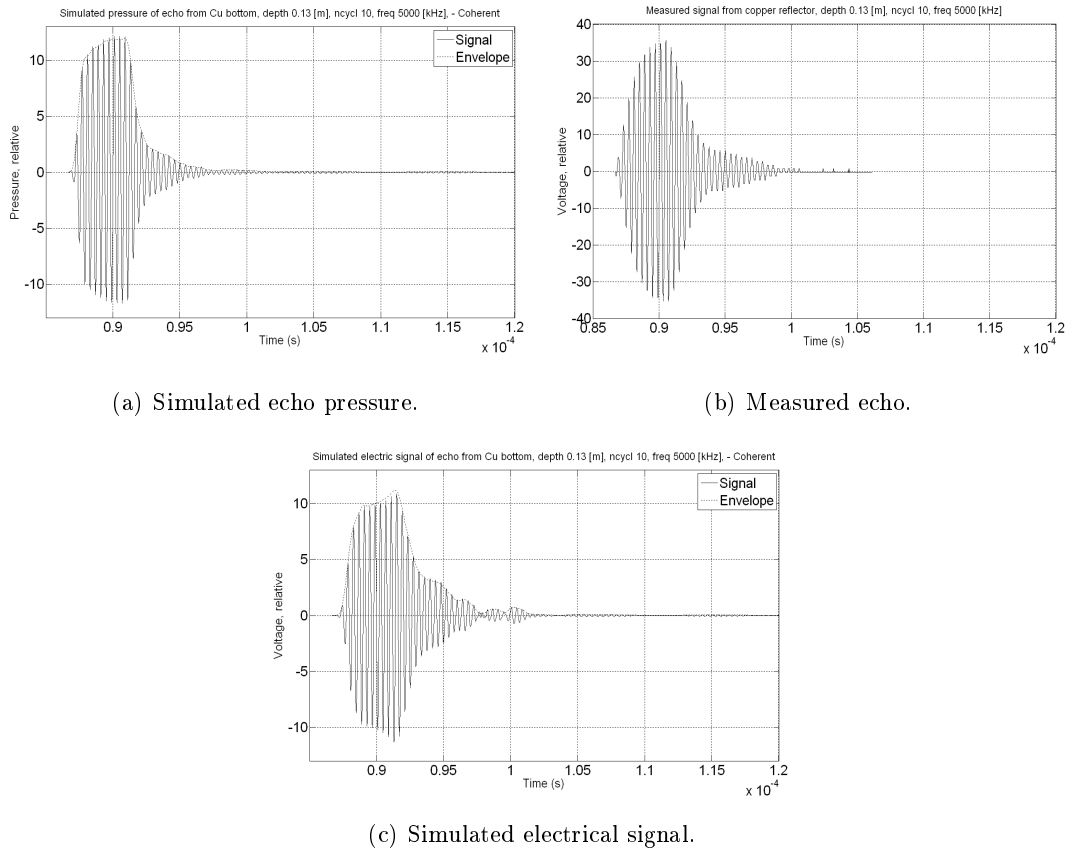(b) Measured echo.

(c) Simulated electrical signal.

Figure 4.12: Simulated compared to measured signals, reflection from a copper reflector at a water-depth of 13 cm.

As seen in figure 4.12, the results are not very good, the simulated electrical signal and the measured signal from the copper reflector are not similar. The reason for this is probably that the assumption of reciprocity is false. The impulse response should have been measured specifically on reception, however, this is not a trivial task.

4.5 Signal variation

For a surface of random roughness the returned echo is highly variable. Both the strength and the shape of the echo changes as different portions of the surface are insonified. This is due to the variation in the incoherent component of the echo. The fluctuations in signal strength and shape observed as the source insonified different parts of the coarse sand surface are illustrated in figure 4.13.
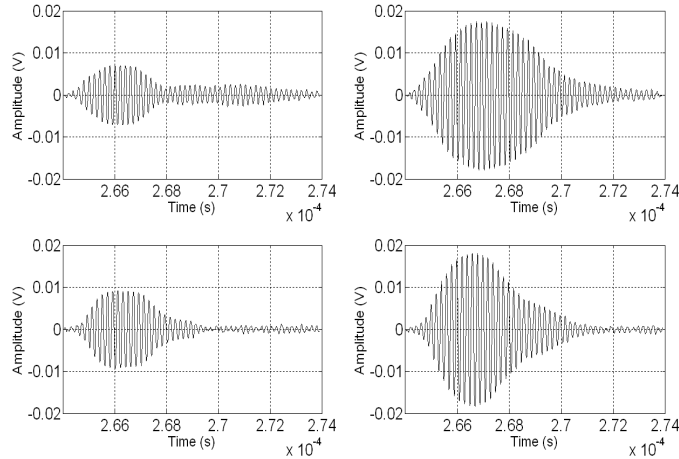
Figure 4.13: Signal variation in scattering from the coarse sand surface.

The source was moved in steps of 5 mm, in a four-by-five matrix (horizontally in the y and x-directions) along the surface, and the returned signals were measured, giving a total of twenty individual signals. Then, the individual full-waveform signals were stacked, that is phase-aligned and averaged, returning the coherent signal. The incoherent part has random phase and nulls out when averaging.

4.5.1 Phase alignment and averaging

The method of stacking individual signals is discussed in this subsection. This method was used for measurements from the sand and clay surfaces.

The process of stacking several returned signals, includes phase-aligning the full-waveform echo signals and finding the average of these signals. For real measurements in the ocean, the individual signals should be aligned by their bottom pick, as the water-depth is not necessarily the same for all the measurements. However, in the laboratory, the water-depth is expected to be equal for all of the measurements used for averaging. This did however not seem to be the case, as some of the signals started up to three periods before others. Due to the high-frequencies used, only small deviations from an even surface lead to different time-delays of the individual signals taken from different portions of the surface.

For the sand measurements, the individual signals were stacked without considering the bottom pick, as the start of the signals was not well-defined, making it difficult to define a threshold level. The method of phase-aligning signals is not straightforward. [12] suggests phase-alignment using rising zero-crossings within one cycle of the bottom pick. However, as mentioned it is not always easy to define the start of signal. Hence, the method used in this work was to phase-adjust the signals using zero-crossings in the middle of the signals. The signals were interpolated by a factor of four, so that a better estimation of the zero-crossings of the signals could be found. Then an index for the zero-crossing that should be used for phase-alignment needed to be picked. Which index was chosen here seemed to be of great importance of how the resulting coherent signal turned out, especially in the cases where the individual signals had very different shape. The steady-state of a signal has constant amplitude and phase, however, not all of the signals measured had a well-defined steady-state. The signals should be phase-aligned at the mid-point of the signal, where the signal have the largest amplitude. But which one of the twenty signals should be used to decide this index? In some cases the individual signals varied a lot, and the rise and maximal amplitude of the different signals were

39

located at different places on the time-axis, as illustrated in figure 4.14.
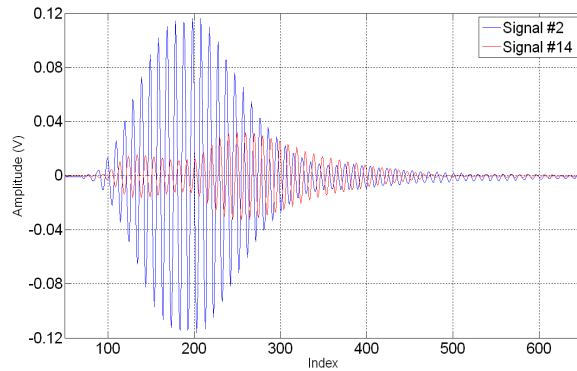

Figure 4.14: Variation in the individual signals, measured with the 5 MHz transducer on the fine sand surface.

It was decided to check the rms-amplitude of each of the signals using a MATLAB-script, and then choose the index for phase-alignment from the signal that had the largest rms-amplitude. Referring to figure 4.14, signal #2 would be chosen and an index around 190 would be used for phase-alignment. This seem to be a logical solution, as this signal will influence the averaged result more than signals with lower amplitude. In addition, the signals with the higher amplitudes look 'nicer', with only one rise, a well-defined peak and a fall, much like the echo signals from the copper reflector. However, this method requires that the individual signals are checked manually to see which one should be used for phase-alignment. A method that automate this process should probably be looked into.
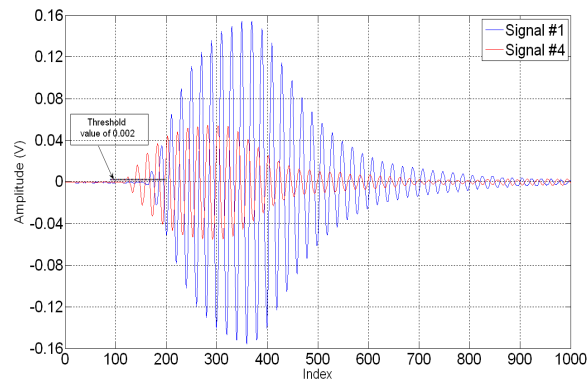
Figure 4.15: Signals from clay surface, showing the threshold value of 0.002 V set for the bottom pick.

For the clay measurements the individual signals could also be shifted 1-3 periods, depending on the bottom pick of the signal. For well-defined signals with a large signal-to-noise ratio, as was the case for the clay measurements, the start of the signal can be found by defining a threshold value, thereby deciding the index of the bottom pick, see figure 4.15. This could then be programmed in MATLAB so that the signals are still aligned by phase at a zero-crossing in the middle of the signal, but the variations in the index where the signal starts is accounted for, so that they are also aligned by their bottom pick (see appendix C.18).

The Hilbert transform of the coherent signals gives the signal envelopes of the coherent signals. Since the coherent signals are found using a phase-alignment method that is not trivial, one also wanted to look at the signals that were not phase-aligned for comparison when looking at echo-prolongation as a function of depth. A method that reduces signal variability is averaging the individual signal envelopes instead of the full-waveform signals [12]. Hence, the twenty individual signals were Hilbert transformed, the absolute value was used to get the signal envelope, and then the average of the twenty envelopes were plotted in dB relative to the maximal value.

4.6   Intensity curves

Intensity calculation assumes time-averaging over at least a period of the signal. In this work the intensity was calculated by simply squaring the signals without averaging over a time-interval. Strictly speaking this is not the intensity according to the definition of intensity, but is similar and therefore referred to as the intensity in this work. The intensity of the coherent signal was found by squaring the coherent signal, while the incoherent signal intensity was found by squaring the individual signals without phase-aligning, and then averaging. These intensities are plotted for the results of the averaged signals from the sand and clay surfaces in chapters 6 and 7.

(a) Coherent intensiy, mean curve.

(b) Incoherent intensity, mean curve.

(c) Coherent intensity, maximal envelope.
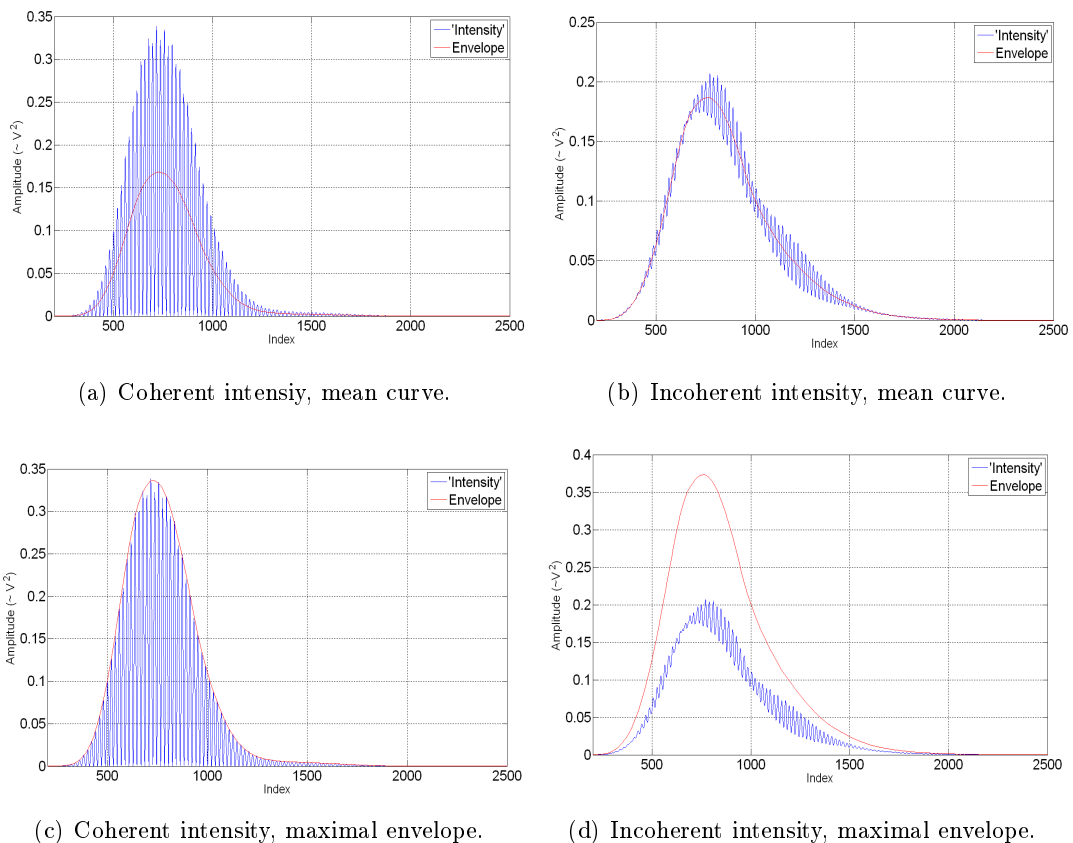
(d) Incoherent intensity, maximal envelope.

Figure 4.16: Finding the intensity envelopes, mean envelopes and envelopes tracing the peak values.

The intensity plots are further used in chapter 8 to calculate different energy and shape parameters. However, here the mean curves of the intensities were used. This was done by removing

the high-frequency components by Fourier transforming the respective intensity signals, replacing the high frequency portion of the frequency spectrum by zeroes and then finding the inverse Fourier transform. This gave the mean value of the signals, which is adequate when the shape parameters are calculated, see figures 4.16(a) and 4.16(b). When calculating the total energy, however, the envelopes were multiplied by two, to get the envelope tracing the peak values of the intensity curve for the averaged coherent intensity, see figure 4.16(c). Multiplying the envelope of the incoherent intensity curve by two, give the same result achieved by averaging the squared envelopes of each individual echo signal.

Chapter 5

Measurements on the copper reflector

The copper reflector has a thickness of 5 cm and a diameter of 20 cm. It is made from 99.99% pure copper, due to the well-defined characteristic impedance for this material compared to stainless steel. Christian Halvorsen [24] used this copper reflector for calibration of hydrophones in his master's thesis in 1982. In connection with Halvorsen's work, the surface was inspected at what was then called the Christian Michelsen Institute (CMI). It was found that the surface could be described as perfectly plane within an uncertainty of 10 µm, and that surface roughness was less than 5 µm. As [24] points out, the copper surface is exposed to corrosion when left in water over a period of time, hence the surface roughness may have changed since the inspection. However, the surface was polished before doing measurements, and should be plane enough for the measurements intended in this work.

5.1   Measurement setup

5.1.1   First measurements on copper

The first measurements on the metal reflector were done in January 2009. The reflector was placed on top of an old, empty PC-cabinet, placed on the bottom of the water tank. The reflector surface was adjusted to be horizontally plane. This could be done by pulling up or pressing down a stick mounted to one end of the copper reflector. The reflector was adjusted manually until achieving the strongest possible signal on the oscilloscope screen. The transducer was tilted so that the beam axis pointed vertically down towards the bottom. This was done by rotating the transducer through 5° about the assumed vertical beam axis, with steps of about 0.25°, using the motordriven system via the computer. The direction in which the rms-amplitude of the first part of the signal had the highest value, was assumed to be the angle giving normal incidence onto the reflector. The experimental setup discussed in section 4.1 was used for this experiment, with the 40 dB pre-amplifier but without the branching box. There was quite a large amount of noise, more than the usual amount of random noise experienced in the lab according to Halvor Hobæk. This made the signal on the oscilloscope screen fluctuate a great deal. Compensating, by letting the oscilloscope continuously average over 128 or 255 sweeps, improved the signal-to-noise ratio. The source of the noise was not identified, however, it seemed to improve over time. Hence, for later measurements continuously averaging over 63 sweeps gave a satisfactory signal.

### 5.1.2   Later measurements on copper

After measuring backscattered signals from both the sand and clay surfaces without seeing any systematic effect of echo lengthening as a function of water-depth, it was decided to go back to a less complex surface to see if this effect was present. A new set of measurements

of the echo received from the copper reflector, with better resolution and spanning over a larger range of distances between the copper reflector and the transducer, were carried out. To achieve greater distances, the copper reflector was placed right onto the bottom of the water tank. The copper reflector and the transducer was then finely tuned so that their surfaces were horizontal and parallell to eachother, obtaining normal incidence of the beam onto the reflector. The transducer was aligned using the same procedure discussed for the first set of measurements, see section 5.1.1. Then the reflected signals from two diametrically opposed points on the copper reflector were measured, located about 5 cm away from the midpoint of the reflector. The reflector was adjusted until these two signals were seen to be received with the same time delay. The reflector was then considered to be horizontal with respect to the transducer. The process of adjusting the transducer and the reflector was repeated a couple of times to achieve the best possible alignment. Four echoes could be observed on the oscilloscope screen when the distance between the transducer and the reflector was 13 cm. The experimental setup was the same as for the earlier measurements on the copper surface, except that the Ultrasonic Preamp 5660B seemed to distort the signal and was therefore replaced with the Ultrasonic Preamp 5670, see table 4.2. In addition, the branching box was used for these measurements. The burst length was increased to 30 cycles and the amplitude of the steady-state area of the received signal, with and without the pre-amplifier, was calculated. It was found that this amplifier increases the signal amplitude with a factor 4.82 at 5 MHz with this expertimental setup. This corresponds to approximately 13.7 dB.

5.2 Results and discussion

5.2.1 First measurements on copper

A burst consisting of 10 cycles with a frequency of 5 MHz, a burst period of 200 ms and a peak-to-peak amplitude of 0.5 V was applied by the signal generator. The first reflected echo from the copper reflector was measured at different water-depths, to see whether the duration of the returned signal changed as a function of depth. Finding the Hilbert transform of the full-waveform echo signal and plotting the absolute value of the Hilbert transform in dB, relative to the maximum value, as a function of time, give the signal envelope. The signal envelopes for the backscattered signals from the copper reflector at different water-depths, along with the linear plot of the effective echo duration as a function of water-depth, are shown in figure 5.1.
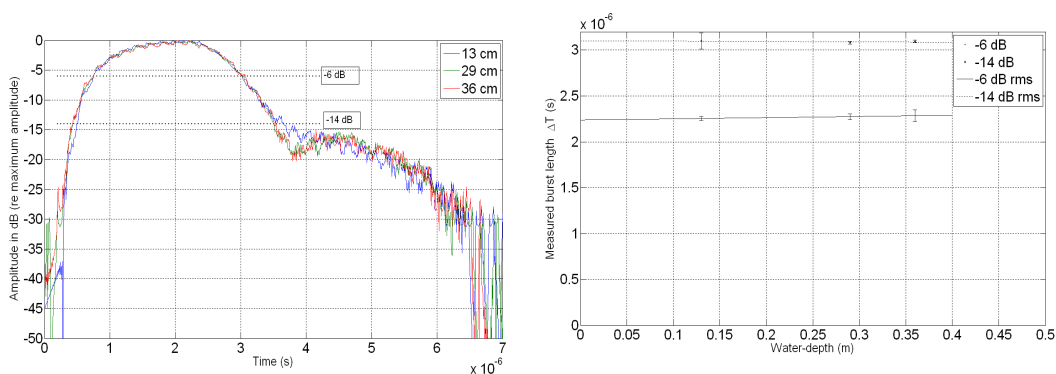
(a) Signal envelopes at different water-depths.   (b) Linear plot of burst length vs. water-depth.

Figure 5.1: Scattering from the copper surface at different water-depths, January 2009.

The effective echo durations measured at both the -6 dB and -14 dB levels are approximately equal for each depth, see figure 5.1(a). This is also seen in figure 5.1(b), as the linear plots are almost horizontal lines. The echo duration does not seem to increase linearly with water-depth, as expected following the discussion in section 2.4. This could be explained by the fact that for a smooth surface, the parts of the beam that hits at an angle away from the normal, is specularly reflected away from the transducer. However, due to the finite size of the reflector, secondary lobes and interference effects, a fraction of the beam should be scattered back to the source, following the discussion in 3.2.2 on backscattering from a finite surface. However, this may not be above the -6 dB level or even the -14 dB level. Below the -14 dB level the noise level is reached. Could better dynamics in the measurements show the effect of echo lengthening?

5.2.2 Later measurements on copper

A burst consisting of 10 cycles with a frequency of 5 MHz, a burst period of 200 ms and a peak-to-peak amplitude of 0.5 V, was applied by the signal generator. Measurements at different water-depths were taken. The different parts of the signal were recorded separately and the vertical scaling factor of the oscilloscope was adjusted for each recording, so that the signal covered as much of the oscilloscope screen as possible, thereby achieving better precision of the digitalization for each part. Also a better sampling frequency could be achieved, as the whole time signal did not have to cover the screen at one time, thereby increasing the resolution on the time-axis. Up to four different versions of the signal, with different resolution, were matched to give one signal. To match two signals, the first index n after a zero-crossing in the second signal was chosen manually. Knowing the difference in the time-delays of the two signals and the index n, it is possible to decide which part of the first signal should be picked, and the two signals can be matched at the zero-crossing. The matched signals can be seen in figure 5.2.
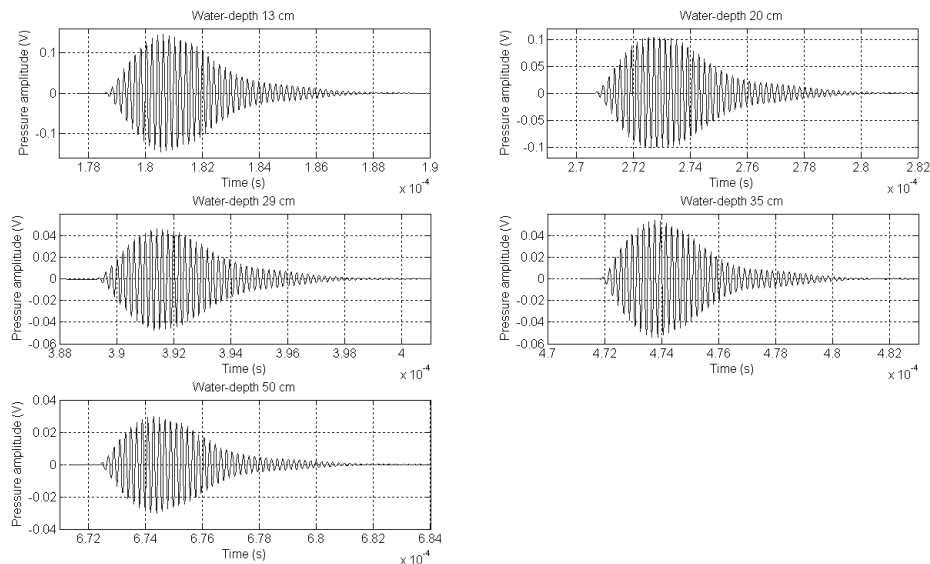

Figure 5.2: Echo signals from copper at different water-depths.

The time scale is adjusted according to the time-delay of the returned signal, accounting for the time the signal spends going from the transducer to the surface and back. The time-windows are of equal length for each water-depth, hence the lengths of the echo signals can be compared.

The echoes are seen to have approximately the same shape and duration. The duration of the echoes are approximately 9 µs, while the transmitted signal was 2 µs long plus some more due to ringing in the transducer. The amplitude decreases for increasing water-depths, except for the signal at 35 cm which has a slightly larger amplitude than the signal at 29 cm. The signal envelopes for each water-depth, and the linear plots of echo duration as a function of water-depth are plotted in figure 5.3.
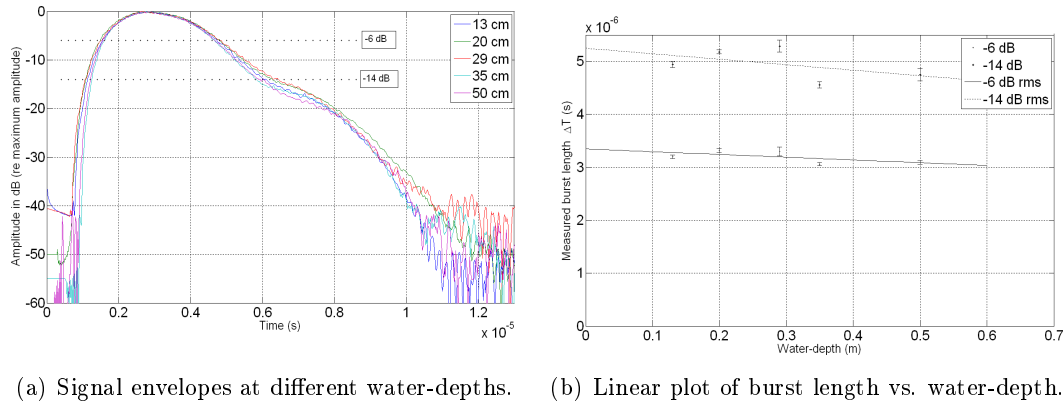
(a) Signal envelopes at different water-depths.   (b) Linear plot of burst length vs. water-depth.

Figure 5.3: Scattering from the copper surface at different water-depths, July 2009.

The effective echo durations are again seen to be approximately the same for all the depths measured, as was the result for the measurements done in January. The dynamics are better here, however, even at the lower pressure levels there does not seem to be a systematic increase of echo duration as the water-depth increases. The echo durations read from the signal envelope plots, for both the January and July measurements, are given in table 5.1. The uncertainties in echo durations from reading out values in the plots are estimated. These uncertainties varies between the different envelopes, as some of them fluctuates more around the chosen pressure levels than others.

Table 5.1: Effective echo durations from a copper reflector.

Water-depth	Measurements in January		Measurements in July	
	-6 dB	-14 dB	-6 dB	-14 dB
13 cm	2.26 ± 0.02 µs	3.10 ± 0.09 µs	3.20 ± 0.04 µs	4.94 ± 0.05 µs
20 cm	-	-	3.32 ± 0.04 µs	5.18 ± 0.04 µs
29 cm	2.28 ± 0.03 µs	3.08 ± 0.02 µs	3.30 ± 0.09 µs	5.29 ± 0.11 µs
36/35 cm	2.29 ± 0.06 µs	3.10 ± 0.02 µs	3.06 ± 0.03 µs	4.56 ± 0.06 µs
50 cm	-	-	3.09 ± 0.04 µs	4.75 ± 0.12 µs

The difference in effective echo durations for the measurements done in January and July, could possibly be explained by the fact that a different experimental setup was used. Another explanation could be that the method for setting up the reflector to be horizontal was better for the second set of measurements. The echo durations for different water-depths however, seem to be around the same value, the duration fluctuates a bit but there is no indication that it increases linearly with increasing water-depth, as discussed in section 2.4.

5.3 Copper reflector with sand particles

The copper reflector was then sprinkled with a few sand particles randomly distributed across the surface, as shown in figure 5.4. This was an attempt to see whether the effect of increasing echo duration with water-depth could be enhanced by the sand particles scattering sound back to the transducer.

Figure 5.4: Copper reflector sprinkled with sand.

The peak-to-peak amplitude of the 5 MHz signal from the signal generator was now set to 0.2 V, otherwise the experimental setup was the same as before, with the 13.7 dB pre-amplifier and the branching box. The signal envelopes and linear plots are shown in figure 5.5.

(a) Signal envelopes at different water-depths.

(b) Linear plot of burst length vs. water-depth.
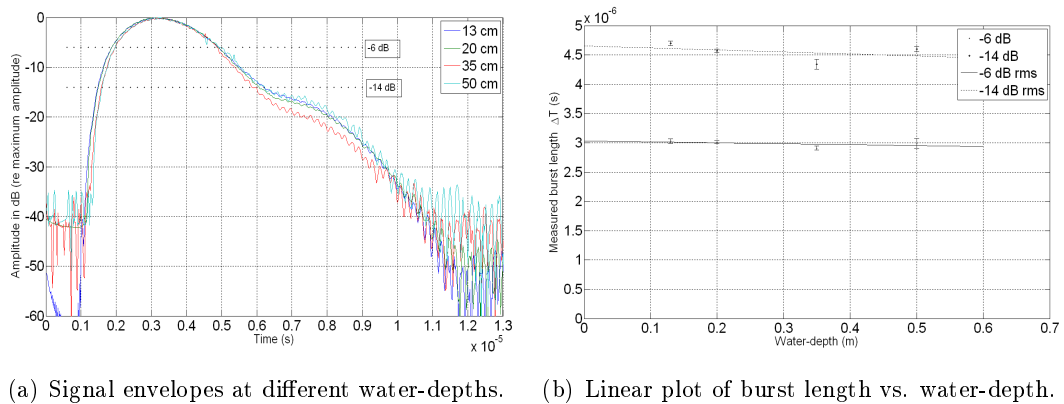
Figure 5.5: Scattering from the copper surface sprinkled with sand particles at different water-depths, July 2009.

The echo durations found from the plots in figure 5.5(a) are summarized in table 5.2. Again, the echo duration does not seem to increase with increasing water-depth. Rather it seems to be randomly spread around a constant value, with no correlation to water-depth. The echo durations lie around the same value as for the copper reflector without sand particles.

47

Table 5.2: Effective echo duration from a copper reflector with sand.

Water-depth	-6 dB	-14 dB
13 cm	3.03 ± 0.04 µs	4.70 ± 0.04 µs
20 cm	3.01 ± 0.03 µs	4.57 ± 0.03 µs
35 cm	2.91 ± 0.04 µs	4.34 ± 0.08 µs
50 cm	2.99 ± 0.08 µs	4.60 ± 0.05 µs

5.4 Expected echo durations for the different water-depths

According to the theory discussed in section 2.4, the echo duration should increase as depth increases. Putting values for θ_{-3dB} and θ_{-7dB}, found from the directivity plot in section 4.3, into the equations found in section 2.4, the expected increase in echo duration can be calculated. These values are shown in table 5.3 for some water-depths for each of the transducers.

Table 5.3: Expected increase in echo duration

Water-depth	5 MHz transducer		1.4 MHz transducer	
	Δt for θ_{-3dB}	Δt for θ_{-7dB}	Δt for θ_{-3dB}	Δt for θ_{-7dB}
13 cm	0.17 µs	0.34 µs	0.56 µs	1.30 µs
16 cm	0.20 µs	0.42 µs	0.69 µs	1.60 µs
20 cm	0.25 µs	0.53 µs	0.86 µs	2.00 µs
22 cm	0.28 µs	0.58 µs	0.95 µs	2.20 µs
35 cm	0.45 µs	0.92 µs	1.51 µs	3.51 µs
50 cm	0.64 µs	1.32 µs	2.16 µs	5.01 µs

This is the expected increase for each water-depth, meaning that the total duration should be the length of the transmitted burst plus this additional time period. For ten cycles of the 5 MHz signal, the burst length is 2 µs, whereas for the 1.4 MHz signal, ten cycles give a burst length of 7.14 µs. The increase in echo duration should be clearly visible in the plots of the signal envelopes, as the increase relative to the original burst length of the signal is fairly large. Also the increase between different water-depths are large enough that it should be visible in the plots.

48

Chapter 6

Measurements on a tray of sand

6.1 Preparation of the sand tray

Halvor Hobæk collected sand at a beach nearby, and it was left to dry for a few days. Several sieves were then used to separate the sand particles of different sizes. Six groups of particles were obtained: less than $125\,\text{µm}$, between $125 - 150\,\text{µm}$, between $150 - 250\,\text{µm}$, between $250 - 500\,\text{µm}$, between $500 - 1000\,\text{µm}$ and the remaining sandparticles. The remaining, larger sand particles were put in the bottom of a tray with dimensions $30 \times 40 \times 4$ cm. Then a layer of sand with particle-size between $500 - 1000\,\text{µm}$ was added, and finally a layer with particles sized between $250 - 500\,\text{µm}$ was added. This is referred to as the fine sand surface. The surface was carefully leveled after the addition of each layer. Further, the tray was placed in a larger vessel filled with water and left for 24 hours to get rid of air.

6.2 Measurement setup

The tray of sand was placed in the water tank by using two lengths of polyester cord, each rope being thread through holes in the tray and mounted on the side of the tank, leaving possibility for adjusting the depth position of the tray. A leveling instrument was placed on top of the sand tray, and the ends of the cords adjusted until the surface was considered sufficiently horizontal. The tilt of the transducer was then adjusted to obtain normal incidence onto the surface. Since the process of adjusting the cord lengths and making sure the surface was horizontal was quite time-consuming, it was easier and faster to adjust the height of the transducer to obtain different distances between the transducer and the sand once the tray was placed in the water tank. The experimental setup used for these measurements was the same as that described in chapter 5 for the first measurements on the copper reflector, except that the amplifier on the receiving side seemed to distort the signal and was therefore replaced by a home made amplifier. This amplifier stopped working after a few days, and it was decided to do the measurements without any amplification of the received signal. Measurements were therefore only done for water-depths up to 22 cm, as greater depths gave too low resolution of the signal on the oscilloscope.

6.2.1 Difficulties in leveling the sand surface and algae growth

It was difficult to place the tray of sand in the water tank without disturbing the surface. Sand particles came off and was disposed off on other parts of the surface, making the surface more rough. Leveling of the surface while the tray was in the water tank proved difficult as some of the sand particles seemed to adhere to each other and was dragged along with the aluminium ruler used as a leveler, leaving small holes on the surface. Taking the sand tray out of the

water tank for leveling was considered the only solution. An electrical drill was put into one of the holes at the edge of the tray, in an attempt to stir the tray enough to make the surface level out. However, this led to larger particles from the bottom layers rising to the surface. Hence, the layering of the sand was somewhat disturbed. Further, a metal plate was dragged back and forth across the surface. This seemed to give a satisfactory result, however, there were still some small holes randomly spread across the surface. These holes were estimated to be approximately 1 mm deep, and to have a diameter of about $3 - 4$ mm.

Another unforeseen problem arose when the sand surface was exposed to a burst consisting of ten periods of a sine wave with a frequency of 5 MHz, a peak-to-peak amplitude of 0.5 V and a burst period of 200 ms, amplified by the 50 dB power amplifier. After a while the radiation pressure at the interface managed to make a hole with a diameter of about 1 cm in the sand surface. The sand tray was once again taken out of the tank for leveling, and the peak-to-peak amplitude of the sound burst was lowered to 0.2 V in the successive measurements. After leaving the sand tray in the water tank for a week, a layer of algae was starting to grow on top of the sand surface. The sand tray was again taken out of the tank, and a bottle of chlorine was poured over it. The tray was left for an hour before being replaced back into the tank. How much the algae layer was actually influencing the measurements was not looked into, however, the process of adding chlorine was repeated when the algae growth started to return.

6.3 Measurements on a coarser sand bottom

Sand with particle size between $500 - 1000$ μm was added in a small patch, due to only small amounts of sand left, on top of the leveled sand surface. This is referred to as the coarse sand surface. The area covered was about 10×10 cm. It should be more than large enough considering the small area insonified by the main lobe of the incident wave. With an angle of first minima of $3.65°$, the radius of the area covered by the main lobe on the sand surface, with the transducer in a distance of 22 cm from the tray, will be approximately $r = (22 \text{ cm}) \tan(3.65°) = 1.4$ cm. The returned signal was measured at different water-depths, as for the fine sand surface. However, at this point of time the method of stacking signals to find the coherent signal, discussed in section 4.5.1, was looked into. This was done only at the 20 cm water-depth.

6.4 Results and discussion of the first measurements on sand

According to the geometric considerations done in section 2.4 on echo-prolongation as a function of depth, the effective echo duration should increase linearly as the water-depth increases. The first echo from the sand tray was measured at different water-depths, to see whether the duration of the returned signal changed as a function of depth. Hilbert transformation of the full-waveform echo signal, and plotting the absolute value in dB, relative to the maximum value, as a function of time, give the signal envelope. The signal envelopes of the backscattered signals from the fine sand surface at different water-depths, and the corresponding linear plot of the effective burst-length as a function of water-depth, are shown in figure 6.1. Here, the -12 dB level was considered instead of the -14 dB level, due to poorer dynamics for these measurements. In these measurement only individual signals at each water-depth were considered, signal fluctuation was therefore not accounted for.

(a) Signal envelopes at different water-depths.   (b) Linear plot of burst length vs. water-depth.
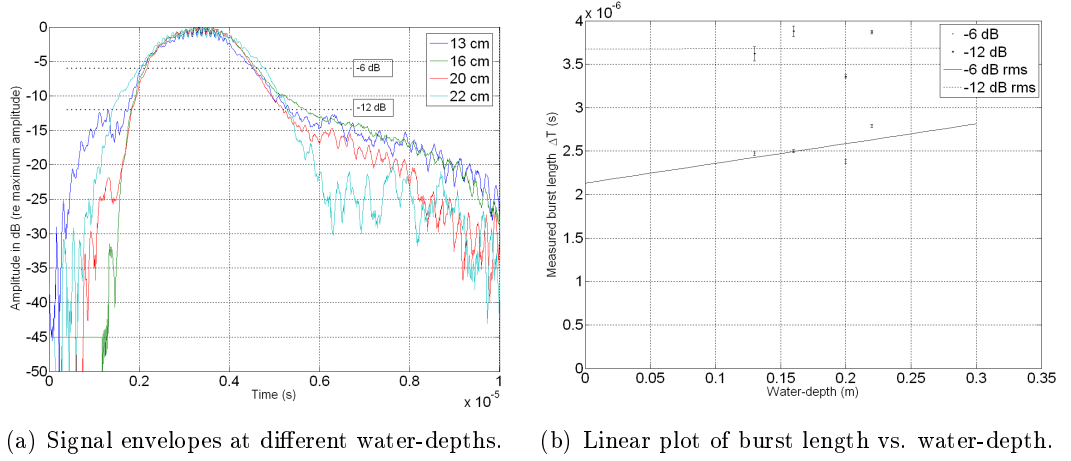
Figure 6.1: Scattering from the fine sand surface at different water-depths, individual signals.

The signal envelopes of the backscattered signals from the coarse sand surface at different water-depths and the correspondig linear plot of the effective echo duration as a function of water-depth, are shown in figure 6.2. As stacking of signals to account for signal fluctuation was only looked at for the 20 cm water-depth, it is individual signals that are considered here.

(a) Signal envelopes at different water-depths.   (b) Linear plot of burst length vs. water-depth.
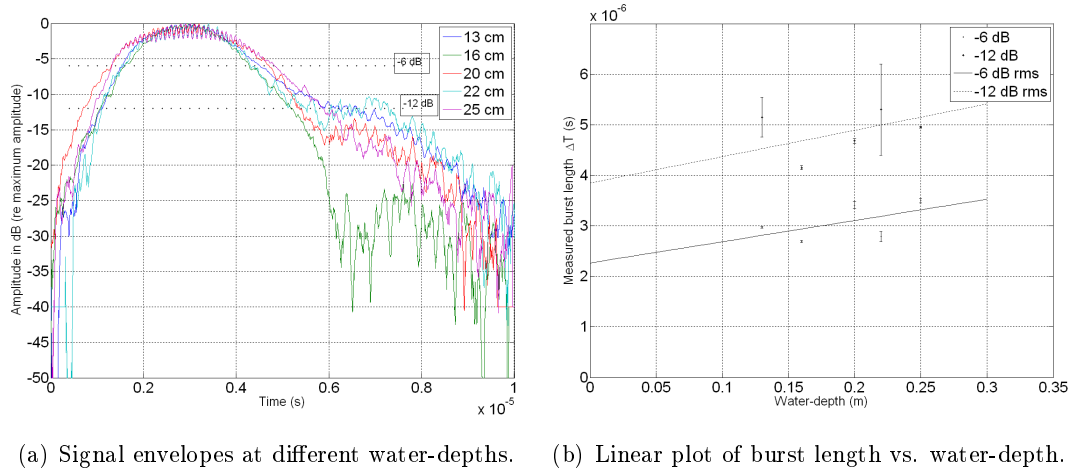
Figure 6.2: Scattering from the coarse sand surface at different water-depths, individual signals.

The values of the effective echo durations for the -6 dB and the -12 dB level, read from the signal envelope plots, along with the estimated uncertainties, are summarized in table 6.1.

Table 6.1: Effective echo durations from the signal envelope plot, individual signals.

	Fine sand surface		Coarse sand surface	
Water-depth	-6 dB data	-12 dB data	-6 dB data	-12 dB data
13 cm	2.47 ± 0.02 µs	3.62 ± 0.08 µs	2.97 ± 0.02 µs	5.15 ± 0.39 µs
16 cm	2.50 ± 0.02 µs	3.88 ± 0.06 µs	2.69 ± 0.02 µs	4.15 ± 0.04 µs
20 cm	2.38 ± 0.02 µs	3.36 ± 0.02 µs	3.41 ± 0.07 µs	4.68 ± 0.05 µs
22 cm	2.79 ± 0.02 µs	3.87 ± 0.02 µs	2.79 ± 0.10 µs	5.30 ± 0.90 µs
25 cm	-	-	3.50 ± 0.05 µs	4.95 ± 0.02 µs

The values in table 6.1 were used to make the linear plots in figures 6.1(b) and 6.2(b). The linear plots together with the equations in section 2.4, were used to calculate values for the effective angle and effective burst length with their respective uncertainties. The results are summarized in table 6.2.

Table 6.2: Effective angle and effective length of the burst, individual signals.

	Fine sand surface		Coarse sand surface	
	-6 dB data	-12 dB data	-6 dB data	-12 dB data
α	0.0017 ± 0.0020	0.00003 ± 0.00320	0.0032 ± 0.0028	0.0039 ± 0.0047
D	3.2 ± 0.7 mm	5.5 ± 1.2 mm	3.4 ± 1.1 mm	5.8 ± 1.9 mm
θ	$3.3° \pm 2.0°$	$0.5° \pm 22.0°$	$4.5° \pm 2.0°$	$5.1° \pm 3.0°$

D_{-12dB} is expected to be larger than D_{-6dB} since more of the burst is included. Likewise, one would expect that the angle θ increases as the treshold is set lower, including more of the outer parts of the beam. However, for the fine sand surface, the -12 dB data show no systematic increase in echo duration with depth, and the linear plot for these data is almost a horizontal line. However, one should also consider the increased uncertainty in the -12 dB measurements in comparison with the -6 dB measurements. α is the coefficient giving the rate of increase of the echo duration, and is a constant for a given transducer. For the 5 MHz transducer, the expected coefficient is $\alpha_{-3dB} = 0.00095$ for the -3 dB angle and $\alpha_{-6dB} = 0.0018$ for the -6 dB angle, using the theoretical expressions in section 2.4. For the measurements, the increase in echo duration is seen to be larger than expected, except at the -12 dB level for the fine surface, comparing the values for α from table 6.2 to the theoretically expected coefficients. For ten cycles of a 5 MHz burst, the length of the transmitted burst is 3 mm, plus some more due to ringing in the transducer. Hence, the effective burst lengths from the -6 dB data are reasonable.

6.4.1 Results of stacking the signals from the coarse sand surface

After phase-aligning the time signals taken in twenty different positions on the coarse sand surface, with the transducer in a distance of 20 cm, the coherent signal could be found by averaging. See figure 6.3(a), where the coherent signal and standard deviation of the coherent signal is plotted. In figure 6.3(b), the intensity of the coherent signal is compared with the intensity of the incoherent signal. The intensities were found by the method discussed in section 4.6.
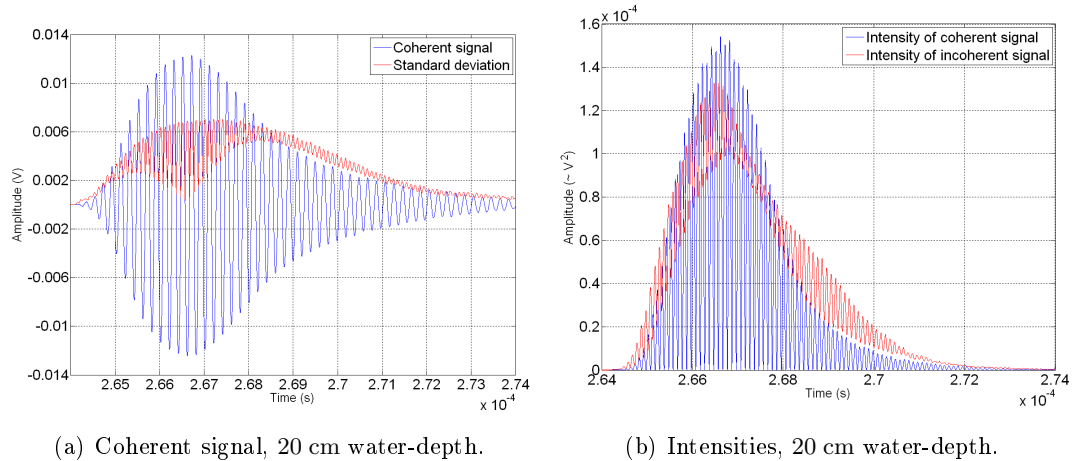
(a) Coherent signal, 20 cm water-depth.　　(b) Intensities, 20 cm water-depth.

Figure 6.3: Stacked signals from the coarse sand surface, measured with the 5 MHz transducer.

6.5　Later measurements on sand

It was decided to do a new set of measurements on sand, both to check some of the previous results and to do some additional measurements. This time, signals were taken in twenty different positions for each water-depth, so that the coherent signals could be compared. There was also great variation in the signals from the fine sand surface, hence, it was decided to stack the signals from this surface as well. The signal from the fine sand surface was also measured at twenty different positions. In addition, a set of measurements was done on an even coarser sand surface. It was also desirable to get measurements for a greater range of water-depths by using a pre-amplifier. In addition, it was decided to do measurements using a different transducer, to see which results this would lead to. A 1.4 MHz transducer with a total beam-width of approximately 20°, therefore covering more of the surface, was chosen for this purpose. All of these measurements were done applying a burst from the signal generator with a peak-to-peak amplitude of 0.2 V, which was then amplified 50 dB by the power amplifier.

6.5.1　Measurement setup

To avoid algae-growth, the sand was boiled, left to dry, and then sieved following the same procedure described in section 6.1. The largest particles with grain size above 1 mm (typically $0.2 - 0.7$ cm) were placed in the bottom of the tray, and measurements were done with the 5 MHz transducer only. This surface is referred to as the gravel surface. Then a layer of sand with particle-size between $500 - 1000$ μm was added. This surface is referred to as the coarse sand surface. Measurements were done with both transducers before adding the layer of particles sized between $250 - 500$ μm, which is referred to as the fine sand surface. Again, measurements were done with both transducers. The surface was carefully leveled after the addition of each layer. For the gravel and coarse sand it was fairly easy to get the surfaces plane by shaking the tray while the sand was still dry. However, for the fine sand surface, the sand got wet when it came in contact with the coarser sand, and it was harder to get an even surface. This can be seen in figure 6.4(c). The tray was placed in a larger vessel filled with water and left for 24 hours to get rid of air. The tray of sand was now placed directly onto the bottom of the tank. For the gravel and coarse sand surfaces, the 60 dB pre-amplifier was used when measuring with the 5 MHz transducer. However, for the rest of the measurements the amplification needed to be stepped down to 40 dB, to avoid distortion of the signals. The experimental setup was the same as discussed in section 4.1, with the branching

53

box. Mistakenly, the high-pass filter, which was set with a cut-off frequency of 2 MHz for the measurements with the 5 MHz transducer, was left with the same cut-off frequency for the measurements done with the 1.4 MHz transducer. There was not enough time to repeat these measurements, however, an attempt was made to adjust the already measured signals. This did not leave a satisfactory result, which is further discussed in section 6.7.
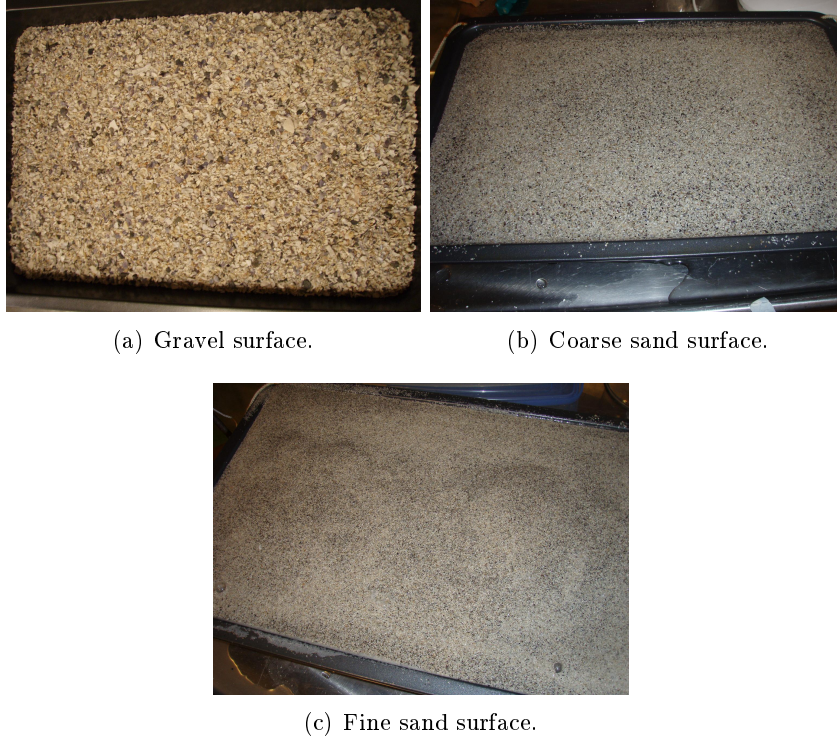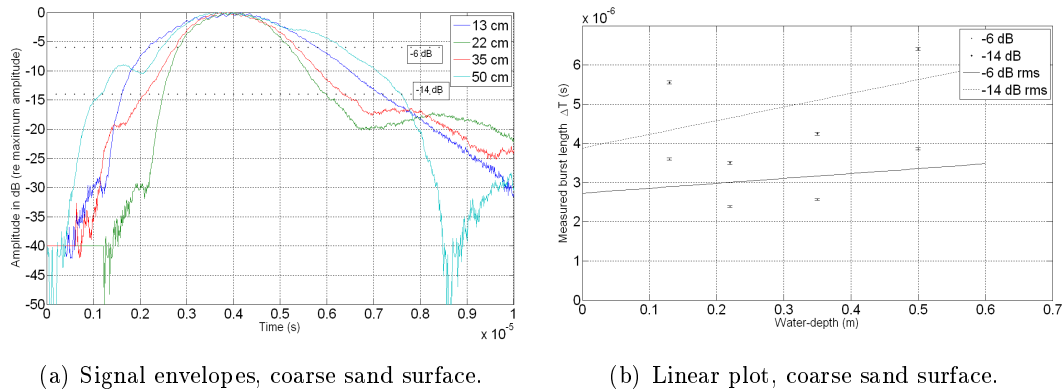

(a) Gravel surface.   (b) Coarse sand surface.

(c) Fine sand surface.

Figure 6.4: The sand surfaces that were used for measurements.

6.5.2 Results of individual signals

As well as stacking the signals taken at twenty different positions on the surface, individual signals taken in a specific position, that was the same for each water-depth, were also compared. This was only done for the coarse and fine sand surfaces. The results of the individual measured signals for the 5 MHz transducer, are plotted in figure 6.5.

(a) Signal envelopes, coarse sand surface.   (b) Linear plot, coarse sand surface.

(c) Signal envelopes, fine sand surface.

(d) Linear plot, fine sand surface.
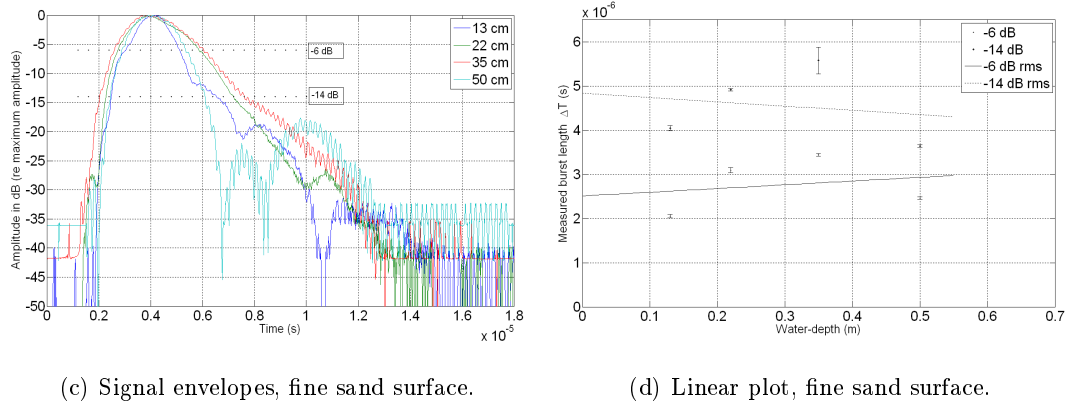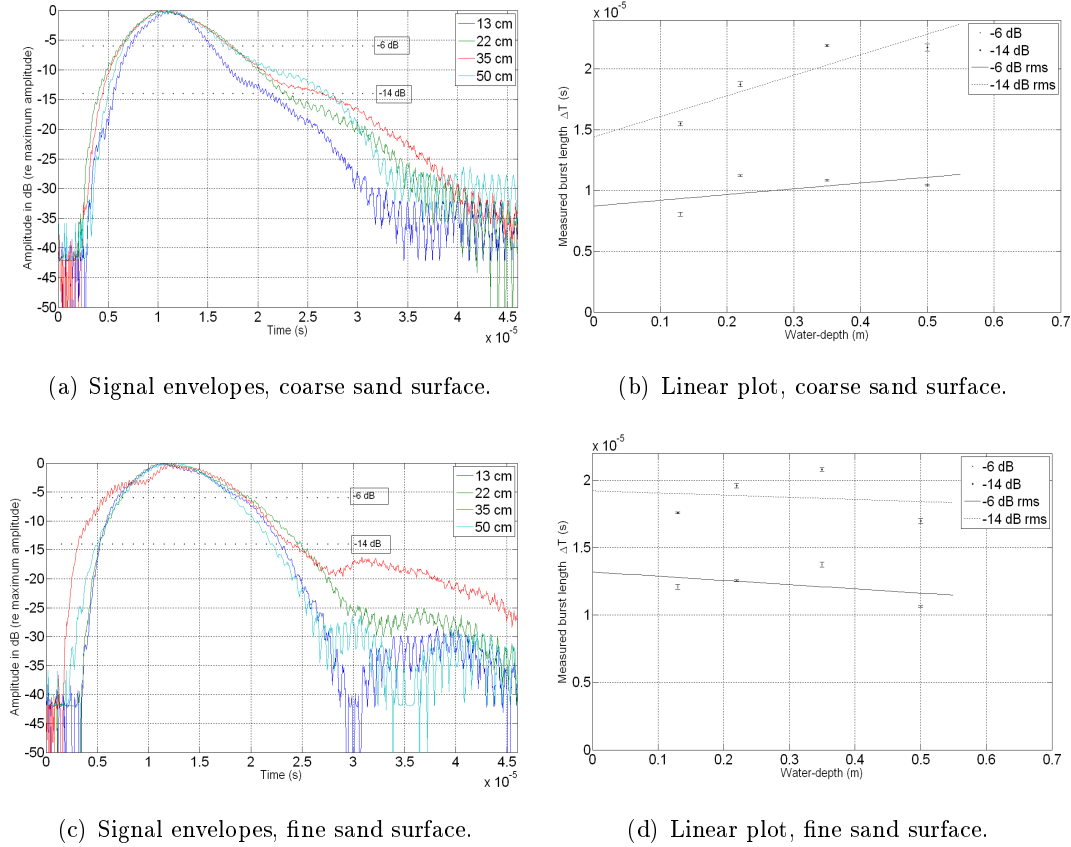
Figure 6.5: Signal envelopes and corresponding linear plots of the effective echo duration as a function of water-depth, for measurements taken with the 5 MHz transducer. Individual scattered signals from sand with different grain size.

The values of the effective echo durations, read from figures 6.5(a) and 6.5(c) are summarized in table 6.3.

Table 6.3: Effective echo durations, 5 MHz transducer, individual signals.

Water-depth	Coarse sand surface		Fine sand surface	
	-6 dB data	-14 dB data	-6 dB data	-14 dB data
13 cm	3.60 ± 0.03 µs	5.55 ± 0.04 µs	2.06 ± 0.04 µs	4.05 ± 0.06 µs
22 cm	2.39 ± 0.02 µs	3.50 ± 0.04 µs	3.10 ± 0.06 µs	4.92 ± 0.03 µs
35 cm	2.57 ± 0.02 µs	4.25 ± 0.04 µs	3.44 ± 0.03 µs	5.58 ± 0.30 µs
50 cm	3.86 ± 0.03 µs	6.41 ± 0.04 µs	2.46 ± 0.03 µs	3.64 ± 0.03 µs

These results were used to make the linear plots in figures 6.5(b) and 6.5(d), which together with the equations in section 2.4 were used to calculate values for the effective angle and the effective length of the burst with their respective uncertainties. The results can be found in table 6.4.

Table 6.4: Effective angle and effective burst length, 5 MHz transducer, individual signals.

	Coarse sand surface		Fine sand surface	
	-6 dB data	-14 dB data	-6 dB data	-14 dB data
α	0.0009 ± 0.0023	0.0026 ± 0.0039	0.0006 ± 0.0020	-0.0007 ± 0.0028
D	4.1 ± 1.5 mm	5.8 ± 2.6 mm	3.8 ± 1.3 mm	7.3 ± 1.9 mm
θ	$2.5° \pm 3.1°$	$4.1° \pm 3.1°$	$2.0° \pm 3.2°$	-

Within the uncertainty bounds, the -6 dB data correspond to the -6 dB data in table 6.2, which represents the earlier measurements on sand. The linear plots show that the measurement points are located far from the straight line, leading to large uncertainties. For the -14 dB data for the fine sand surface, α has a negative value, which leads to an imaginary value for the angle θ. It is just the last measurement in the linear plot that makes the coefficient of the line negative. Since the individual signals at each water-depth varies a great deal in both shape and strength, this might also affect the duration of the echo at a certain level. Hence, comparing envelopes of individual signals might involve too large uncertainties to draw any conclusions.

The -6 dB data correspond to the θ_{-3dB} angle, which was read from the directivity plot for the 5 MHz transducer to be $2.50° \pm 0.60°$. The -14 dB data corresponds to the θ_{-7dB} angle, which was read from the directivity plot for the 5 MHz transducer to be $3.60° \pm 0.60°$. Especially for the coarse sand, the effective angle θ_{-3dB} found from these measurements correspond well with the angle found from the directivity plot, while the -14 *dB* data give a bit higer values for α and θ than what is expected. The effective burst length, D, should be compared to the length of the signal, which for the 5 MHz transducer with a 10 cycle burst is 3 mm plus some more due to ringing in the transducer.

The results of the individual signals, for the 1.4 MHz transducer, are plotted in figure 6.6.

(a) Signal envelopes, coarse sand surface.

(b) Linear plot, coarse sand surface.

(c) Signal envelopes, fine sand surface.

(d) Linear plot, fine sand surface.

Figure 6.6: Signal envelopes and the corresponding linear plots of the effective echo duration as a function of water-depth, for measurements taken with the 1.4 MHz transducer. Individual scattered signals from sand with different grain size.

The values of the effective echo durations, read from figures 6.6(a) and 6.6(c) are summarized in table 6.5.

Table 6.5: Effective echo durations, 1.4 MHz transducer, individual signals.

	Coarse sand surface		Fine sand surface	
Water-depth	-6 dB data	-14 dB data	-6 dB data	-14 dB data
13 cm	8.05 ± 0.18 μs	15.48 ± 0.16 μs	12.10 ± 0.18 μs	17.60 ± 0.07 μs
22 cm	11.20 ± 0.07 μs	18.73 ± 0.21 μs	12.55 ± 0.07 μs	19.60 ± 0.18 μs
35 cm	10.85 ± 0.07 μs	21.90 ± 0.09 μs	13.75 ± 0.18 μs	20.80 ± 0.14 μs
50 cm	10.45 ± 0.07 μs	21.75 ± 0.28 μs	10.65 ± 0.07 μs	16.98 ± 0.21 μs

These results were used to make the linear plots in figures 6.6(b) and 6.6(d), which together with the equations in section 2.4 were used to calculate values for the effective angle and the effective length of the burst with their respective uncertainties. The results can be found in table 6.6.

Table 6.6: Effective angle and effective burst length, 1.4 MHz transducer, individual signals.

	Coarse sand surface		Fine sand surface	
	-6 dB data	-14 dB data	-6 dB data	-14 dB data
α	0.0035 ± 0.0040	0.013 ± 0.004	-0.0023 ± 0.0039	-0.0012 ± 0.0058
D	13.1 ± 2.6 mm	21.6 ± 2.9 mm	19.8 ± 2.6 mm	28.8 ± 3.8 mm
θ	$4.8° \pm 2.7°$	$9.1° \pm 1.6°$	-	-

For the fine sand surface both the -6 dB and the -14 dB linear plots have a negative gradient. As for the 5 MHz transducer, it is only the measured echo duration at the 50 cm water-depth that causes the gradients to be negative. What causes this reduction in echo duration at this depth is unknown. The -6 dB data correspond to the θ_{-3dB} angle, which was read from the directivity plot for the 1.4 MHz transducer to be $4.60° \pm 0.40°$. The -14 dB data correspond to the θ_{-7dB} angle, which was read from the directivity plot for the 1.4 MHz transducer to be $7.00° \pm 0.40°$. Again the correspondence between the effective angle θ_{-3dB} found from these measurements and the angle found from the directivity plot seem to be good for the coarse sand surface, while the -14 dB data give a bit higher values of α and θ than expected. The effective burst length, D, should be compared to the length of the signal, which for the 1.4 MHz transducer with a 10 cycle burst, is 10.7 mm plus some more due to ringing in the transducer.

6.5.3 Results of the stacked signals for the 5 MHz transducer

The signals were stacked following the procedure discussed in section 4.5. The coherent signals were found, as well the intensities of both the coherent and incoherent signals. The intensities were found by the method discussed in section 4.6. The result of the stacked signals from the gravel surface measured with the 5 MHz transducer for different water-depths, are plotted in figure 6.7.
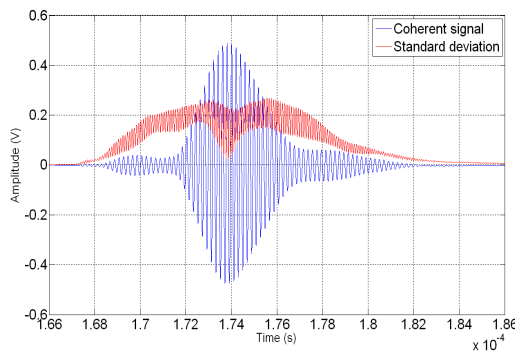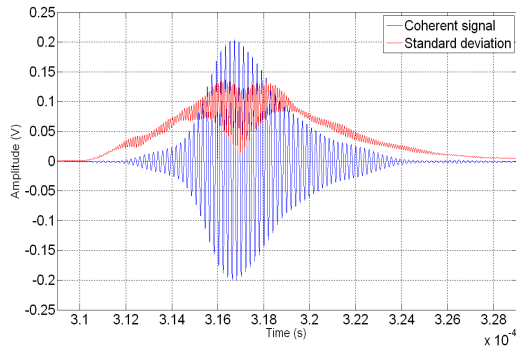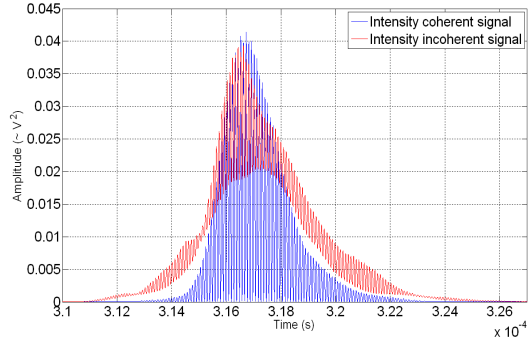

(a) Coherent signal, 13 cm.
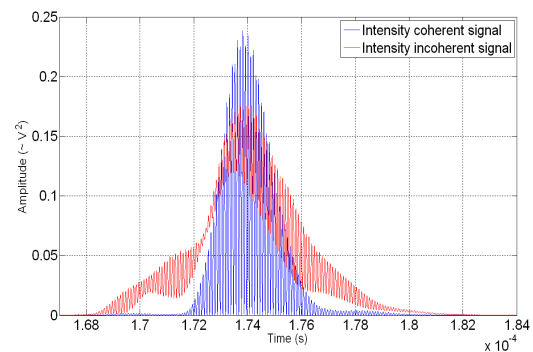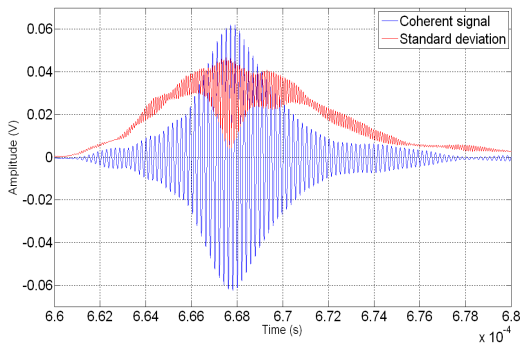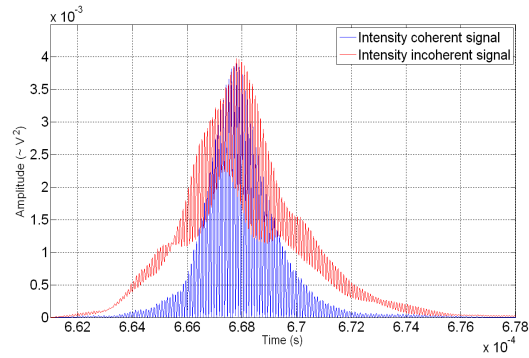
(b) Intensitities, 13 cm.

(c) Coherent signal, 22 cm.
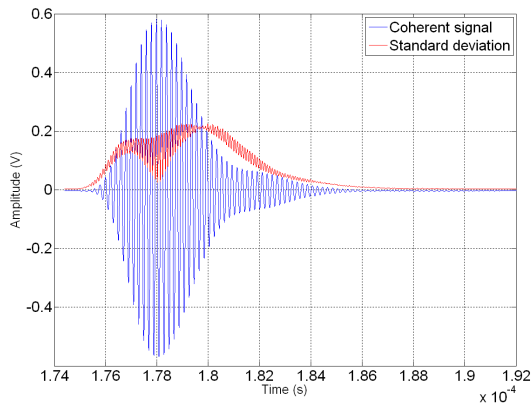

(d) Intensities, 22 cm.

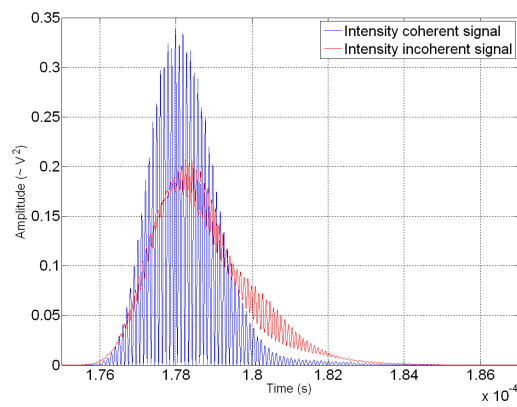

(e) Coherent signal, 50 cm.

(f) Intensities, 50 cm.

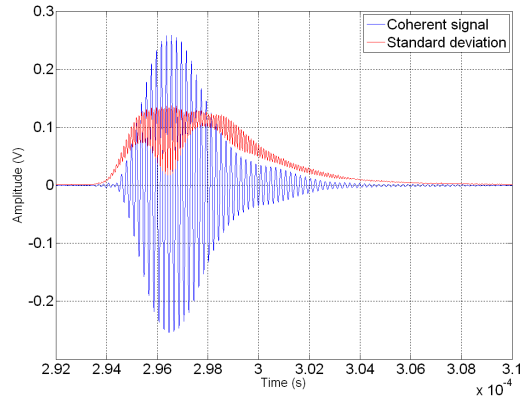Figure 6.7: Stacked signals from the gravel surface, 5 MHz transducer.

The results of the stacked signals from the coarse sand surface measured with the 5 MHz transducer for different water-depths, are plotted in figure 6.8.
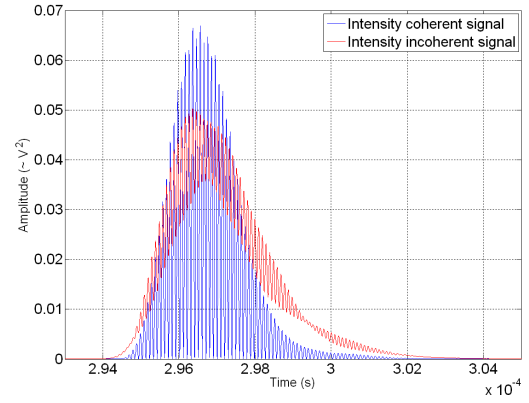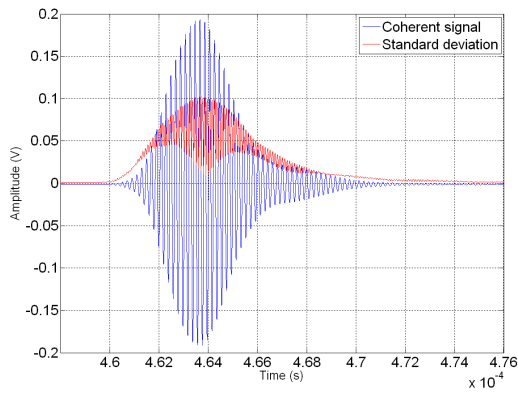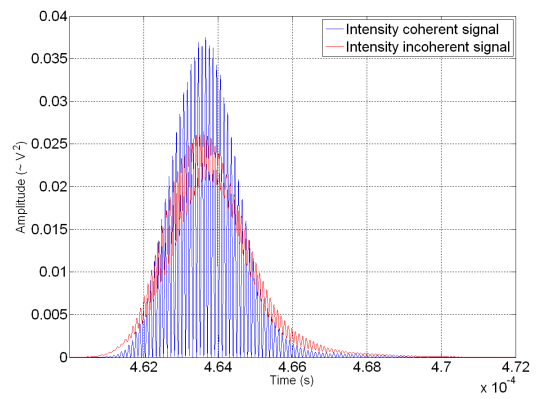

(a) Coherent signal, 13 cm.

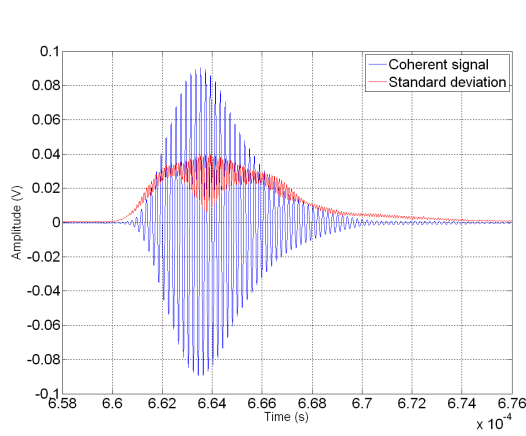(b) Intensities, 13 cm.

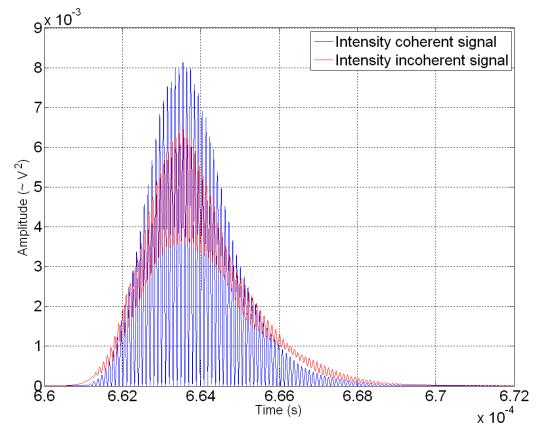(c) Coherent signal, 22 cm.

(d) Intensitities, 22 cm.

(e) Coherent signal, 35 cm.

(f) Intensitities, 35 cm.

(g) Coherent signal, 50 cm.
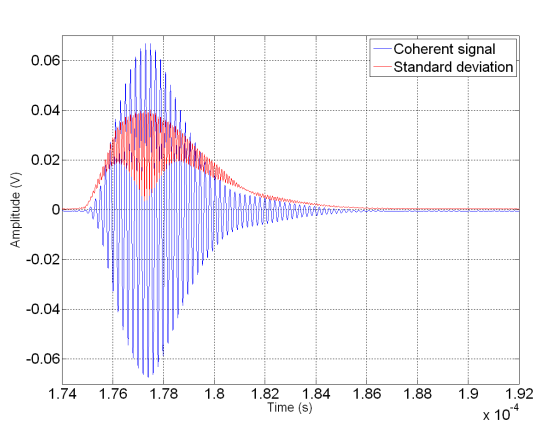
(h) Intensitities, 50 cm.

Figure 6.8: Stacked signals from the coarse sand surface, 5 MHz transducer.

The results of the stacked signals from the fine sand surface measured with the 5 MHz transducer for different water-depths, are plotted in figure 6.9.

(a) Coherent signal, 13 cm.

(b) Intensities, 13 cm.

(c) Coherent signal, 22 cm.

(d) Intensities, 22 cm.

(e) Coherent signal, 35 cm.

(f) Intensities, 35 cm.
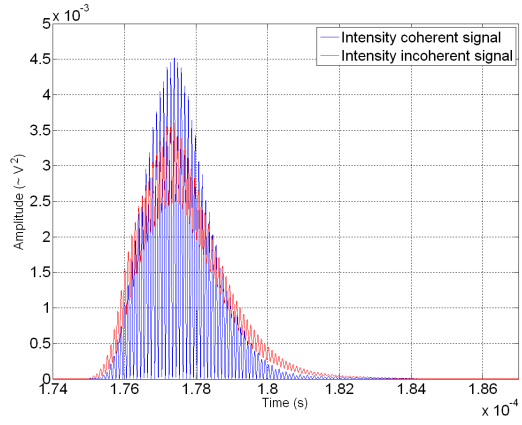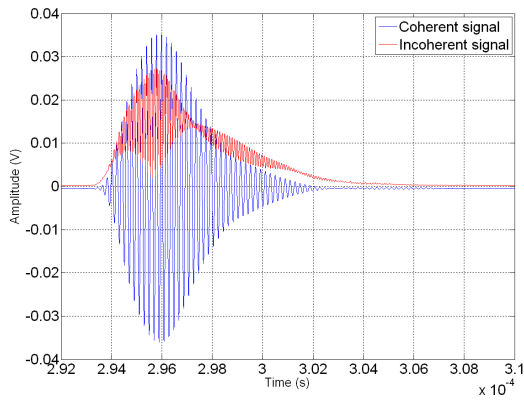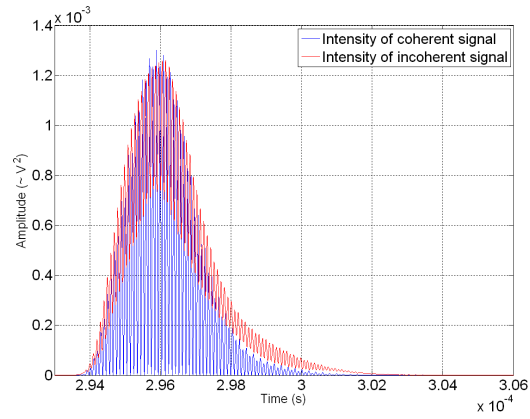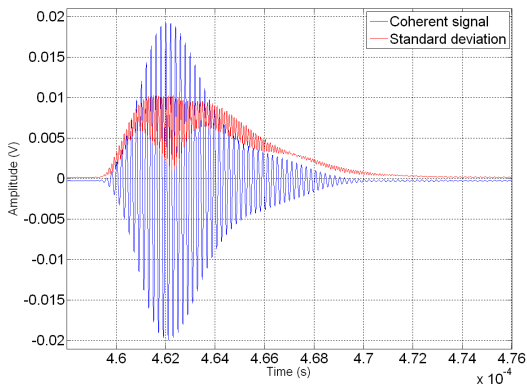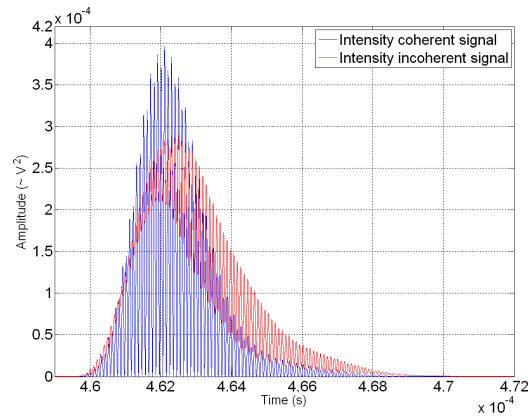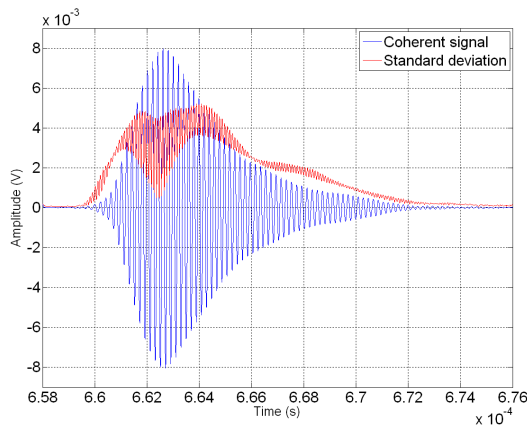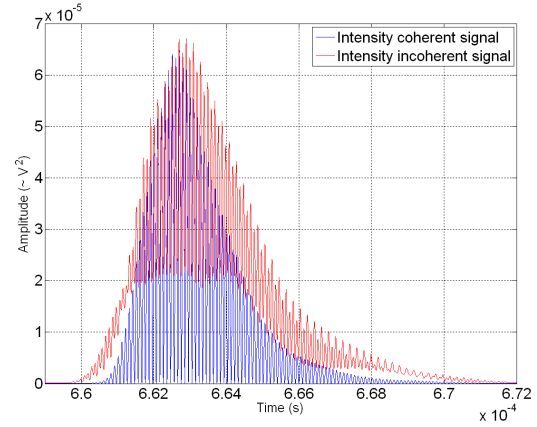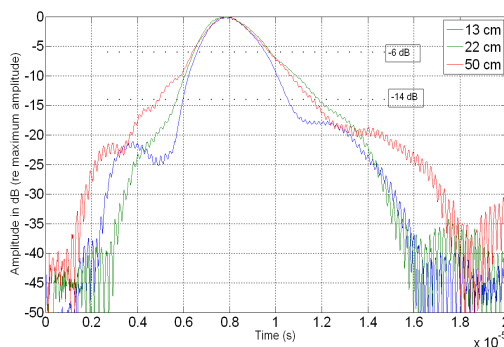
(g) Coherent signal, 50 cm.

(h) Intensitities, 50 cm.

Figure 6.9: Stacked signals from the fine sand surface, 5 MHz transducer.

The amplitudes of the signals from the gravel and coarse sand surfaces should not be compared to the amplitudes of the signals from the fine sand surface, as the signals from the gravel and coarse sand surfaces were amplified by 60 dB, while the signals from the fine sand surface were amplified by 40 dB. Expanding the applied burst to 30 cycles and then measuring the rms-amplitude of the steady-state, with and without the pre-amplifier, the amplification factors could be estimated. For the 5 MHz transducer, the 40 dB pre-amplifier amplified the signal by a factor of 42, which is approximately 32.5 dB. The 60 dB pre-amplifier amplified the signal by a factor of 310, which is approximately 50 dB. The amplitudes of the coherent signals from the gravel, coarse sand and fine sand surfaces may then be compared, by multiplying the amplitude of the signals from the fine sand surface by $310/42 \simeq 7.38$. The amplitude is higher for the coarse sand surface than the fine sand surface, except at the 22 cm water-depth, where the amplitudes seem to be about equal for the two surfaces. The amplitude is consistently a bit smaller for the gravel surface than for the fine sand surface. The coarse sand surface is expected to be a stronger scatterer, because of the increased roughness of the surface compared to the fine sand. The gravel surface, however, consists of very large particles compared to the wavelength of the incoming sound, and hence scatters the sound more diffusely, which could explain why the amplitude is less for the signals from this surface.

The coherent signal envelopes and the averaged envelopes (found without phase-aligning the individual signals) are plotted in figure 6.10, for the different sand surfaces.
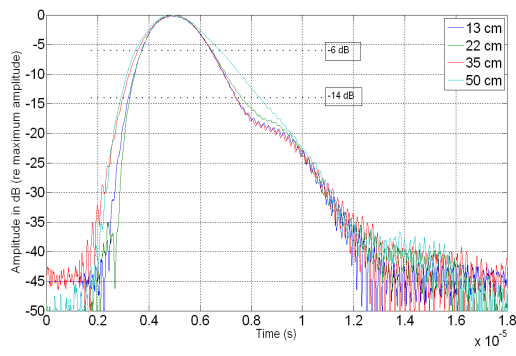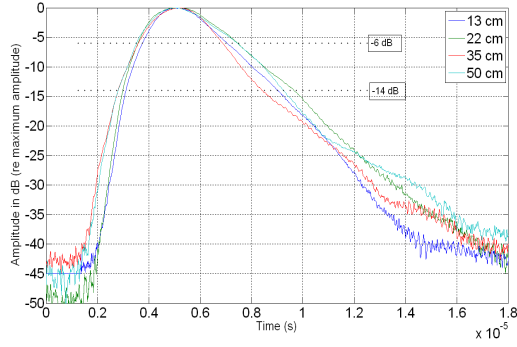

(a) Gravel surface, coherent signals.
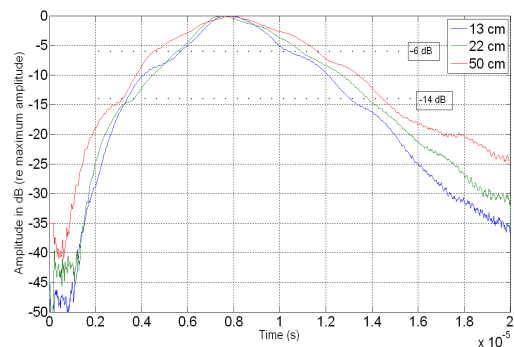
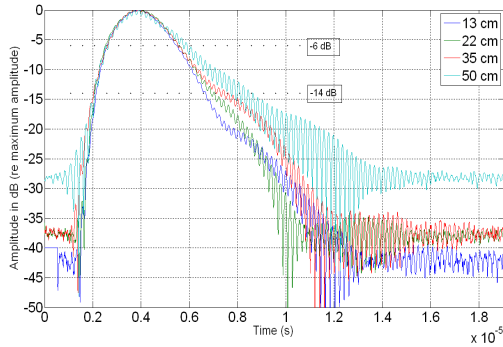(b) Gravel surface, averaged envelopes.

(c) Coarse sand surface, coherent signals.

(d) Coarse sand surface, averaged envelopes.

(e) Fine sand surface, coherent signals.
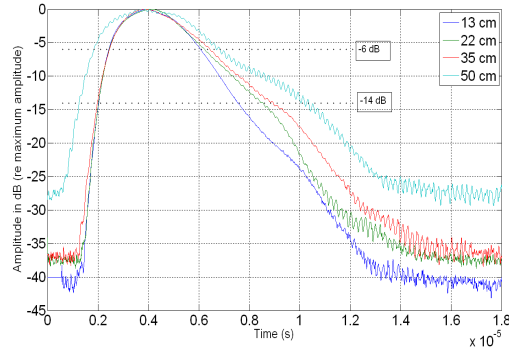
(f) Fine sand surface, averaged envelopes.

Figure 6.10: Coherent signal envelopes and averaged envelopes, 5 MHz transducer.

The values of the effective echo durations, read from figure 6.10 are summarized in table 6.7.

Table 6.7: Effective echo durations from the signal envelope plots, 5 MHz transducer.

Water-depth	Gravel surface		Coarse sand surface		Fine sand surface	
	-6 dB data [μs]	-14 dB data [μs]	-6 dB data [μs]	-14 dB data [μs]	-6 dB data [μs]	-14 dB data [μs]
Coherent stacked signals:						
13 cm	2.97 ± 0.02	4.55 ± 0.02	2.71 ± 0.02	4.19 ± 0.02	2.91 ± 0.02	4.55 ± 0.02
22 cm	3.32 ± 0.02	6.18 ± 0.02	2.74 ± 0.02	4.34 ± 0.02	3.03 ± 0.02	4.90 ± 0.09
35 cm	-	-	2.85 ± 0.02	4.46 ± 0.02	2.91 ± 0.02	5.34 ± 0.26
50 cm	3.37 ± 0.02	6.59 ± 0.02	3.31 ± 0.02	5.45 ± 0.02	3.18 ± 0.09	6.12 ± 0.46
Averaged envelopes:						
13 cm	4.66 ± 0.02	9.68 ± 0.02	3.31 ± 0.02	5.93 ± 0.02	3.63 ± 0.02	5.53 ± 0.02
22 cm	5.38 ± 0.02	10.13 ± 0.02	3.88 ± 0.02	6.67 ± 0.02	3.78 ± 0.02	6.33 ± 0.20
35 cm	-	-	3.29 ± 0.02	5.61 ± 0.02	3.98 ± 0.02	6.78 ± 0.20
50 cm	7.09 ± 0.02	11.32 ± 0.02	3.93 ± 0.02	6.44 ± 0.02	4.78 ± 0.24	8.74 ± 0.38

These results were used to make the linear plots in figure 6.11, which together with the equations in section 2.4 were used to calculate values for the effective angle and the effective length of the burst with their respective uncertainties. The results are summarized in table 6.8.

(a) Gravel, coherent signals.
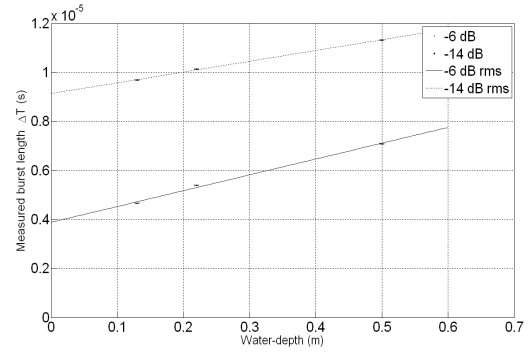
(b) Gravel, averaged envelopes.
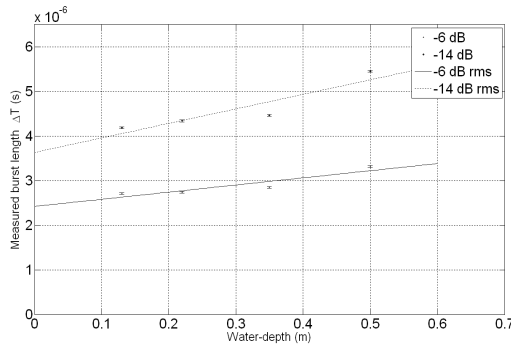
(c) Coarse sand, coherent signals.
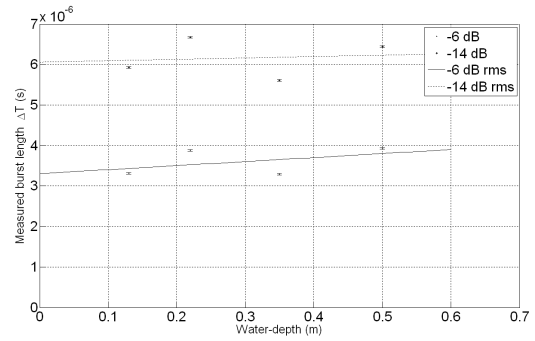
(d) Coarse sand, averaged envelopes.
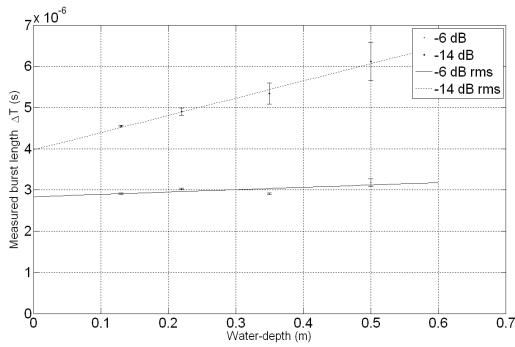
(e) Fine sand, coherent signals.
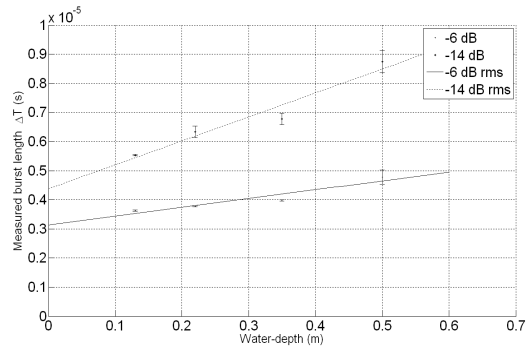
(f) Fine sand, averaged envelopes.

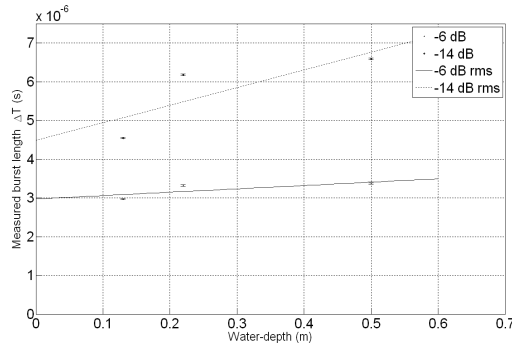Figure 6.11: Linear plots of the effective echo duration as a function of water-depth, 5 MHz transducer.

Table 6.8: Effective angle and effective length of the burst, 5 MHz transducer, averaged signals.

	Gravel surface	Coarse sand surface	Fine sand surface
Coherent stacked signals:			
	-6 dB data	-6 dB data	-6 dB data
α	0.0006 ± 0.0005	0.0012 ± 0.0003	0.0004 ± 0.0003
D	4.5 ± 0.4 mm	3.6 ± 0.2 mm	4.3 ± 0.2 mm
θ	$2.1° \pm 0.9°$	$2.8° \pm 0.4°$	$1.7° \pm 0.6°$
	-14 dB data	-14 dB data	-14 dB data
α	0.0034 ± 0.0024	0.0024 ± 0.0007	0.0031 ± 0.0002
D	6.7 ± 1.6 mm	5.4 ± 0.5 mm	6.0 ± 0.2 mm
θ	$4.7° \pm 1.7°$	$4.0° \pm 0.6°$	$4.5° \pm 0.2°$
Averaged envelopes:			
	-6 dB data	-6 dB data	-6 dB data
α	0.0048 ± 0.0003	0.0007 ± 0.0010	0.0023 ± 0.0005
D	5.8 ± 0.2 mm	5.0 ± 0.7 mm	4.7 ± 0.3 mm
θ	$5.6° \pm 0.2°$	$2.2° \pm 1.5°$	$3.9° \pm 0.4°$
	-14 dB data	-14 dB data	-14 dB data
α	0.0033 ± 0.0001	0.0003 ± 0.0016	0.0062 ± 0.0011
D	13.7 ± 0.2 mm	9.1 ± 1.0 mm	6.6 ± 0.7 mm
θ	$4.6° \pm 0.1°$	$1.3° \pm 4.0°$	$6.4° \pm 0.6°$

For the stacked coherent signals and the averaged envelopes there is almost consistently an increase in echo duration with water-depth. Also the measured echo durations lie closer to the linear graphs than what was seen when considering individual scattered signals. This leads to less uncertainty in the coefficients of the lines, and therefore the different parameters calculated. Considering that the linear plots have different scales on the y-axis, there is a difference in the linear plots found from the coherent signals and the averaged envelopes. The averaged envelopes give echo durations that lie closer to the linear graph for the gravel surface. However, for the coarse and fine sand surfaces, the measured echo durations lie closer to the linear plot when the coherent signal envelopes are considered. The -6 dB data corresponds to the θ_{-3dB} angle, which was read from the directivity plot for the 5 MHz transducer to be $2.50° \pm 0.60°$. The -14 dB data corresponds to the θ_{-7dB} angle, which was read from the directivity plot for the 5 MHz transducer to be $3.60° \pm 0.60°$. The effective burst length, D, should be compared to the length of the transmitted burst, which for the 5 MHz transducer with a 10 cycle burst, is 3 mm plus some more due to ringing in the transducer. Comparison of the measured data with the expected increase in echo duration with water-depth, following the discussion in section 2.4, show that the increase is variable. The theoretical values of the linear increase coefficient α is $\alpha_{-3dB} = 0.00095$ and $\alpha_{-7dB} = 0.0020$ for the -6 dB and the -14 dB data, respectively. For some of the data the increase in echo duration is smaller than what is expected, while for other data the increase is larger than expected.

6.5.4 Results of the stacked signals for the 1.4 MHz transducer

For the 1.4 MHz transducer, the 40 dB pre-amplifier was found to amplify the signal by a factor of 51.6, which is approximately 34 dB. The results of the stacked signals from the coarse sand surface measured with the 1.4 MHz transducer for different water-depths, are plotted in figure 6.12.
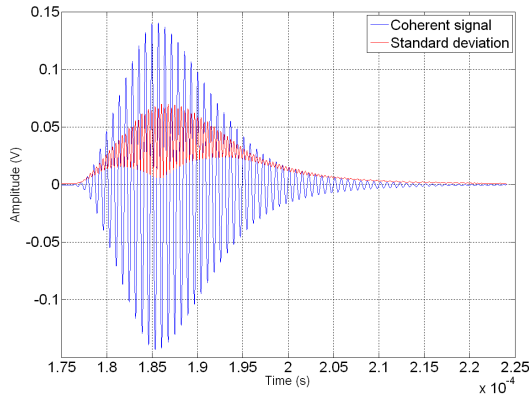
(a) Coherent signal, 13 cm.
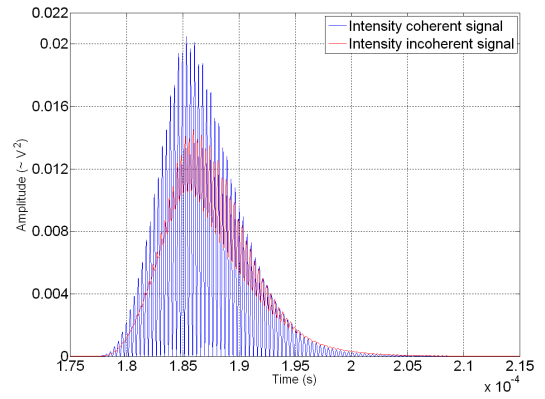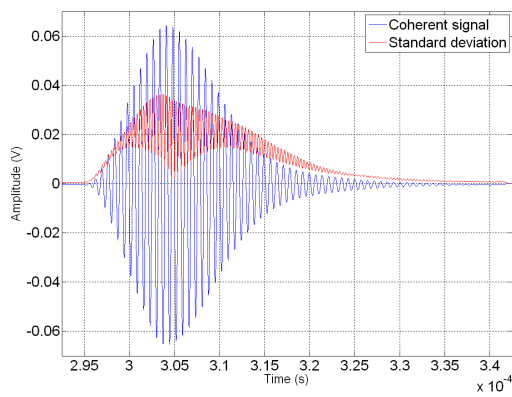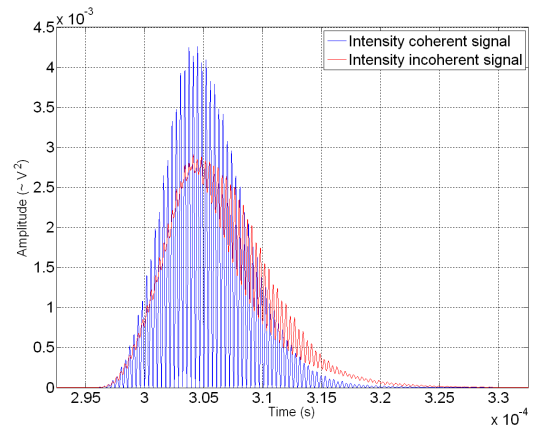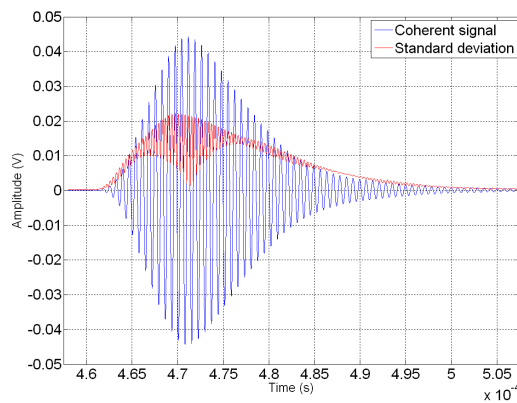
(b) Intensitities, 13 cm.

(c) Coherent signal, 22 cm.

(d) Intensitities, 22 cm.
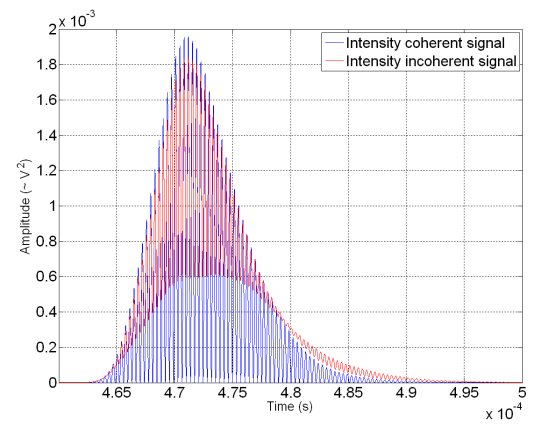
(e) Coherent signal, 35 cm.

(f) Intensitities, 35 cm.
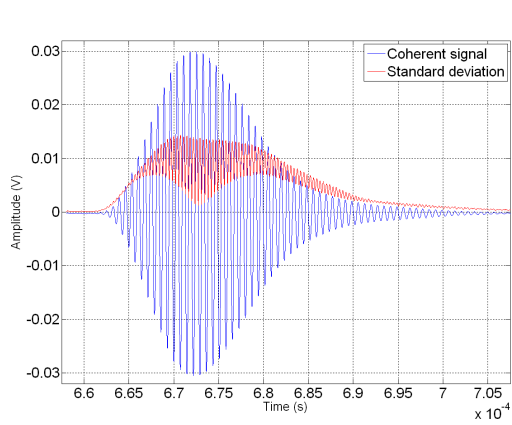
(g) Coherent signal, 50 cm.
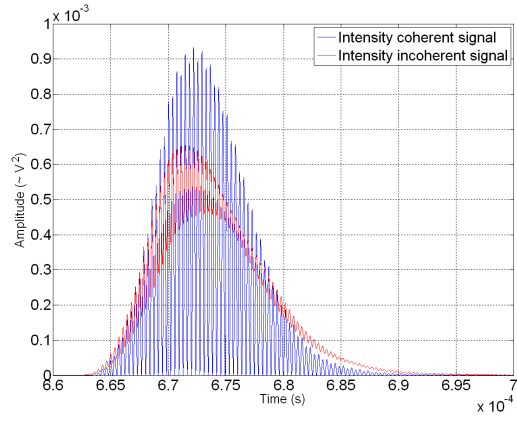
(h) Intensities, 50 cm.

Figure 6.12: Stacked signals from the coarse sand surface, 1.4 MHz transducer.

The results of the stacked signals from the fine sand surface measured with the 1.4 MHz transducer for different water-depths, are plotted in figure 6.13.
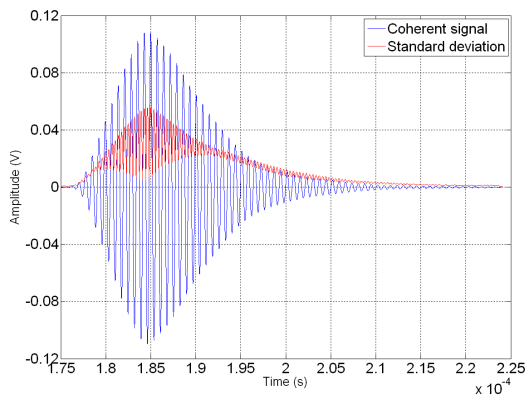
(a) Coherent signal, 13 cm.

(b) Intensities, 13 cm.

(c) Coherent signal, 22 cm.

(d) Intensities, 22 cm.

(e) Coherent signal, 35 cm.
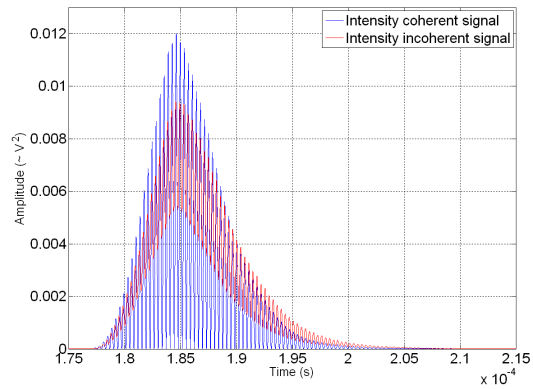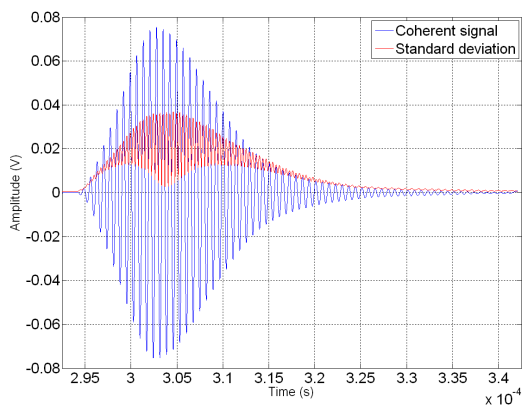
(f) Intensities, 35 cm.

(g) Coherent signal, 50 cm.
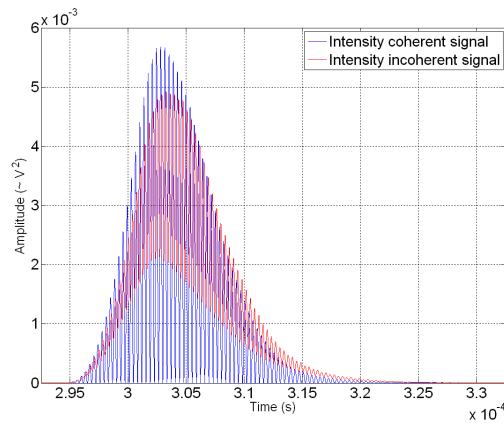
(h) Intensities, 50 cm.
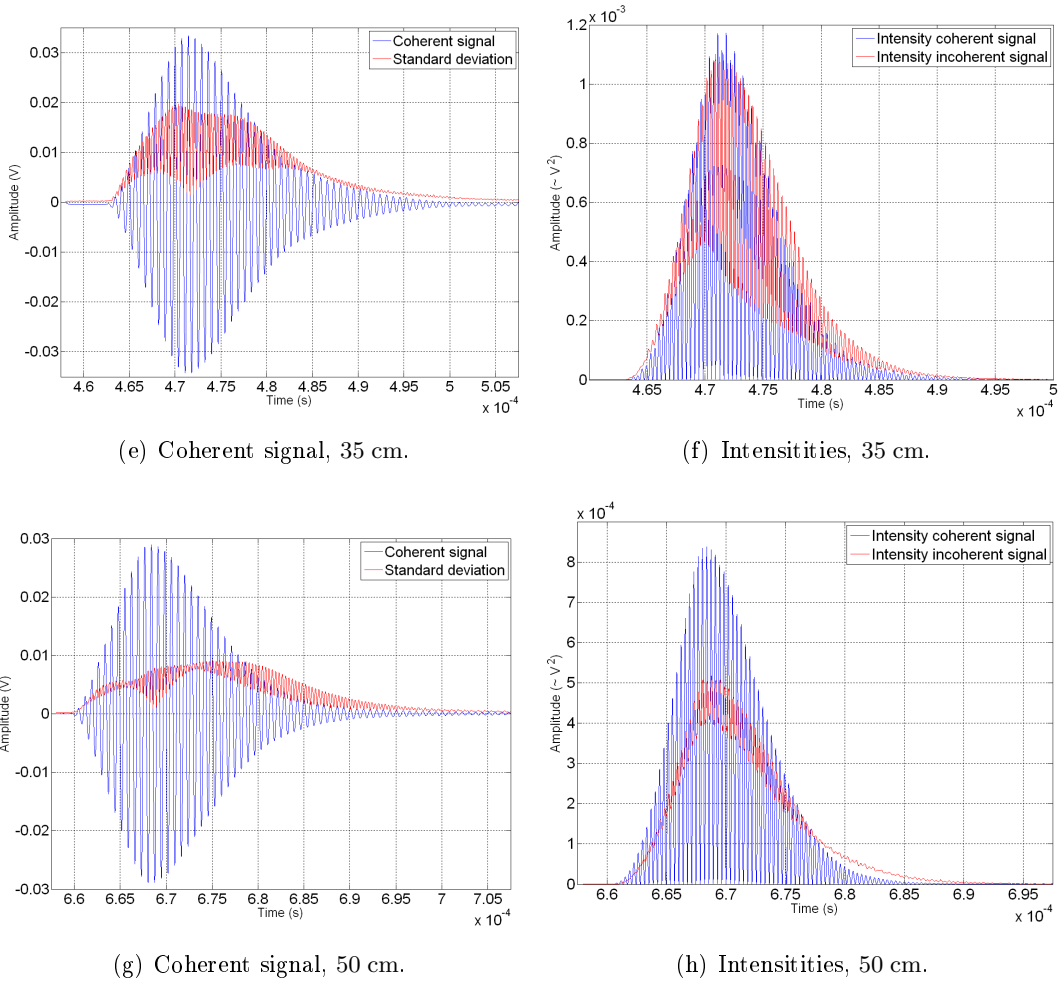
Figure 6.13: Stacked signals from the fine sand surface, 1.4 MHz transducer.

Comparing the amplitudes from the coarse and fine sand surfaces, the amplitudes are greater for the coarse sand surface, except again at the 22 cm water-depth, where the amplitude of the signal from the fine sand surface is larger. It might be an effect of the fine sand surface not being perfectly leveled that comes into play at this water-depth.

Finding the signal envelopes by Hilbert transformation of the coherent signals, as well as averaging the individual signal envelopes without phase-aligning the individual signals, gave the following results for the 1.4 MHz transducer.
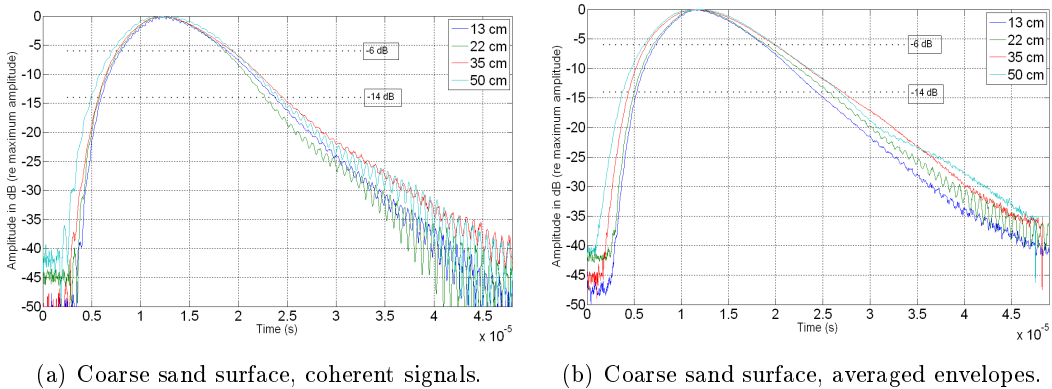
(a) Coarse sand surface, coherent signals.

(b) Coarse sand surface, averaged envelopes.

67

(c) Fine sand surface, coherent signals.   (d) Fine sand surface, averaged envelopes.
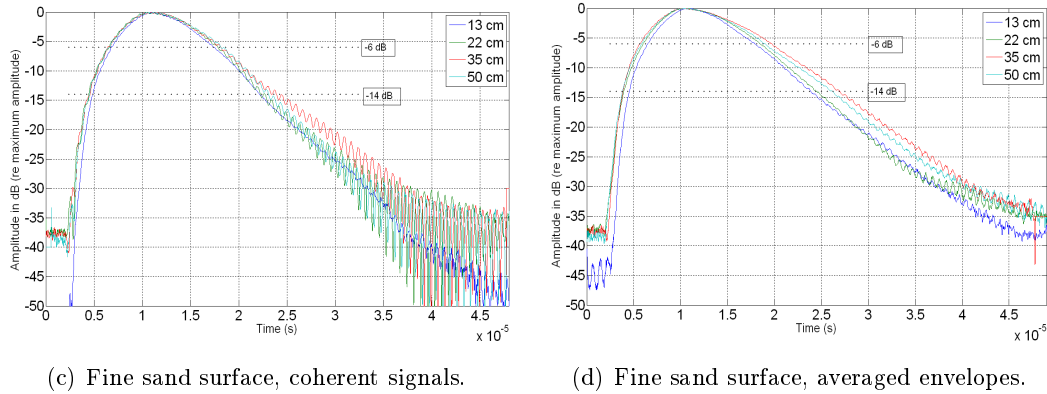
Figure 6.14: Coherent signal envelopes and averaged envelopes, 1.4 MHz.

The values of the effective echo durations, read from figure 6.14 are summarized in table 6.9.

Table 6.9: Effective echo durations, 1.4 MHz transducer.

Water-depth	Coarse sand surface		Fine sand surface	
	-6 dB data	-14 dB data	-6 dB data	-14 dB data
Coherent stacked signals:				
13 cm	10.93 ± 0.08 µs	17.83 ± 0.08 µs	10.67 ± 0.08 µs	17.26 ± 0.08 µs
22 cm	10.75 ± 0.08 µs	16.92 ± 0.08 µs	11.28 ± 0.10 µs	18.04 ± 0.30 µs
35 cm	11.76 ± 0.08 µs	18.92 ± 0.08 µs	11.75 ± 0.08 µs	19.06 ± 0.60 µs
50 cm	12.51 ± 0.08 µs	19.15 ± 0.08 µs	11.53 ± 0.12 µs	18.56 ± 0.08 µs
Averaged envelopes:				
13 cm	11.53 ± 0.08 µs	19.05 ± 0.08 µs	11.46 ± 0.08 µs	19.30 ± 0.08 µs
22 cm	11.99 ± 0.08 µs	20.38 ± 0.25 µs	12.50 ± 0.08 µs	20.59 ± 0.08 µs
35 cm	13.58 ± 0.08 µs	22.66 ± 0.20 µs	14.06 ± 0.10 µs	23.00 ± 0.20 µs
50 cm	13.96 ± 0.08 µs	23.04 ± 0.20 µs	13.13 ± 0.14 µs	22.28 ± 0.20 µs

These results were used to make the linear plots in figure 6.15, which together with the equations in section 2.4 were used to calculate values for the effective angle and the effective length of the burst with their respective uncertainties. The results are summarized in table 6.10.

(a) Coarse sand surface, coherent signals.   (b) Coarse sand surface, averaged envelopes.

68

(c) Fine sand surface, coherent signals.   (d) Fine sand surface, averaged envelopes.
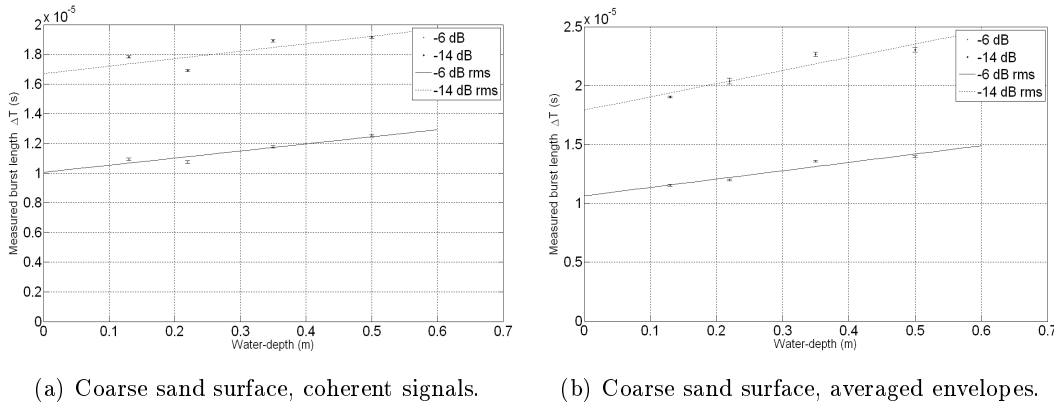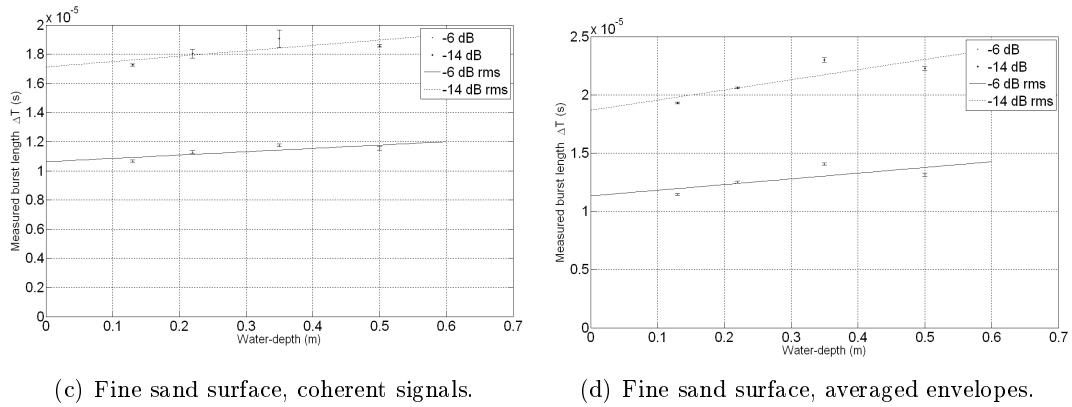
Figure 6.15: Linear plots of the effective echo duration as a function of water-depth, 1.4 MHz transducer.

Table 6.10: Effective angle and effective length of the burst, 1.4 MHz transducer, averaged signals.

	Coarse sand surface		Fine sand surface	
	-6 dB data	-14 dB data	-6 dB data	-14 dB data
Coherent stacked signals:				
α	0.0036 ± 0.008	0.0038 ± 0.0021	0.0017 ± 0.0009	0.0028 ± 0.0016
D	15.1 ± 0.6 mm	25.0 ± 1.4 mm	15.9 ± 0.7 mm	25.7 ± 1.1 mm
θ	$4.8° \pm 0.6°$	$5.0° \pm 1.4°$	$3.3° \pm 0.9°$	$4.3° \pm 1.2°$
Averaged envelopes:				
α	0.0053 ± 0.0011	0.0084 ± 0.0019	0.0037 ± 0.0025	0.0065 ± 0.0030
D	16.0 ± 0.7 mm	26.9 ± 1.3 mm	17.0 ± 1.7 mm	28.0 ± 2.0 mm
θ	$5.9° \pm 0.6°$	$7.4° \pm 0.8°$	$4.9° \pm 1.7°$	$6.5° \pm 1.5°$

For the stacked coherent signals and the averaged envelopes, there is almost consistently an increase in echo duration with water-depth, as was also the case for the 5 MHz transducer. Also the measured echo durations lie closer to the linear graphs than what was seen when considering individual scattered signals for the 1.4 MHz transducer. This leads to less uncertainty in the coefficients of the linear graphs, and therefore the different values calculated. Considering that the linear plots have different scales on the y-axis, there is a difference in the linear plots found from the coherent signals and the averaged envelopes. The -6 dB data corresponds to the θ_{-3dB} angle, which was read from the directivity plot for the 1.4 MHz transducer to be $4.60° \pm 0.40°$. The -14 dB data corresponds to the θ_{-7dB} angle, which was read from the directivity plot for the 1.4 MHz transducer to be $7.00° \pm 0.40°$. The effective burst length, D, should be compared to the length of the signal, which for the 1.4 MHz transducer with a 10 cycle burst is 10.7 mm. Comparison of the measured data with the expected increase in echo duration with water-depth, following the discussion in section 2.4, show that the increase is variable. For some of the data the increase in echo duration is smaller than what is expected, while for other data the increase is larger than expected.

6.6 Depth-dependence correction

One objective was to look at how the depth-dependence of the echoes could be compensated for. Signals from the fine and coarse sand surfaces were measured using different lengths of the transmitted signal, and two of the correction steps suggested by Pouliquen [8], discussed in section 2.4.1, were applied to compare echo envelopes from the same sediment at different water-depths. This was done looking at averaged echo envelopes without phase alignment. The first correction step is to adjust the length of the transmitted burst linearly with water-depth, a longer burst should be used for greater depths. The second step brings the measured signal to a reference water-depth.
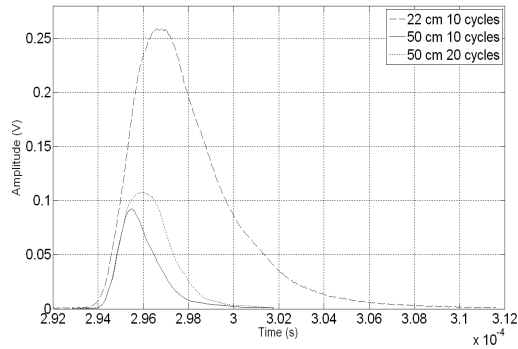
(a) Echo envelope at 50 cm moved to a reference distance at 22 cm, coarse sand.
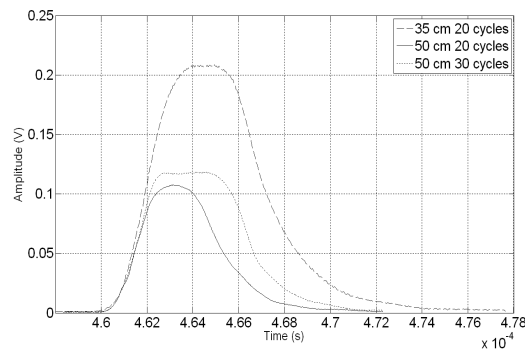
(b) Echo envelope at 50 cm moved to a reference distance at 35 cm, coarse sand.
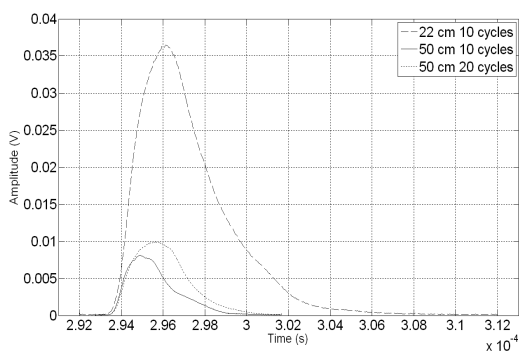
(c) Echo envelope at 50 cm moved to a reference distance at 22 cm, fine sand.
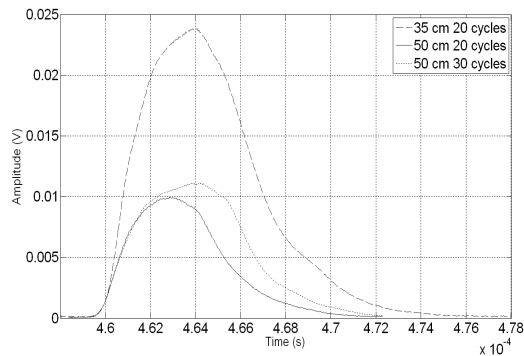
(d) Echo envelope at 50 cm moved to a reference distance at 35 cm, fine sand.

Figure 6.16: Application of correction steps, moving the measured signals to a reference water-depth. 5 MHz transducer.

First of all it should be noted that a power or intensity adjustment is also necessary to make the echoes depth independent. However, this is not trivial and was not looked into in this work. This makes it difficult to compare the signals. However, there might be an indication that adjusting the transmitted burst length is a useful step in making the echo envelope depth independent. The measurements were not well enough planned to give the right transmitted burst lengths relative to the water-depths measured, hence the relationship $\tau_0 = \tau H/r$ (see section 2.4.1) was not exact. The measurements at 50 cm moved to a reference depth of 22 cm should have been measured with a transmitted burst consisting of approximately 23 cycles, while the measurements at 50 cm moved to a reference depth of 35 cm should have been measured with a transmitted burst consisting of approximately 29 cycles.

70

6.7 Adjusting the signals measured with the 1.4 MHz transducer

As already mentioned, the measurements done with the 1.4 MHz transducer used an experimental setup where the high-pass cutoff frequency mistakenly was set to 2 MHz. This leads to a strong attenuation of the frequencies around the transmitted frequency and the frequencies below, which strongly influence the echo signal shape and energy. The mistake was discovered too late to rerun the experiment with the right experimental setup. It was therefore decided to make an attempt to adjust the measurements, by removing the effect of the pre-amplifier and the filter on the already measured signals. To do this the frequency response of these instruments connected in series had to be found. The frequency response was first measured by applying a burst consisting of one period of a square wave with a frequency of 1.34 MHz from the signal generator. Both the input and output signals were measured by the oscilloscope, and were then Fourier transformed so that the frequency response could be found. Using this method, the phase of the frequency response is included. A more accurate way of determining the frequency response is measuring the input and output signals, while stepping through a range of frequencies. This was done for frequencies between 0.5 MHz and 6.1 MHz, with steps of 0.2 MHz. By using the steady-state area of the measured signals, the rms-amplitude can be calculated and the magnitude of the frequency response can be found by dividing the amplitude of the signal out by the amplitude of the signal in. Phase information is not included. When comparing the results obtained by the two methods, the magnitude of the frequency response start to increase from zero at approximately the same frequency. However, the curve found by the first method rises much steeper than the curve found by the second method, and starts to fall off again at around 2 MHz, while the curve found by the second method falls off at around 4 MHz, referring to figure 6.17. Hence, it was decided to use the latter method, as this was believed to be more accurate.

The frequency response for frequencies up to 3 MHz was used, as this included most of the high-frequency components in the measured signal. The measured frequency response was fitted with a cubic polynomial, to give a better resolution of the frequencies. This needed to be done so that the frequency response had the same resolution of frequencies as the frequency spectrum of the measured signal. The measured frequency response and the fitted polynomial is shown in figure 6.17. The frequency response for frequencies below 0.5 MHz was set to a constant value, equal to the value measured at 0.5 MHz.
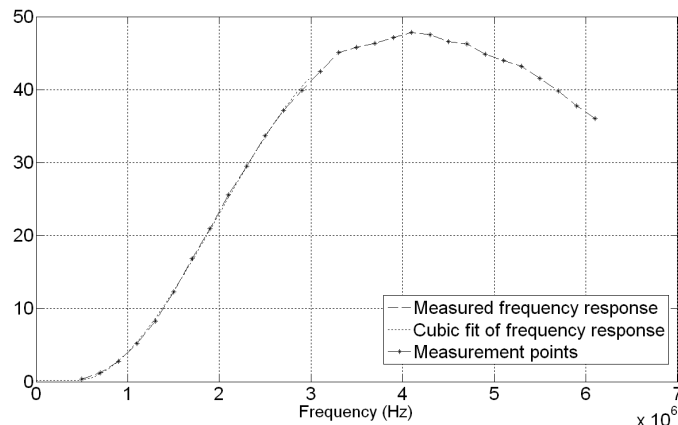
Figure 6.17: Frequency response of the pre-amplifier and the filter, measured data and fitted polynomial.

The wanted signal, is the signal from the transducer before it goes through the pre-amplifier and the filter. The measured signal is the signal from the receiver convolved with the impulse response of the pre-amplifier in series with the filter. Fourier transformation therefore gives

$$FT(\text{measured signal}) = FT(\text{wanted signal})FT(h), \tag{6.1}$$

where FT is the Fourier transform, h is the impulse response and $FT(h)$ therefore the frequency response measured. To find the wanted signal, the frequency spectrum of the measured signal must be divided by the frequency response. The frequency spectrum of the measured signal was found, frequency components above 3 MHz as well as the DC-component were set to zero. This gave the result shown in figure 6.18(b). By setting the low frequency components of the signal to zero, the result in figure 6.18(c) was achieved.
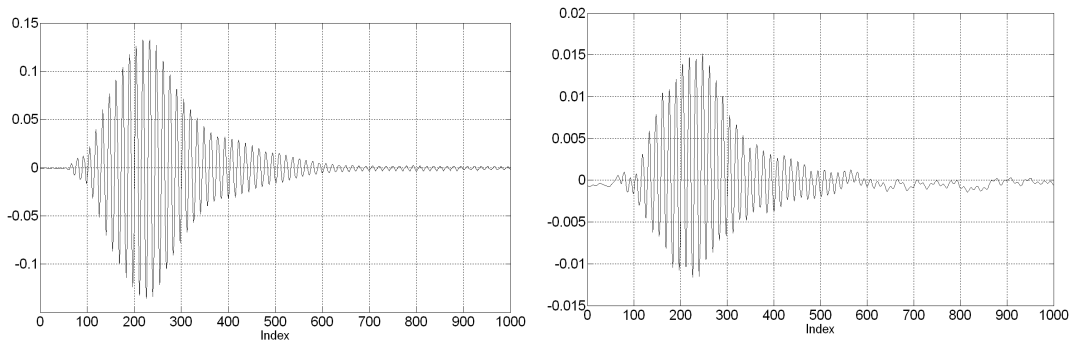
(a) Measured signal with the 1.4 MHz transducer.   (b) Adjusted signal, DC-component set to zero.
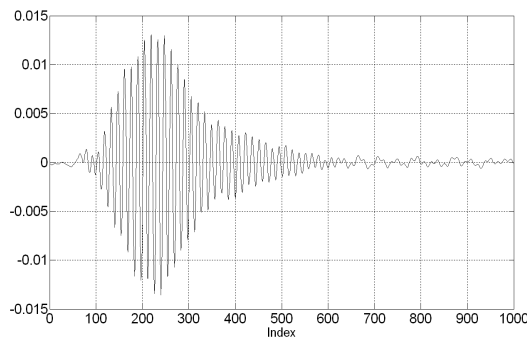
(c) Adjusted signal, DC-component and low frequency components set to zero.

Figure 6.18: Measured and adjusted signals.

The results show that the low frequency components are strongly amplified as expected, but this will exaggerate low frequency noise as well, which is not desirable. These frequency components influence the shape of the echoes, which are used to calculate the different classification parameters. The signal amplitude has decreased compared to the measured signal, since the effect of the pre-amplifier is removed. It was not trusted that this method gives a satisfactory result for the adjusted signals, and it was decided not to go any further with these results. However, the measured signals obtained with this transducer are retained. Since all of the measurements are taken with the same experimental setup, the difference in the signals should be due to differences of the scattering surface, hence the measurements can still be compared.

Chapter 7

Measurements on clay

After measuring the returned echo from a copper reflector and a sand surface, the next step was to measure on a different type of sediment, hence air drying clay was bought.

7.1   Preparation of the clay and measurement setup

The clay came in a big lump, and needed to be worked with in order to soften it up before placing it in the tray. The clay was packed carefully into the tray, trying to get as little air pockets as possible in the clay sediment. As with the sand surface, the challenge was once again to get a levelled surface. This was achieved by dragging a metal plate across the surface. However, as with the sand tray, the surface was disturbed when placed in the water tank as patches of clay came off and were disposed of on other parts of the surface. Again, it proved difficult to level the surface while it was in the water tank, and the only solution was to take it out of the water tank to relevel it. The clay seemed to contain more water in the top layer after being left in the tank for a few days, and the sediment seemed more inhomogenous as some of the clay conglomerated, making relevelling more difficult. Plastic foil was wrapped over the surface before placing it in the water tank, in an attempt to keep the surface undisturbed. However, the clay stuck to the foil when it was taken off, so this technique proved useless. It seemed that the only possibility was to just place the tray as carefully as possible into the water tank, minimizing the disturbance of the surface.
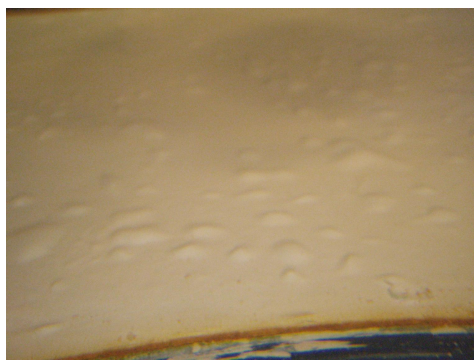
Figure 7.1: Clay surface with pockets.

As the clay was left in the water tank for a few days, another problem arose. Small pockets formed on the surface. It was first believed to be air pockets, however, as the pockets were punctured, no air bubbles rose to the surface. It might have been a result of the clay expanding. It was decided to relevel the surface before each day of measurements, to avoid the problem

of surface pockets, as they gave very large signal variation across the surface, illustrated in figure 7.2. A series of measurements were made at different water-depths from $13 - 22$ cm. As for the early sand measurements, no pre-amplifier was used, nor was the branching box used. Hence, greater distances were difficult to measure, due to poor resolution.
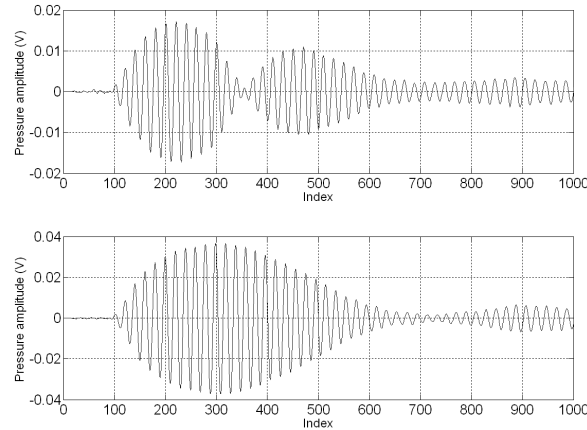
Figure 7.2: Signal variation across the clay surface.

7.2 Results and discussion of the measurements on clay

The first set of measurements was taken before the problem with pockets on the surface arose, hence only one area of the surface was insonified for each water-depth. Signal variation across the surface was not considered at this point of time. The signal envelopes for the backscattered signals from the clay surface at different water-depths, and the corresponding linear plot of the effective echo duration as a function of water-depth, are shown in figure 7.3.
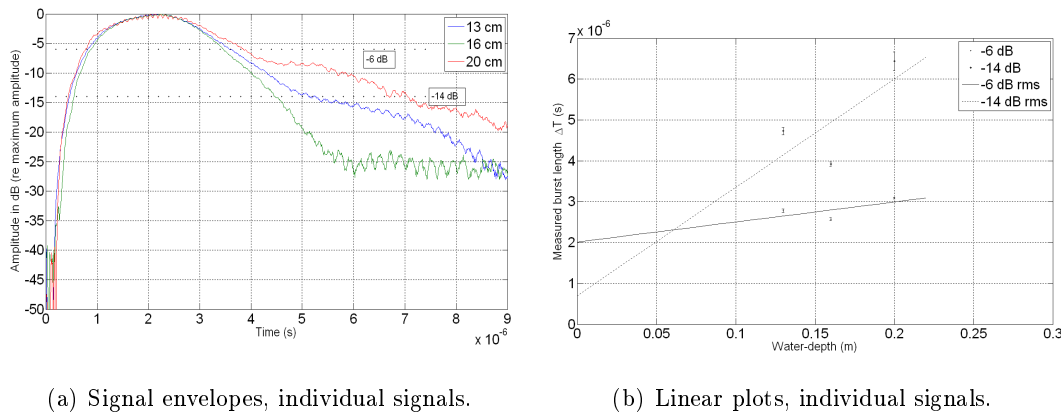
(a) Signal envelopes, individual signals.

(b) Linear plots, individual signals.

Figure 7.3: Scattering from the clay surface at different water-depths, individual signals, April 2009.

For the next set of measurements, it was decided to use the method of stacking signals, as it was difficult to level the surface. Also, the Hilbert transform of individual signals taken in the same position for the different water-depths were looked at, to compare to the earlier measurements. These results are plotted in figure 7.4.

(a) Signal envelopes, individual signals.

(b) Linear plots, individual signals.
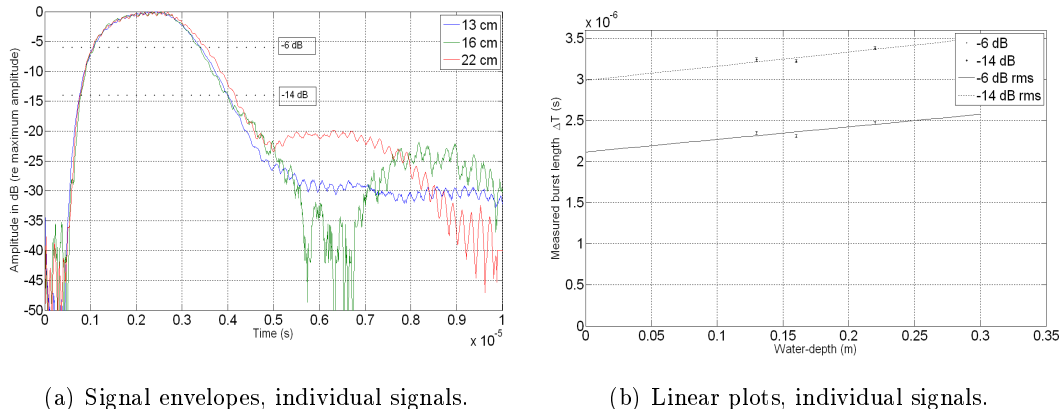
Figure 7.4: Scattering from the clay surface, individual signals, May 2009.

The values of the effective echo durations, read from figures 7.3(a) and 7.4(a) are summarized in table 7.1.

Table 7.1: Effective echo durations, individual signals.

	April 2009		May 2009	
Water-depth	-6 dB data	-14 dB data	-6 dB data	-14 dB data
13 cm	2.78 ± 0.04 µs	4.73 ± 0.09 µs	2.35 ± 0.02 µs	3.24 ± 0.02 µs
16 cm	2.57 ± 0.04 µs	3.92 ± 0.05 µs	2.31 ± 0.02 µs	3.22 ± 0.02 µs
20/22 cm	3.09 ± 0.02 µs	6.44 ± 0.22 µs	2.47 ± 0.02 µs	3.38 ± 0.02 µs

These results were used to make the linear plots in figures 7.3(b) and 7.4(b), which together with the equations in section 2.4 were used to calculate values for the effective angle and the effective burst length with their respective uncertainties. The results are summarized in table 7.2.

Table 7.2: Effective angle and effective burst length, individual signals.

	April 2009		May 2009	
	-6 dB data	-14 dB data	-6 dB data	-14 dB data
α	0.0037 ± 0.0042	0.020 ± 0.019	0.0011 ± 0.0007	0.0013 ± 0.0006
D	3.0 ± 1.4 mm	1.0 ± 6.3 mm	3.2 ± 0.3 mm	4.5 ± 0.2 mm
θ	$4.9° \pm 2.8°$	$11.4° \pm 5.3°$	$2.7° \pm 0.9°$	$2.9° \pm 0.7°$

The results of the measurements done in April are considerably different than the results of the measurements done in May. Especially for the -14 dB data, where the uncertainties in the April measurements are very large. The -6 dB data corresponds to the θ_{-3dB} angle, which was read from the directivity plot for the 5 MHz transducer to be $2.50° \pm 0.60°$. The measurements done in May give a value close to this. The -14 dB data corresponds to the θ_{-7dB} angle, which was read from the directivity plot for the 5 MHz transducer to be $3.60° \pm 0.60°$. The effective burst length, D, should be compared to the length of the signal, which for the 5 MHz transducer with a 10 cycle burst, is 3 mm plus some more due to ringing in the transducer. The measurements done in May give values closer to the theoretic values, and have less uncertainties. The effective angle, θ, for the -14 dB data is larger compared to the -6 dB data, but does not increase by as much as is predicted following the discussion in section 2.4.

75

7.2.1 Results of the stacked signals

The echo signals were phase-aligned by their bottom pick, as described in section 4.5. The coherent signals at different water-depths and the standard deviation of the individual signals from the coherent signal, are plotted in figure 7.5. The intensities of the coherent signals and the incoherent signals are found by the method discussed in section 4.6.
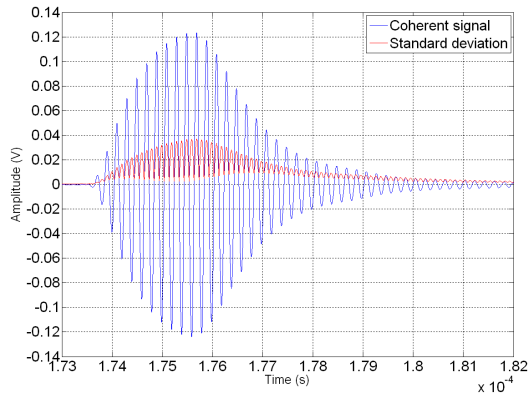
(a) Coherent signal, 13 cm.
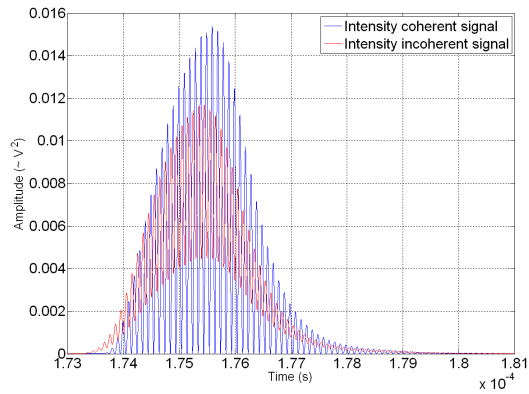
(b) Intensitities, 13 cm.
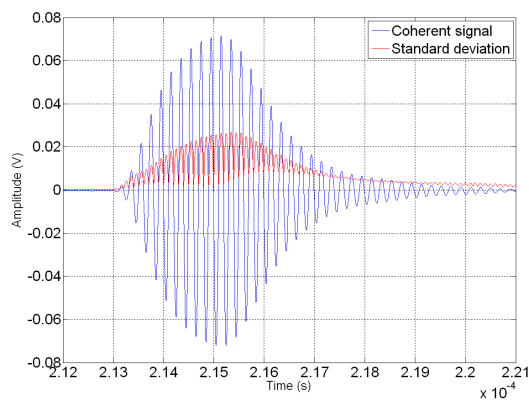
(c) Coherent signal, 16 cm.
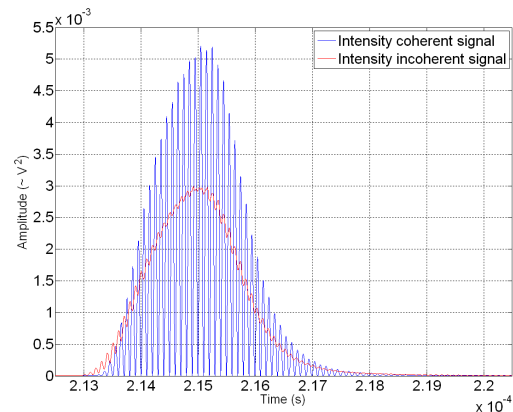
(d) Intensitities, 16 cm.
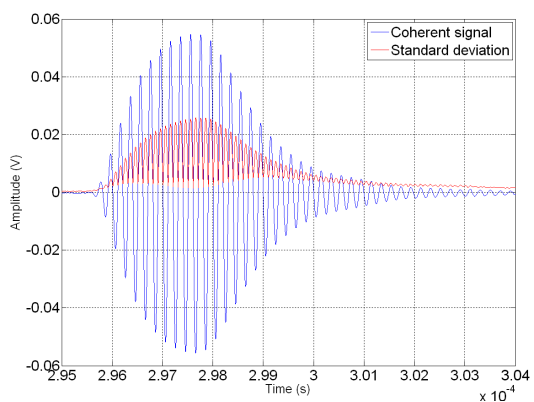
(e) Coherent signal, 22 cm.
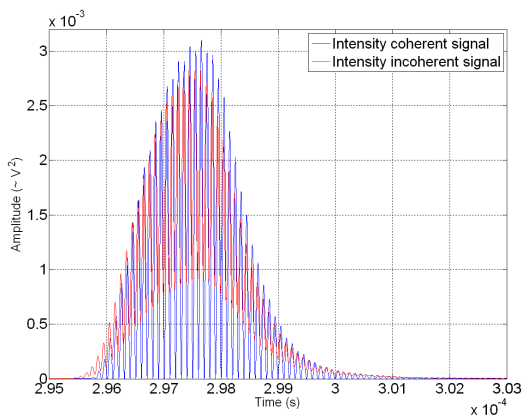
(f) Intensitities, 22 cm.

Figure 7.5: Stacked signals from the clay surface, 5 MHz transducer.

76

The Hilbert transform was used to find the signal envelope of the stacked coherent signals, as well as the averaged signal envelopes that are not phase-aligned.

(a) Coherent signals.

(b) Coherent signals.

(c) Averaged envelopes.

(d) Averaged envelopes.
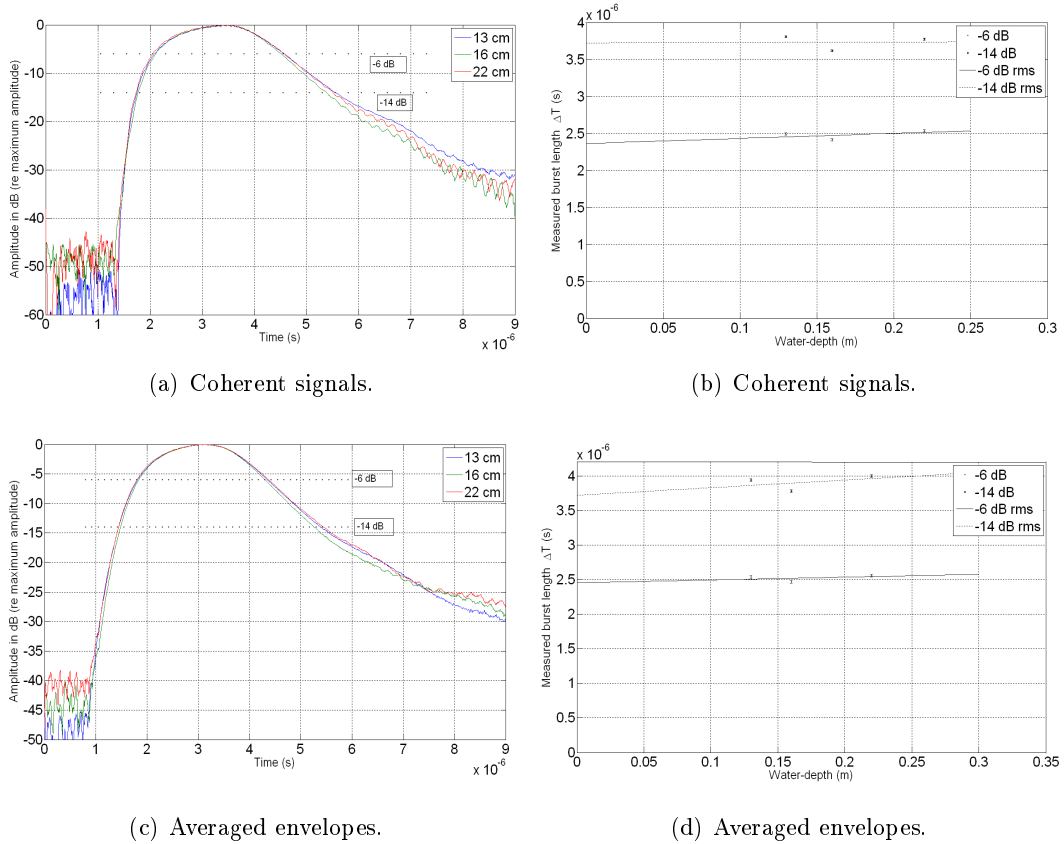
Figure 7.6: Signal envelopes and linear plots of the echo duration as a function of water-depth for averaged signals from the clay surface.

The values of the effective echo durations read from figures 7.6(a) and 7.6(c) are summarized in table 7.3.

Table 7.3: Effective echo durations, averaged signals, clay surface.

Water-depth	-6 dB data	-14 dB data
Coherent stacked signals:		
13 cm	2.49 ± 0.02 µs	3.81 ± 0.02 µs
16 cm	2.42 ± 0.02 µs	3.62 ± 0.02 µs
22 cm	2.54 ± 0.02 µs	3.78 ± 0.02 µs
Averaged envelopes:		
13 cm	2.54 ± 0.02 µs	3.94 ± 0.02 µs
16 cm	2.47 ± 0.02 µs	3.78 ± 0.02 µs
22 cm	2.56 ± 0.02 µs	4.00 ± 0.02 µs

These results were used to make the linear plots in figures 7.6(b) and 7.6(d), which together with the equations in section 2.4 were used to calculate values for the effective angle and the effective burst length with their respective uncertainties. The results can be found in table 7.4.

Table 7.4: Effective angle and effective burst length, averaged signals.

	-6 dB data	-14 dB data
Coherent stacked signals:		
α	0.0005 ± 0.0008	0.00007 ± 0.00170
D	3.5 ± 0.3 mm	5.6 ± 0.6 mm
θ	$1.9° \pm 1.4°$	$0.7° \pm 8.0°$
Averaged envelopes:		
α	0.0003 ± 0.0007	0.0008 ± 0.0017
D	3.7 ± 0.3 mm	5.6 ± 0.6 mm
θ	$1.4° \pm 1.6°$	$2.3° \pm 2.4°$

Compared to the results for the individual signal envelopes, these data indicate a smaller increase of the echo duration as a function of depth. Also, compared to the results of the averaged signals from the different sand surfaces, the increase in echo duration is smaller here. The discussion in section 2.4 was based on surface scattering. For the clay surface however, it is likely that more of the beam is transmitted into the sediment, and therefore that other effects concerning sediment volume scattering influence the signal scattered back to the transducer. The uncertainties in the data listed in table 7.4 are large, especially for the effective angle found from the coherent -14 dB data. The angle θ_{-3dB} read from the directivity plot in section 4.3.1 is $2.5 \pm 0.6°$. Within the uncertainty bounds, the effective angle found from the -6 dB level data correlates to this value. The angle θ_{-7dB} read from the directivity plot is $3.6 \pm 0.6°$. The effective angle, calculated from the averaged envelope -14 dB data, correlates to this value within the uncertainty bounds. The effective angle found from the coherent -14 dB data, however, is much lower than this. But as already mentioned, the uncertainty is large here.

Chapter 8

Parameters used for seabed classification and characterization

In this chapter, different echo parameters based on energy statistics and spectral moments will be considered and calculated for the measured data collected from different bottom types. The goal is to find out whether any of these parameters are good discriminators of sediments at the frequencies used in this work.

8.1 Energy and shape parameters

As mentioned in the introduction, van Walree *et al.* [5] compare echo shape parameters of field data with the ground truth. The parameters used in their work were tested on the data collected in this master thesis, along with another set of parameters given for a statistical distribution.

8.1.1 Expressions for the energy and shape parameters

In van Walree *et al.* [5] the total energy of an echo is defined as

$$E = \int_0^{T_0} I(t)\, \mathrm{d}t, \tag{8.1}$$

where $I(t)$ is the echo intensity, which varies quadratically with the recorded voltage. The integral runs over a selected time window of the echo envelope, T_0, which is set to 10 ms, centered at the peak echo intensity. Further, they define the echo center of gravity as

$$t_0 = \frac{1}{E} \int_0^{T_0} I(t)t\, \mathrm{d}t. \tag{8.2}$$

These two parameters are used in the calculation of the echo shape parameters, namely the timespread, T, and the skewness, $S1$, given by

$$T = \sqrt{\frac{4}{E} \int_0^{T_0} I(t)(t - t_0)^2\, \mathrm{d}t}, \tag{8.3}$$

$$S1 = \frac{8}{T^3 E} \int_0^{T_0} I(t)(t - t_0)^3\, \mathrm{d}t. \tag{8.4}$$

These definitions are said to resemble the moments associated with statistical distributions. The timespread is a measure of the temporal extent of the echo, while the skewness is a measure of the echo assymetry. Since these parameters are both normalized by the echo energy, E, they should be independent of the echo energy and hence be considered as pure shape parameters. The skewness, $S1$, is also normalized by the third power of T to make the skewness independent of the echo duration. The skewness of seafloor echoes are typically positive, since they usually consist of an initial peak of specular reflection and a tail consisting of seafloor surface scattering and volume scattering.

In a textbook on statistics [25], a different definition for skewness was found, given by

$$S2 = \text{skewness} = \frac{\sum_{i=1}^{N}(Y_i - \overline{Y})^3}{(N-1)s^3}, \tag{8.5}$$

where $\overline{Y}$ is the mean value of the samples, s is the standard deviation and N is the number of samples. When the distribution is symmetric, the skewness should approach a value of zero. This should give about the same result as the value for skewness calculated by equation (8.4), as they are both based on statistical distribution. However, in this work both were calculated for comparison. A higher moment, also associated with the statistical distribution, is the kurtosis, which describes the peakedness of the distribution. It is given by the same equation as the skewness, except that a power 3 is replaced by a power 4

$$K = \text{kurtosis} = \frac{\sum_{i=1}^{N}(Y_i - \overline{Y})^4}{(N-1)s^4}. \tag{8.6}$$

8.1.2 Results of calculating the parameters for the measured data from different sediments

The parameters mentioned above was calculated for the different data using a MATLAB script. Both the coherent intensity plots and the incoherent intensity plots from chapters 6 and 7 were looked at. It was the later measurements on sand that were considered here. Envelopes of the intensities of the incoherent and coherent signals were found, following the discussion in section 4.6, which could then be used for calculation of the different parameters. As the duration of the echoes from for example the clay surface are very different compared to the echo durations of the echoes from the fine sand surface, it was decided to use only the portion of the signal which was over a certain threshold compared to the maximal value of the envelope. 0.5% of the maximum value was chosen, as it was seen that this threshold level included a large portion of the tail of the echo envelopes. Using a set time interval, as discussed by van Walree *et al.* [5], would result in a large portion of the envelope at zero intensity. Hence, the threshold approach was considered an appropriate solution.

For the 1.4 MHz transducer, the calculated parameters for the coherent and incoherent intensities for the fine and coarse sand surfaces are summarized in table 8.1. The intensity envelopes have not been adjusted for spherical spreading, and therefore a comparison is based only on echoes received at the same water-depth.

Table 8.1: Echo energy and shape parameters for the 1.4 MHz transducer.

Water-depth	Surface	Timespread T [μs]	Skewness $S1$	$S2$	Kurtosis K	Total energy TE
Coherent intensity:						
13 cm	Fine sand	7.15	0.73	0.77	2.12	9.25×10^{-7}
	Coarse sand	7.27	0.67	0.72	2.06	1.63×10^{-7}
22 cm	Fine sand	7.35	0.65	0.69	1.96	4.86×10^{-8}
	Coarse sand	6.88	0.55	0.66	1.93	3.46×10^{-8}
35 cm	Fine sand	8.00	0.89	0.85	2.23	1.01×10^{-8}
	Coarse sand	7.80	0.76	0.77	2.12	1.72×10^{-8}
50 cm	Fine sand	7.59	0.64	0.66	1.95	7.45×10^{-9}
	Coarse sand	7.77	0.57	0.62	1.82	8.77×10^{-9}
Incoherent intensity:						
13 cm	Fine sand	8.14	0.96	0.90	2.39	1.22×10^{-7}
	Coarse sand	7.97	0.77	0.76	2.12	2.14×10^{-7}
22 cm	Fine sand	8.31	0.79	0.74	2.04	6.52×10^{-8}
	Coarse sand	8.55	0.83	0.78	2.15	5.15×10^{-8}
35 cm	Fine sand	9.49	0.90	0.76	2.10	1.55×10^{-8}
	Coarse sand	9.34	0.88	0.78	2.14	2.47×10^{-8}
50 cm	Fine sand	9.50	0.92	0.80	2.17	9.29×10^{-9}
	Coarse sand	9.47	0.74	0.69	1.92	1.23×10^{-8}
Uncertainty estimate, Δ:						
13 cm	Fine sand	0.3	0.1	0.1	0.2	2×10^{-8}
	Coarse sand	0.8	0.2	0.1	0.2	2×10^{-7}

From table 8.1 it looks like skewness and kurtosis are echo shape parameters that are consistently larger for the fine sand surface than for the coarse sand surface, when considering the coherent intensity. The timespread seem to vary a bit more, and the result is not consistent for different water-depths. Looking at the incoherent intensity, these parameters do not seem to be useful in discriminating between sand of different grain size, as the results vary between water-depths. The total energy backscattered is not consistently larger for one of the surfaces, it varies between water-depths for both the coherent and the incoherent intensities. From these data, the coherent intensity seem to be more useful than the incoherent intensity for classification using echo shape parameters. The uncertainties are large compared to the difference in the parameters between the two surfaces.

The uncertainty was estimated by calculating the parameters for the average of five individual measurements at a time. With a total of twenty individual measurements, this led to a total of four values for each parameter. The standard deviation of these values were then used as an estimate for the uncertainty in the different parameters. This was done at only one water-depth, as one just wanted an idea about the magnitude of the uncertainty. Also, the uncertainty for the coherent and incoherent intensities were seen to be approximately the same, and it is the uncertainties calculated from the coherent intensities that are given in tables 8.1 and 8.2. To calculate the uncertainty more exact, one should probably have obtained twenty individual measurements, three or four times from the same surface, and used the standard deviation of these measurements.

For the 5 MHz transducer, there were more measured data to compare, as this transducer was used to measure on the gravel and clay surfaces and the copper reflector, in addition to the fine and coarse sand surfaces. However, for the clay surface, only water-depths up to

22 cm were measured. In addition, the measurements were done using different experimental setups. The clay measurements were taken without the pre-amplifier and the branching box. It is therefore questionable whether these data should be compared like this. For the other sediments as well, different pre-amplification was used as discussed in earlier chapters. However, this should only affect the total enegy of the echoes, and not the shape parameters. The calculated echo energy and shape parameters for the different surfaces, considering the coherent intensities, are summarized in table 8.2. The total energy was also calculated, first using the measured data as they were. Then a second set of values were estimated, to allow comparison of the data taken with different measurement setups. This was done by adjusting the data so that it represented measurements taken using the branching box and the 60 dB pre-amplifier. The measured signals were multiplied by factors found by comparing the rms-amplitude of measurements on the same surface, using the different experimental setups. The adjusted energy is not precise, it is just meant as an indication to allow comparison of the total energy backscattered from the different surfaces.

Table 8.2: Echo energy and shape parameters for the 5 MHz transducer, coherent intensity.

Water-depth	Surface	Timespread T [μs]	Skewness $S1$	$S2$	Kurtosis K	Total energy TE	Adjusted TE'
13 cm	Clay	1.59	0.66	0.66	1.86	2.96×10^{-8}	1.27×10^{-5}
	Fine sand	1.89	0.77	0.81	2.15	9.88×10^{-9}	5.38×10^{-7}
	Coarse sand	1.83	0.91	0.89	2.21	7.15×10^{-7}	-
	Gravel	2.17	0.81	1.39	3.44	5.39×10^{-7}	-
22 cm	Clay	1.57	0.58	0.59	1.76	6.23×10^{-9}	2.67×10^{-6}
	Fine sand	2.01	0.79	0.71	1.96	3.03×10^{-9}	1.65×10^{-7}
	Coarse sand	1.88	1.00	0.86	2.14	1.44×10^{-7}	-
	Gravel	2.58	0.92	1.11	2.74	1.10×10^{-7}	-
35 cm	Fine sand	2.25	1.17	0.99	2.44	9.14×10^{-10}	4.98×10^{-8}
	Coarse sand	1.87	0.72	0.88	2.21	8.28×10^{-8}	-
50 cm	Fine sand	2.65	1.31	1.10	2.78	1.63×10^{-10}	8.90×10^{-9}
	Coarse sand	2.20	0.74	0.77	2.08	2.06×10^{-8}	-
	Gravel	2.90	0.77	1.59	4.19	1.03×10^{-8}	-
Uncertainty estimate, Δ:							
13 cm	Clay	0.08	0.1	0.06	0.09	1.2×10^{-8}	0.5×10^{-5}
	Fine sand	0.2	0.3	0.08	0.2	1.6×10^{-9}	0.9×10^{-7}
	Coarse sand	0.3	0.4	0.3	0.4	2.2×10^{-7}	-
	Gravel	0.3	0.7	0.3	0.9	2.5×10^{-7}	-

For the coherent echoes, the timespread seem to be a good discriminator. It is largest for gravel, then fine sand, then coarse sand and then clay. However, one might expect that it would have some dependence on grain size. This does not seem to be the case, as the result for fine sand is larger than the result for coarse sand. As mentioned earlier, it was more difficult to get the fine sand surface levelled. This may have influenced the results here. For the different skewness parameters the results vary. $S1$ and $S2$ seem to give very different results, especially for the gravel surface. $S1$ increases from clay to fine sand, from fine sand to gravel and from gravel to coarse sand at the lower water-depths. However, for the larger water-depths, $S1$ increases from coarse sand to gravel and then from gravel to fine sand. The parameters $S2$ and K yields the same results, except that these parameters are always largest for gravel. The total energy backscattered is largest for the clay surface, the result varies for different water-depths

for the fine and coarse sand surfaces and gravel. The uncertainties in the parameters are again very large, with these included there is not much of a difference in the parameters between the different surfaces.

Table 8.3: Echo energy and shape parameters for the 5 MHz transducer, incoherent intensity.

Water-depth	Surface	Timespread T [µs]	Skewness $S1$	$S2$	Kurtosis K	Total energy TE	Adjusted TE'
13 cm	Clay	1.70	0.74	0.77	2.01	3.25×10^{-8}	1.39×10^{-5}
	Fine sand	2.32	0.88	0.75	2.04	1.58×10^{-8}	8.63×10^{-7}
	Coarse sand	2.53	0.85	0.82	2.21	1.03×10^{-6}	-
	Gravel	4.01	0.22	1.12	2.98	1.13×10^{-6}	-
	Copper	2.13	0.90	0.69	1.88	5.30×10^{-8}	2.21×10^{-4}
22 cm	Clay	1.69	0.71	0.73	1.94	7.61×10^{-9}	3.26×10^{-6}
	Fine sand	2.55	1.07	0.84	2.21	5.29×10^{-9}	2.88×10^{-7}
	Coarse sand	2.70	0.95	0.80	2.13	2.48×10^{-7}	-
	Gravel	3.99	0.48	1.06	2.70	2.34×10^{-7}	-
35 cm	Fine sand	2.96	1.04	0.83	2.21	1.50×10^{-9}	8.15×10^{-8}
	Coarse sand	2.30	0.75	0.91	2.29	1.22×10^{-7}	-
	Copper	2.07	1.02	0.72	1.92	7.01×10^{-9}	2.92×10^{-5}
50 cm	Fine sand	3.63	1.04	0.78	2.04	3.31×10^{-10}	1.80×10^{-8}
	Coarse sand	2.66	0.75	0.79	2.18	2.92×10^{-8}	-
	Gravel	4.61	0.63	1.11	3.00	2.65×10^{-8}	-
	Copper	2.07	0.94	0.72	1.92	2.22×10^{-9}	9.26×10^{-6}

For the incoherent intensities, the timespread seem to be a good discriminator for some sediment types, however, it varies between water-depths for the coarse and fine sand surfaces. It is smallest for clay, then copper, followed by either the coarse or fine sand surface, and is largest for gravel. The skewness, $S1$, seem to discriminate well between the sediments, however, the skewness for copper seem to be variable between water-depths. It should be considered that the measurements on copper only consist of one measurement, while the measurements from the other surfaces are stacked and averaged. Considering the sediments, the skewness $S1$ is consistently largest for fine sand, then coarse sand, then clay and then gravel. The skewness $S2$ is seen to give very different values compared to the values given by the skewness $S1$ for the gravel surface. The skewness $S2$ is largest for gravel, then coarse sand, then clay, then fine sand and then copper, except at 22 cm, where the skewness $S2$ is larger for fine sand than for coarse sand. It should be noted, however, that the values for the fine and coarse sand surfaces, as well as for the clay surface, are very similar. The kurtosis gives about the same result. It seems to increase with grain size, except at the 22 cm water-depth, where the value for fine sand is larger than the value for coarse sand. Hence, there seem to be an indication that these parameters might be useful for classification at this frequency, at least for some sediment types. Again it should be noted that the uncertainty is large. The total energy varies between water-depths for the sand surfaces, and seems to be consistently larger for the clay surface and the copper reflector.

8.2   Spectral moments

van Walree *et al.* [5], as well as Tegowski and Lubniewski [13], have used spectral moments in the frequency domain to describe the shape of the echo envelope spectrum. As the order of

these moments increases, they are increasingly sensitive to high frequency components in the echo envelope. The spectral moment M of order N is defined as

$$M_N = \int\limits_0^\infty S(\omega)\omega^N \, d\omega, \tag{8.7}$$

where $S(\omega)$ is the power spectral density of the echo envelope $s(t)$, and ω is the angular frequency [5]. It is not specified directly, but it seems to be the echo pressure envelope that is used here instead of the intensity envelope, which was used when calculating the energy and shape parameters. Tegowski and Lubniewski [13] use these spectral moments to estimate the spectral width, which is a measure of the spectral power density around the mean frequency, $\overline{\omega}$. They use two definitions of the spectral width, given by

$$\upsilon^2 = \frac{M_0 M_2}{M_1^2} - 1, \tag{8.8}$$

$$\varepsilon^2 = \frac{M_0 M_4 - M_2^2}{M_0 M_4}, \tag{8.9}$$

where M_i is the spectral moment of order i. For a narrow spectrum the parameters become small, $\upsilon^2 \to 0$ and $\varepsilon^2 \to 0$. In cases where the spectral energy is broadly distributed among frequencies, $\varepsilon^2 \to 1$ and υ^2 increases. The spectral skewness describe the shape of the power spectral density, $S(\omega)$, and is defined by [5, 13]

$$\gamma = \frac{M_3}{M_2^{3/2}}. \tag{8.10}$$

8.2.1 Results of calculating the parameters for the echo envelopes from different sediments

The power spectrum was found by Fourier transformation of the mean echo envelope and multiplication by the complex conjugate of the result, which should give the same result as squaring the magnitude of the Fourier transform. The mean echo envelope was found by Hilbert transforming the individual incoherent echo signals, finding the absolute value and then averaging the results for the twenty different signals. It was considered that the signals should be sampled using the same sample frequency for each sediment surface, since the number of points in the integration seemed to affect the calculated parameters. Since the same sample frequency was not used in the actual measurements, this was achieved by interpolation of the signals. Hence, the signals from the clay surface were interpolated with a factor 2 (sample frequency 0.1 GHz), whereas the rest of the measurements were interpolated with a factor 4 (sample frequency 50 MHz). As mentioned before, the measurements on the different sediment surfaces are done using different measurement setups, and the amplitudes of the signals relative to one another can therefore not be compared directly. For this reason, the power spectral density plots were normalized, to show the relative importance of each frequency component. The time series measured are too short to give a good resolution of the frequencies in the power spectral density plot. Techniques to improve the resolution, by for example adding zeroes to the time series, should probably be considered. However, the signals were just looked at as they were, as it was just meant to check whether there was any indication that the spectral skewness could be a good discriminator of different sediments. The results of the spectral width, given by υ^2, and the spectral skewness, γ, are summarized in tables 8.4 and 8.5 for the 1.4 MHz and 5 MHz transducers, respectively. The spectral width, ε^2, gave a result of one for all of the echo envelopes.

Table 8.4: Parameters calculated from spectral moments, 1.4 MHz transducer.

Water-depth	Surface	Spectral width v^2	Spectral skewness γ
13 cm	Fine sand	3.40	0.314
	Coarse sand	3.68	0.251
22 cm	Fine sand	3.67	0.365
	Coarse sand	3.54	0.290
35 cm	Fine sand	4.84	0.415
	Coarse sand	3.66	0.391
50 cm	Fine sand	3.67	0.335
	Coarse sand	3.56	0.401
Uncertainty estimate, Δ:			
13 cm	Fine sand	0.8	0.02
	Coarse sand	5	0.05

Table 8.5: Parameters calculated from spectral moments, 5 MHz transducer.

Water-depth	Surface	Spectral width v^2	Spectral skewness γ
13 cm	Clay	2.42	0.039
	Fine sand	1.97	0.059
	Coarse sand	2.03	0.055
	Gravel	4.32	0.185
	Copper	3.74	0.115
22 cm	Clay	2.68	0.041
	Fine sand	2.34	0.093
	Coarse sand	2.15	0.063
	Gravel	5.15	0.247
35 cm	Fine sand	2.59	0.115
	Coarse sand	1.95	0.063
	Copper	3.42	0.096
50 cm	Fine sand	5.94	0.345
	Coarse sand	2.23	0.079
	Gravel	7.04	0.364
	Copper	3.63	0.102
Uncertainty estimate, Δ:			
13 cm	Clay	0.3	0.005
	Fine sand	0.4	0.01
	Coarse sand	0.7	0.03
	Gravel	0.9	0.05

For the 1.4 MHz transducer, the spectral width is larger for the fine sand surface than for the coarse sand surface, except at the 13 cm water-depth. The spectral skewness is larger for the fine sand surface than for the coarse sand surface except at the 50 cm water-depth. Hence, the correlation here is uncertain, especially when the magntiude of the uncertainties are considered.

For the 5 MHz transducer the spectral width is again larger for the fine sand surface than

the coarse sand surface, except at the 13 cm water-depth. It seems that the spectral width is a good discriminator here, especially for separating the clay and gravel surfaces from the fine and coarse sand surfaces. The spectral skewness seem to be a good discriminator as well at this frequency, at least for the sediments. The results for the copper reflector, seem to be of a more constant nature and not so dependent on water-depth. Looking at the uncertainty, however, the difference in parameters between the different surfaces are not that large. Hence, it is not obvious that this is a good method to discriminate between different sediments.

Chapter 9

Conclusions

Studying backscattering from sediments, even in a controlled laboratory setting where the sediments are known and fairly homogenous, proved to be a difficult task. Backscattering from a random rough surface is a complex problem, as it consists of both coherent and incoherent scattering from the interface as well as scattering from sediment volume inhomogenities. To be able to compare the measurements from different surfaces, it would have been better if the same experimental setup was used for all the measurements. Also, the measurement-series could have been planned better, to allow a better comparison with theory. Especially when considering using different lengths of the transmitted burst for different water-depths.

9.1   Measured echo durations as a function of depth

The measurements on the copper reflector indicate that there is no increase in echo duration with increasing water-depth. While there was some fluctuation in echo duration, there seemed to be no correlation with depth. This could be explained by the fact that for a smooth surface the parts of the beam that hits at an angle away from the normal is reflected away from the transducer (specular reflection). However, due to the finite size of the reflector, secondary lobes and interference effects, some of it should be scattered back to the source.

The individual signals measured from the different sand surfaces and clay, gave variable results. Some of the data fit well with theory, but overall the echo durations fluctuate a great deal, and for some surfaces it even looked like the echo duration was shorter for greater depths. Hence, there is no indication that the echo duration increases systematically with depth. However, it should be considered that the individual signals are subject to large signal variation. The shape and strength of these signals varies as the transducer is moved to insonify different portions of the surface. The method of stacking echo signals, as described in the literature, was therefore looked into.

Considering the stacked coherent envelopes, as well as the total averaged envelopes, these seem to give a more systematic increase in echo duration with depth. Also, the measured echo durations lie closer to the linear graph plotted, which give less uncertainties in the coefficients calculated. The coherent signal envelopes give somewhat different results than the averaged envelopes. However, it varies between the different surfaces which of these give the best fit to the amount of increase in echo duration predicted by the theory discussed in section 2.4. For some of the measurements the increase is a bit higher than predicted, while for others it is lower. There is also a difference in increase looking at the -6 dB level of the signal envelopes compared to the -14 dB level. Especially for the clay measurements, the increase in echo duration is much less than what is predicted by theory. This may be caused by less surface roughness compared to the sand surfaces, and also may be an effect of more penetration into the sediment.

The predicted increase was found using a model where reflection from a plane surface is considered. Hence, there are obviously other scattering effects in the measurements from the different surfaces that affects the echo durations, and could explain the deviations from the theoretical increase. It is seen that the model used in this work is too simple to predict the duration of the returned echoes. A more realistic, and complex, model need to be used to account for the different scattering mechanisms.

9.1.1 Depth-dependence correction

One objective was to look at how the depth-dependence of the echoes could be compensated for. At the frequencies used in these measurements there does not seem to be a trivial relationship between echo duration and water-depth. In addition, the increase in echo duration with water-depth seem to be dependent of sediment type and which scattering effects are dominating the scattering. Hence, a standardised method for depth-dependence correction may prove difficult.

Two of the correction steps suggested by Pouliquen [8] were applied to signals from the coarse and fine sand surfaces, measured with the 5 MHz transducer. The results were given in section 6.6. The measurements were not well enough planned to give the right transmitted burst lengths relative to the water-depths measured, hence the relationship $\tau_0 = \tau H/r$ (see section 2.4.1) was not exact. However, there might be an indication that adjusting the transmitted burst length is a useful step in making the echo envelope depth independent.

9.2 Echo shape parameters and spectral moments

The energy and shape parameters that were calculated gave variable results. While the skewness and kurtosis seem to be good discriminators when considering the coherent intensities using the 1.4 MHz transducer, considering the incoherent intensities seem to give better discrimination for measurements at 5 MHz. One would expect some sort of dependency of the calculated parameters on grain size. However, the sequence of these surfaces seem to be more or less random when looking at the values of the different parameters. There seem to be an indication that some of these parameters are good discriminators, at least to separate between some sediments.

The spectral moments seem to discriminate well between some sediments, however the values for the fine and coarse sand surfaces varies between different water-depths. The spectral width does not seem to have any correlation with grain size, as the values are larger for gravel and clay than for coarse and fine sand. However, the spectral skewness seem to increase from clay to coarse and fine sand, and then to gravel.

In spite of the fact that these measurements are done in a controlled laboratory environment, these parameters do not seem to provide a good discrimination for other than very different sediment types, like clay compared to gravel, considering the estimated uncertainties. Hence, it seems like this method might not be very useful in classification or characterization of the seafloor.

9.3 Further work

New measurements in the laboratory, where the transmitted burst length is carefully adjusted to allow comparison of echo envelopes from several depths transformed to a reference depth, could give a better answer to whether the correction steps suggested by Pouliquen are useful. Also a way to adjust the power and intensity of the echo envelopes should then be looked into and applied to the data.

Although a lot of different physical models of scattering from the ocean floor have been developed, there is yet no single model that can be used to unambiguously characterize the seafloor. Hence, more work should be done in this area.

Bibliography

[1] G. E. O. Schlagintweit. "Real-time acoustic bottom classification for hydrography: A field evaluation of RoxAnn". In *OCEANS '93. Engineering in Harmony with Ocean*, volume **3**, pages 214–219. Canadian Hydrographic Service, Department of Fisheries and Oceans, 1993.

[2] Philippe Blondel. "A review of acoustic techniques for habitat mapping" [online]. Department of Physics, University of Bath, 2008. Available: `http://people.bath.ac.uk/pyspb/research/selected_publications/Blondel_Hydroacoustics_inpress2008.pdf` [November 5th 2009].

[3] L. J. Hamilton. "Acoustic seabed classification systems" [online]. DSTO Aeronautical and Maritime Research Laboratory, 2001. Available: `http://hdl.handle.net/1947/3596` [November 5th 2009].

[4] Paul A. Clarke and L. J. Hamilton. "The ABCS program for the analysis of echo sounder returns for acoustic bottom classification" [online]. DSTO Aeronautical and Maritime Research Laboratory, August 1999. Available: `http://hdl.handle.net/1947/3739` [November 5th 2009].

[5] P. A. van Walree, J. Tegowski, C. Laban, and D. G. Simons. "Acoustic seafloor discrimination with echo shape parameters: A comparison with the ground truth". *Continental Shelf Research*, **25**(18), 2005.

[6] Bjarte Berntsen, Jens M. Hovem, and Oddbjørn Bergem. "Characterization of the seafloor using normal incidence acoustic backscattered time domain signals from a parametric sonar". In *OCEANS '99 MTS/IEEE. Riding the Crest into the 21st Century*, volume **1**, pages 30–36, 1999.

[7] E. Pouliquen, O. Bergem, and N. G. Pace. "Time-evolution modeling of seafloor scatter. I. Concept". *J. Acoust. Soc. Am.*, **105**(6):3136–3141, June 1999.

[8] E. Pouliquen. "Depth-dependence correction for normal incidence echosounding". In *Proceedings of the 7th European Conference on Underwater Acoustics*, Delft, The Netherlands, July 2004.

[9] Philippe Blondel and Nick G. Pace. "Scaled tank experiments: Seabed and target scattering at high frequencies". In *Underwater Acoustic Measurements: Technologies & Results*. Crete, Greece, June 28th - July 1st 2005.

[10] D. Jackson and M. Richardson. *High-frequency seafloor acoustics*. Springer, 2007.

[11] E. Pouliquen and X. Lurton. "Sea-bed identification using echo sounder signals". In *European Conference on Underwater Acoustics*, pages 535–538. Elsevier Applied Science, 1992.

[12] Ben R. Biffard, Jon M. Preston, and N. Ross Chapman. "Acoustic classification with single-beam echosounders: Processing methods and theory for isolating effects on the seabed on echoes". In *Proceedings of Underwater Acoustic Measurements: Technologies & Results*. Crete, Greece, June 2007.

[13] J. Tegowski and Z. Lubniewski. "Seabed characterisation using spectral moments of the echo signal". *Acta Acustica united with Acustica*, **88**:623–626, 2002.

[14] F. B. Jensen, W. A. Kuperman, M. B. Porter, and H. Schmidt. *Computational Acoustics*, chapter 2. Springer/AiP-Press, 2000.

[15] Lawrence E. Kinsler et al. *Fundamentals of Acoustics*. John Wiley & Sons, Inc., 4th edition, 2000.

[16] Magne Vestrheim. "Lecture notes for the course PHYS 272: Akustiske transdusere", UiB, 2008.

[17] Halvor Hobæk. "Lecture notes for the course PHYS 271: Akustikk", UiB, 2008.

[18] D. C. Baird. *An introduction to measurement theory and experimental design*. Prentice-Hall, 1962.

[19] John G. Proakis and Masoud Salehi. *Communication Systems Engineering*. Prentice Hall, 2nd edition, 2002.

[20] H. Medwin and C. S. Clay. *Fundamentals of Acoustical Oceanography*, chapter 7. Academic Press, 1998.

[21] David T. Blackstock. *Physical Acoustics*, chapter 14. John Wiley & Sons, Inc., 2000.

[22] H. Hobæk and A. Heggen. "Analysis of echoes from a plane reflector - steps toward acoustic habitat mapping". In *Proceedings of the 32th Scandinavian Symposium on Physical Acoustics*. Finse, 8-11 February, 2009, R. J. Korneliussen (ed.). The Norwegian Physics CD-rom.

[23] J. A. Ogilvy. *Theory of Wave Scattering from Random Rough Surfaces*. Institute of Physics Publishing, 1991.

[24] Christian Halvorsen. "Resiprositetskalibrering av hydrofoner". Master's thesis in Norwegian, UiB, 1982.

[25] R. V. Hogg and E. A. Tanis. *Probability and statistical inference*. Pearson, Prentice Hall, 7th edition, 2006.

[26] "Lecture notes for the course PHYS114: Grunnleggende målevitenskap", UiB, spring 2007.

Appendix A

Uncertainty calculations

A.1 General expression for uncertainty calculations

If the standard deviation of each of the input variables to an expression is known, the total uncertainty can be calculated. To do this it is also necessary to know the relationship between the measured result and the input variables, $y = f(x_1, x_2, x_3, ..., x_n)$. If the uncertainties of the input variables are denoted by $u(x_1)$, $u(x_2)$,..., $u(x_n)$, the combined uncertainty can be expressed by [26]

$$
\begin{aligned}
u_c(y) &= \sqrt{\left(\frac{\partial f}{\partial x_1}\right)^2 u^2(x_1) + \left(\frac{\partial f}{\partial x_2}\right)^2 u^2(x_2) + ... + \left(\frac{\partial f}{\partial x_n}\right)^2 u^2(x_n)} \\
&= \sqrt{\sum_{i=1}^{n} \left(\frac{\partial f}{\partial x_i}\right)^2 u^2(x_i)},
\end{aligned}
\tag{A.1}
$$

under the assumption that the input variables are independent variables. For an additive expression the results are especially easy to calculate. For example, for the additive expression

$$
y = ax_1 + bx_2 - cx_3 + ...,
\tag{A.2}
$$

where a, b, c,... are constants without uncertainty, and x_1, x_2, x_3,... are independent variables, the expression in equation A.1 becomes

$$
u_c(y) = \sqrt{a^2 u^2(x_1) + b^2 u^2(x_2) + c^2 u^2(x_3) + ...}
\tag{A.3}
$$

A.1.1 Uncertainties in the effective angle and the effective burst length

From equation (2.12), the effective burst length is given by the expression $D = cb$, where c is the sound speed and b is the offset of the linear plot, with uncertainty given in section 2.4. The sound speed is set to 1500 ± 20 m/s. Then the formula for the uncertainty of the effective burst length, can easily be calculated by using equation A.1

$$
u(D) = \sqrt{c^2 u^2(b) + b^2 u^2(c)}.
\tag{A.4}
$$

The factor α is given by $mc/2$, where c is the soundspeed and m is the gradient of the linear equation, with uncertainty given in section 2.4. The uncertainty in α is therefore given by

$$
u(\alpha) = \sqrt{\left(\frac{c}{2}\right)^2 u^2(m) + \left(\frac{m}{2}\right)^2 u^2(c)}.
\tag{A.5}
$$

The effective angle is given by $\theta = \cos^{-1}(1/(\alpha + 1))$. The uncertainty of the effective angle can be found from the uncertainty in α by using the relation

$$\mathrm{d}\theta = \frac{\cos^2 \theta}{\sin \theta} \, \mathrm{d}\alpha, \tag{A.6}$$

which is found using the same standard formula for uncertainty, equation A.1.

A.1.2 Uncertainty in directivity measurements

The directivity measurements, discussed in section 4.3, were done by reading out the trace from the oscilloscope and finding the rms-value of the steady state area of the burst. The uncertainty of the oscilloscope is given to be 2 % of the fullscale-value. For the 5 MHz transducer, the needle-hydrophone was moved in steps of 2 mm by the motor, and signals were recorded in each position. The directivity measurement was programmed, so that the needle hydrophone moved in steps and the computer recorded the signals automatically, without adjusting the scale on the oscilloscope. Hence, the uncertainty of the rms-amplitude in each position is difficult to estimate, as it was not registered how much of the oscilloscope screen was covered by the signal. For the 1.4 MHz transducer, however, the measurements had to be done by moving the hydrophone manually, and the scale on the oscilloscope was adjusted for the signal to cover the whole screen for each measurement. Hence, the instrument uncertainty in this case was 2 % of the rms-value of the signal. Again the hydrophone was moved with steps of 2 mm.

The angle from the acoustic axis, for a specific measurement point, can be found when the distance from the transducer to the needle hydrophone, a, and the distance from the acoustic axis to the measurement point, b, are known. The relation is given by

$$\theta = \tan^{-1}\left(\frac{b}{a}\right). \tag{A.7}$$

Derivation of θ with respect to the variables a and b, give the results

$$\left(\frac{\partial \theta}{\partial a}\right)^2 = \frac{b^2}{(a^2 + b^2)^2},$$

$$\left(\frac{\partial \theta}{\partial b}\right)^2 = \frac{a^2}{(a^2 + b^2)^2},$$

which can be put into the expression of the total uncertainty, given in equation (A.1), to find the uncertainty in the angle of a specific measurement point.

$$\Delta\theta = \sqrt{\left(\frac{\delta\theta}{\delta a}\right)^2 u^2(a) + \left(\frac{\delta\theta}{\delta b}\right)^2 u^2(b)}. \tag{A.8}$$

The distance from the transducer to the needle hydrophone is found by registering the time-delay of the signal upon reception, when the needle hydrophone is centered on the acoustic axis of the transducer, and then multiplying this by the soundspeed in water. The uncertainty in the time-delay read from the oscilloscope is assumed to be negligible in comparison to the uncertainty of the sound speed in water. The sound speed in water, c, is set to 1500 ± 20 m/s. According to equation (A.1), this leads to an expression for the uncertainty of a given by, $u(a) = \tau u(c)$, where τ is the time-delay.

The uncertainty in b is related to the uncertainty in the positioning of the needle-hydrophone. In the case where the needle hydrophone was moved manually, it is related to the uncertainty

in the adjustment wheel used for positioning, as well as the uncertainty in reading the value from this adjustment wheel. The uncertainty in the wheel itself is assumed negligible compared to the uncertainty in actually reading off the position on the wheel. Since the scale on the positioning wheel was divided into 0.1 mm, the uncertainty was set to this value. In addition, when a certain angle is to be determined, e.g. the -3 dB angle, uncertainty in b is also influenced by the uncertainty in the voltage, which is read by the oscilloscope. This relationship is not trivial. The uncertainty of the oscilloscope is given to be 2% of the full-scale value. Therefore, for the 1.4 MHz transducer, the rms-value has an uncertainty of 2%. In dB this is estimated to 0.2 dB. Plotting the measured voltage in dB, relative to the value on the acoustic axis, as a function of position away from the beam axis, the uncertainty in b was estimated. The uncertainty in the dB-level was seen to be small compared to the discretization error introduced, as the needle hydrophone was moved in steps of 2 mm. Hence, the uncertainty was set to half the discretization length, that is 1 mm for this transducer. This is large compared to the uncertainty introduced by reading of the adjustment wheel, hence, the latter was considered negligible. For the 5 MHz transducer, the uncertainty in the rms-value was larger, and the uncertainty in b was therefore estimated to be 2 mm. These values can then be put into equation A.8, to find the uncertainty of a specific angle, e.g. the -3 dB angle. The value of b needs to be read out of the plot for the dB-level as a function of distance away from the acoustic axis. The angles that were found from the directivity plots, were the -3 dB, -6 dB and -7 dB angles. The uncertainties of these angles have been calculated following the procedure discussed here. The uncertainty in angle calculated by equation (A.8) is given in radians, and was transformed to degrees.

A.4

Appendix B

Helmholtz-Kirchhoff integral theorem

The inhomogenous wave equation with sources represented as forced mass injection is given by the equation

$$\nabla^2 \psi - c^{-2} \frac{\partial^2 \psi}{\partial t^2} = f(\mathbf{r}, t). \tag{B.1}$$

In the frequency domain this turns into the Helmholtz equation

$$[\nabla^2 + k^2(\mathbf{r})] \psi(\mathbf{r}, \omega) = f(\mathbf{r}, \omega). \tag{B.2}$$
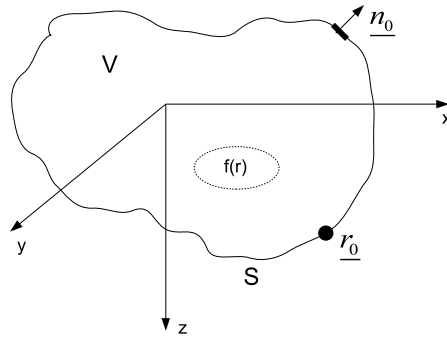
Figure B.1: Bounded volume V containing a source of sound.

Now, looking at a source in a medium occupying a volume V, and bounded by the surface S, an acoustic field is set up in the volume by the distribution of volume forces $f(\mathbf{r})$ inside the volume V (illustrated in figure B.1). The displacement potential $\psi(\mathbf{r})$ must therefore satisfy the inhomogenous Helmholtz equation, equation (B.2). The free-field Green's function, $g_\omega(\mathbf{r}, \mathbf{r}_0) = \frac{e^{ikR}}{4\pi R}$, where $R = |\mathbf{r} - \mathbf{r}_0|$ for a point source located in $\mathbf{r} = \mathbf{r}_0$, is a particular solution of the equation (B.2). However, for a problem with boundary conditions, the general solution is needed. This is given by the sum of a particular solution and the solution of the homogenous Helmholtz equation. The general Green's function is introduced

$$G_\omega(\mathbf{r}, \mathbf{r}_0) = g_\omega(\mathbf{r}, \mathbf{r}_0) + H_\omega(\mathbf{r}), \tag{B.3}$$

where $H_\omega(\mathbf{r})$ is an arbitrary function satisfying the homogenous Helmholtz equation, $[\nabla^2 + k^2(\mathbf{r})]H_\omega(\mathbf{r}) = 0$. The general Green's function must satisfy the inhomogenous Helmholtz equation, the boundary conditions and the radiation condition.

For an omnidirectional source located in $\mathbf{r} = \mathbf{r}_0$, the acoustic field is only dependent on

the distance from the source, and the solution is therefore easier to represent in a spherical coordinate system, with the reduced Helmholtz equation

$$\left[\frac{1}{r^2} \frac{\partial}{\partial r} r^2 \frac{\partial}{\partial r} + k^2 \right] \psi(r) = 0. \tag{B.4}$$

Equation (B.4) has the solutions

$$\psi(r) = \begin{cases} (A/r)e^{ikr}, \\ (B/r)e^{-ikr}. \end{cases} \tag{B.5}$$

These solutions represent diverging and converging, spherical waves, respectively. Looking first at the acoustic field produced by a small point source with radius a in a homogenous fluid with no surrounding boundaries, the surface displacement of the point source is given by

$$u_r(t, a) = U(t). \tag{B.6}$$

In the homogenous fluid the field will be omnidirectional, with a radial displacement

$$u_r = \frac{\partial \psi(r, t)}{\partial r}, \tag{B.7}$$

where the displacement potential ψ satisfy a homogenous wave equation. By taking the Fourier transform of the wave equation and the boundary condition at $r = a$, equation (B.6), what remains is the Helmholtz equation (B.4) and the boundary condition

$$u_r(a) = U(\omega). \tag{B.8}$$

The radiation condition, claiming no incoming waves from infinity, gives $B = 0$ for the solutions of the Helmholtz equation given in (B.5). This means that

$$\psi(r) = A \frac{e^{ikr}}{r}, \tag{B.9}$$

which leads to the displacement field by using equation (B.7)

$$u_r(r) = A e^{ikr} \left(\frac{ik}{r} - \frac{1}{r^2} \right). \tag{B.10}$$

Setting $r = a$ in equation (B.10), leads to

$$u_r(\omega, a) = A e^{ika} \frac{ika - 1}{a^2} \simeq -\frac{A}{a^2}, \tag{B.11}$$

since the radius of the simple point source is small compared to the acoustic wavelength, $ka \ll 1$. An expression for the amplitude, A, can then be found, using the boundary condition in equation (B.8)

$$A = -a^2 U(\omega). \tag{B.12}$$

The source strength is now defined by, $S_\omega = 4\pi a^2 U(\omega)$, as the volume-injection amplitude produced by the source driven with the angular frequency ω. When these expressions are put into equation (B.9) the solution for the field in the fluid can be expressed as

$$\psi(r) = -S_\omega \frac{e^{ikr}}{4\pi r}, \tag{B.13}$$

B.2

containing the Green's function, $g_\omega(r, 0)$. The free-field Green's function satisfy the inhomogenous Helmholtz equation

$$\left[\nabla^2 + k^2\right] g_\omega(\mathbf{r}, \mathbf{r}_0) = -\delta(\mathbf{r} - \mathbf{r}_0). \tag{B.14}$$

This can be checked by integration of equation (B.14) over a small volume containing the point source in $\mathbf{r}_0$. The general Green's function must therefore satisfy the same Helmholtz equation as the free-field Green's function, which gives

$$\left[\nabla^2 + k^2\right] G_\omega(\mathbf{r}, \mathbf{r}_0) = -\delta(\mathbf{r} - \mathbf{r}_0). \tag{B.15}$$

By multiplying equation (B.2) with $G_\omega(\mathbf{r}, \mathbf{r}_0)$ and equation (B.15) with $\psi(\mathbf{r})$ and then subtracting the two equations the result is

$$G_\omega(\mathbf{r}, \mathbf{r}_0)\nabla^2\psi(\mathbf{r}) - \psi(\mathbf{r})\nabla^2 G_\omega(\mathbf{r}, \mathbf{r}_0) = \psi(\mathbf{r})\delta(\mathbf{r} - \mathbf{r}_0) + G_\omega(\mathbf{r}, \mathbf{r}_0)f(\mathbf{r}). \tag{B.16}$$

Further, switching $\mathbf{r}$ and $\mathbf{r}_0$, integration of equation (B.16) over the volume V, with respect to $\mathbf{r}_0$, and also assuming that the Green's function is symmetrical, $G_\omega(\mathbf{r}, \mathbf{r}_0) = G_\omega(\mathbf{r}_0, \mathbf{r})$, one ends up with equation

$$\int_V \left[G_\omega(\mathbf{r}, \mathbf{r}_0)\nabla_0^2\psi(\mathbf{r}_0) - \psi(\mathbf{r}_0)\nabla_0^2 G_\omega(\mathbf{r}, \mathbf{r}_0)\right] \mathrm{d}V_0$$
$$= \int_V \psi(\mathbf{r}_0)\delta(\mathbf{r} - \mathbf{r}_0)\,\mathrm{d}V_0 + \int_V G_\omega(\mathbf{r}, \mathbf{r}_0)f(\mathbf{r}_0)\,\mathrm{d}V_0. \tag{B.17}$$

With the use of integration by parts, Green's first identity, the volume integral on the right side of equation (B.17) can be transformed into a surface integral

$$\psi(\mathbf{r}) = \int_S \left[G_\omega(\mathbf{r}, \mathbf{r}_0)\frac{\partial\psi(\mathbf{r}_0)}{\partial\mathbf{n}_0} - \psi(\mathbf{r}_0)\frac{\partial G_\omega(\mathbf{r}, \mathbf{r}_0)}{\partial\mathbf{n}_0}\right] \mathrm{d}S_0 - \int_V G_\omega(\mathbf{r}, \mathbf{r}_0)f(\mathbf{r}_0)\,\mathrm{d}V_0, \tag{B.18}$$

where $\mathbf{n}_0$ is the surface normal, pointing out of the volume. Equation (B.18) is Green's theorem for sources in a bounded medium. By letting the field points $\mathbf{r}_0$ be located on the boundary of the volume, equation (B.18) becomes an integral equation that has to be solved for the field and the normal derivative of the field on the boundary. Then equation (B.18) can be used to find the field in an arbitrary point $\mathbf{r}$ inside the volume V.

When sound is received the source is not active. Then equation (B.18), for a bounded volume without sources, can be used to find the field

$$p(\mathbf{r}) = \int_S \left(G_\omega(\mathbf{r}, \mathbf{r}_0)\nabla_0 p(\mathbf{r}_0) - p(\mathbf{r}_0)\nabla_0 G_\omega(\mathbf{r}, \mathbf{r}_0)\right) \cdot \mathrm{d}\mathbf{S}_0. \tag{B.19}$$

B.3

Appendix C

MATLAB-scripts

This chapter contains the MATLAB-scripts used for communication with the instruments, control of the positioning system, and signal processing. The scripts that I wrote myself are marked with (A), while the other scripts were obtained from my supervisor Halvor Hobæk.

C.1   lecgethx.m

Program that reads in the signal from the oscilloscope

```
function [samples] = lecgethx(ch)
% ch er streng: TA, TB, TC, TD, M1, M2, M3, M4, C1, C2
% Overføring av data binær form
% Halvor Hobæk 5/12-2006, OK

system('del data-lest');
%
ud=gpib('dev', 0,4,0,10,1,0);
ch='TA';
cmd=[ ch ':WF? DAT1']; % her er det det stopper ...

ibsta=gpib('wrt',ud,cmd);% The actual sending of the command
pause(5);
a=gpib('rdf',ud,'data-lest');
f=fopen('data-lest','rb');
t=fscanf(f,'%2x',inf); % Read response

samples(1:length(t))=(t(1:length(t))-256*(t(1:length(t))>127));
fclose(f);
%fclose(ud);
%[m,k]=size(vektor);
end
```

C.2   lecinit.m

Program for initialization of the oscilloscope for transfer of data

```
function lecinit()
% Initialisering av scopet:

% Responsformatet:
lecset('CHDR OFF');

%Set offset
```

```
% Hex-overføring:
lecset('CFMT OFF,BYTE,HEX');
% Datamengden som skal overføres:max
resp=['WFSU SP,0,NP,0,FP,0'];
lecset(resp);
end
```

C.3   lecskalering.m

Program for getting the scaling factors for the oscilloscope

```
function sk = lecskalering(ud,ch)

% sk=skalering(ch) , funksjon for getting scaling factors for Lecroy 9350
% sk(1)=skale for voltage, sk(2:3) for timebase
ud=gpib('dev', 0,4,0,10,1,0);
cmd='CHDR OFF';
ibsta = gpib('wrt',ud,cmd);
cmd=['C' num2str(ch) ':VDIV?'];
ibsta = gpib('wrt',ud,cmd);
s = gpib('rd',ud);
skk=str2num(s);
p=1;%eventuell probesetting
sk(1)=skk*5/128/p;% scaling factor vertical
cmd='TDIV?';%'HOR:MAI:SCA?';
ibsta=gpib('wrt',ud,cmd);
sk1=gpib('rd',ud);
sk(2)=str2num(sk1);  %oppløysning TDIV
cmd='TRIG_DELAY?';%'HOR:MAI:POS?';
ibsta=gpib('wrt',ud,cmd);
pos=gpib('rd',ud);
sk(3)=str2num(pos); %trigger delay
sk(4)=skk; % skopscale, oppløysning VDIV
sk(5)=p; % eventual probe-setting
```

C.4   stepperstart.m

Program that initiates the motor controller

```
%stepperstart.m  skript for initiering av motorstyring i glasstank
% 31/10-2008, HH
s1=serial('COM3','Terminator','*');
fopen(s1);
fprintf(s1,'2V'); %sett kontroller i rett verbose mode
fgets(s1); %fjern respons
% initierer motorene.  Motor  W (LW,WDR,WST)
fprintf(s1,'1B 1000W 64g');% 1000 er passe fart, -> W
fgets(s1);
fprintf(s1,'2B 1000W 16g');% -> X
fgets(s1);
fprintf(s1,'4B 700W 4g');% -> Y
fgets(s1);
fprintf(s1,'8B 1000W 1g');% -> Z
fgets(s1);
tombuff(s1);
```

C.5 motorX.m

Program that controls motor X

```
function st=motorX(s1,steg,test)
%program for å kjøre motor X
%3/11-08 HH
fart=800;
st=0;
dir='C'; %default utover
maske=32;
if (steg<0)
    dir='0';% %innoverr
    maske=16;
end
tombuff(s1);
r=estoppstatus(s1);
if maske ~= r %OK kan kjøre
    fprintf(s1,['8' dir]); % sett retning
    fprintf(s1,'4B 4g'); %sett generator 3 -> Y
    fprintf(s1,[num2str(fart) 'W']); % sett fart
    fprintf(s1,[num2str(abs(steg)) 'G']); %start motor
    st=1;
end
tombuff(s1);
if test>0
    tt=0;
    while tt==0
        r=estoppstatus(s1);
         if r==maske
            fprintf(s1,'0G'); %stopp motor
            tt=1;
         end
        fprintf(s1,'-11?');nn=fgets(s1);fgets(s1);
        L=length(nn)-1;
        r=str2num(nn(7:L));

        tt=r-1; % bryt her hvis motoren er kommet fram
    end
    st=2;
end
tombuff(s1);
```

C.6 motorY.m

Program that controls motor Y

```
function st=motorY(s1,steg,test)
%program for å kjøre motor Y
%31/10-08 HH
fart=800;
st=0;
dir='C'; %default mot øst
maske=2;
if (steg<0)
    dir='0';% %vest
    maske=1;
end
tombuff(s1);
r=estoppstatus(s1);
if maske ~= r %OK kan kjøre
    fprintf(s1,['128' dir]); % sett retning
    fprintf(s1,'1B 64g'); %sett generator 1 -> W
    fprintf(s1,[num2str(fart) 'W']); % sett fart
    fprintf(s1,[num2str(abs(steg)) 'G']); %start motor
```

```
        st=1;
end
tombuff(s1);
if test>0
        tt=0;
        while tt==0
            r=estoppstatus(s1);
            if r==maske
                fprintf(s1,'0G'); %stopp motor
                tt=1;
            end
            fprintf(s1,'-11?');nn=fgets(s1);fgets(s1);
            L=length(nn)-1;
            r=str2num(nn(7:L));
            tt=r-1; % bryt her hvis motoren er kommet fram
        end
        st=2;
end
tombuff(s1);
```

C.7 motorZ.m

Program that controls motor Z

```
function st=motorZ(s1,steg,test)
%program for å kjøre motor Y
%3/11-08 HH
fart=600;
st=0;
dir='C'; %default nedover
maske=8;
if (steg<0)
    dir='O';% %oppover
    maske=4;
end
tombuff(s1);
r=estoppstatus(s1);
if maske ~= r %OK kan kjøre
    fprintf(s1,['32' dir]); % sett retning
    fprintf(s1,'2B 16g'); %sett generator 2 -> X
    fprintf(s1,[num2str(fart) 'W']); % sett fart
    fprintf(s1,[num2str(abs(steg)) 'G']); %start motor
    st=1;
end
tombuff(s1);
if test>0
    tt=0;
    while tt==0
        r=estoppstatus(s1);
        if r==maske
            fprintf(s1,'0G'); %stopp motor
            tt=1;
        end
        fprintf(s1,'-11?');nn=fgets(s1);fgets(s1);
        L=length(nn)-1;
        r=str2num(nn(7:L));
        if r==0
            tt=1; % bryt her hvis motoren er kommet fram
        end

    end
    st=2;
end
tombuff(s1);
```

C.8 motorW.m

Program that controls motor W

```
function st=motorW(s1,steg,test)
%program for å kjøre motor W, roterar kilda
%3/11-08 HH Testet OK
fart=600;
st=0;
dir='C';  %default
maske=32;
if (steg<0)
    dir='O';% %motsatt
    maske=16;
end
tombuff(s1);
r=estoppstatus(s1);
if maske ~= r %OK kan kjøre
    fprintf(s1,['2' dir]); % sett retning
    fprintf(s1,'8B 1g'); %sett generator 4 -> Z
    fprintf(s1,[num2str(fart) 'W']); % sett fart
    fprintf(s1,[num2str(abs(steg)) 'G']); %start motor
    st=1;
end
tombuff(s1);
if test>0
    tt=0;
    while tt==0
        r=estoppstatus(s1);
         if r==maske
            fprintf(s1,'0G'); %stopp motor
            tt=1;
         end
         fprintf(s1,'-11?');nn=fgets(s1);fgets(s1);
         L=length(nn)-1;
         r=str2num(nn(7:L));
         if r==0
            tt=1; % bryt her hvis motoren er kommet fram
         end
    end
    st=2;
end
tombuff(s1);
```

C.9 motorYW.m

Program used to control motor Y, was used to rotate the transducer when motor W stopped working

```
function st=motorY(s1,steg,test)
%program for å kjøre motor Y
%31/10-08 HH
st=0;
dir='C'; %default mot øst
maske=2;
if (steg<0)
    dir='O';% %vest
    maske=1;
end
tombuff(s1);
r=estoppstatus(s1);
if maske ~= r %OK kan kjøre
    fprintf(s1,['128' dir]); % sett retning
    fprintf(s1,'1B 64g'); %sett generator 1 -> W
```

C.5

```
        fprintf(s1,[num2str(abs(steg)) 'G']); %start motor
        st=1;
end
tombuff(s1);
if test>0
        tt=0;
        while tt==0
            r=estoppstatus(s1);
            if r==maske
                fprintf(s1,'0G'); %stopp motor
                tt=1;
            end
            fprintf(s1,'-11?');nn=fgets(s1);fgets(s1);
            L=length(nn)-1;
            r=str2num(nn(7:L));
            tt=r-1; % bryt her hvis motoren er kommet fram
        end
        st=2;
end
tombuff(s1);
```

C.10   rmsber.m

Program that calculates the rms-amplitudes of a signal vector

```
function rms=rmsber(dd,range)
%function r=rmsber(dd,range)
%beregnar amplitudea av ein måleserie,
%basert på rms-verdien. Men amplituda er
%vanleg absolutt amplitude.
%dd inneheld måleserien i format dd(serienr.,plukk)
%range bestemmer området av plukk som skal brukast,
%eks. 300:1000.
%modifisert for å fjerne dc-offset 25/2-05 HH
n=size(dd)
nn=n(1); %antall målingar i serien
if nargin==1
    range=1:n(2);
end
for j=1:nn
    a=dd(j,range)-mean(dd(j,range));
    rms(j)=sqrt(2*mean(a.^2));
end
```

C.11   sentreringrotasjon.m (A)

Program that rotates the transducer through an angle finding the position where the signal is strongest

```
%sentrering rotasjon
motorYW(s1,-300,1);
motorYW(s1,100,1);
pause(60)
for i=1:17
    pause(15)
    i
    dd(i,:)=lecgethx('TA');
    motorYW(s1,25,1);
end
motorYW(s1,-325,1);
motorYW(s1,100,1);
```

```
snittrot=rmsber(dd,150:350);
plot(snittrot);
save nyrotsentrering.mat;
```

C.12   sentreringvertikalt.m (A)

Program that moves the hydrophone through a given number of steps finding the position where the signal is strongest

```
%sentrering vertikalt
motorZ(s1,-1400,1);
motorZ(s1,200,1);
pause(60)
for i=1:13
    pause(30)
    i
    dd(i,:)=lecgethx('TA');
    motorZ(s1,200,1);
end
motorZ(s1,-1600,1);
motorZ(s1,200,1);
snittrot=rmsber(dd,150:350);
plot(snittrot);
save vertsentrering.mat;
```

C.13   sentreringhorisontalt.m (A)

Program that moves the hydrophone through a given number of steps finding the position where the signal is strongest

```
%sentrering horisontalt
motorY(s1,-250,1);
motorY(s1,100,1);
pause(60)
for i=1:31
    pause(30)
    i
    dd(i,:)=lecgethx('TA');
    motorY(s1,10,1);
end
motorY(s1,-260,1);
motorY(s1,100,1);
snittrot=rmsber(dd,150:350);
plot(snittrot);
save horsentrering.mat;
```

C.14   signalvar.m (A)

Program that reads out the signal from the oscilloscope every 30 seconds over a time period of 20 minutes

```
%signalvariasjon
lecinit()
pause(30)
for i=1:40
```

```
    dd(i,:)=lecgethx('TA');
    pause(30)
end
snittsig=rmsber(dd,100:500);
plot(snittsig);
save signalvar22cm.mat;
```

C.15 interpol.m

Program that interpolates a signal vector

```
function sig=interpol(a,n)
% sig=interpol(a,n)
%
% Interpolerer i vektoren a med faktoren n, dvs. n=4 gir
% 3 verdier mellom to naboplukk
%
% H.H. 19/5-94,20/5
%
[n1,n2]=size(a);
if n1>n2
a=a';
end
% gjor om saa plukkene ligger som  rekkevektorer
[n1,n2]=size(a);
aa=zeros(n1,n*n2);% ny signalvektor (matrise)
for i=1:n2
aa(:,n*i)=a(:,i);
end
ma=fix(n2/2);
x=(1:ma)*pi/n;
si=sin(x)./x;
sinc=[fliplr(si) 1 si];% Dette er sinc-funksjoen aa folde med
for j=1:n1
sigg=conv(sinc,aa(j,:));
sig(j,:)=sigg(ma+n:ma+n-1+n*n2);% plukker ut relevante elementer
end
```

C.16 indeks.m

Program that locates the index of the zero-crossing closest to a pre-defined index

```
function ind=indeks(a,n,p)
    %Finn indeks for nullgjennomgang i nærheit av indeks p
    %
    %interpolerar først for å få fleire punkt slik at ein kjem nærare nullpunkt
    %    dette vert gjort med interpol.m som inneheld vektor a og n angir
    %    multipliseringsfaktor

S=interpol(a,n);
n=find(S>0);
nn=diff(n);
m=find(nn>1);
M=find(n(m)>p);
ind=n(m(M(1)))
```

C.17 fasejuster.m (A)

Program that phase-aligns each signal vector in the stack relative to an index set by looking
at the individual signals in the stack:

```
%function kohsig=fasejuster(a,n)
%program som fasejusterer ei rekke med signal a(1:n,:) i forhold til første målte
%signal a(1,:)
p=1300;
a=s;
n=20;
kohsig(1,:)=interpol(a(1,:),4);
ind(1,:)=indeks(a(1,:),4,p);

for i = 2:n
    kohsig(i,:)=interpol(a(i,:),4);
    ind(i,:)=indeks(a(i,:),4,p);
    diffind=ind(1,:)-ind(i,:);
    if diffind >= 0
        kohsig(i,:)=[zeros(1,diffind) kohsig(i,1:(4008-diffind))];
    else
        kohsig(i,:)=[kohsig(i,(abs(diffind)+1):4008) zeros(1,abs(diffind))];
    end
end
```

C.18 fasejuster2.m (A)

Program that phase-aligns each signal vector in the stack relative to an index set by looking
at the individual signals in the stack, also considers the bottom pick of signals:

```
%function kohsig=fasejuster(a,n)
%program som fasejusterer ei rekke med signal a(1:n,:) i forhold til første målte
%signal a(1,:), tek hensyn til forskjellig start
terskel=0.002;
p1=1410;
p=p1;
a=s;
n=20;
kohsig(1,:)=interpol(a(1,:),4);
ind(1,:)=indeks(a(1,:),4,p);
te=find(kohsig(1,:)>terskel);
n1=te(1);

for i = 2:n
    kohsig(i,:)=interpol(a(i,:),4);
    te=find(kohsig(i,:)>terskel);
    n2=te(1);
    p2=n2-n1;
    p=p1+p2;
    ind(i,:)=indeks(a(i,:),4,p);
    diffind=ind(1,:)-ind(i,:);
    if diffind >= 0
        kohsig(i,:)=[zeros(1,diffind) kohsig(i,1:(4008-diffind))];
    else
        kohsig(i,:)=[kohsig(i,(abs(diffind)+1):4008) zeros(1,abs(diffind))];
    end
    p=p1;
end
```

C.19 imprespons.m

Program that finds the impulse response of the transducer and reconstructs the output signal:

```
function [h,B]=imprespons(signalinn,signalut,N,g)
%Finds the impulse response when input and output signals are known
%N is adjusted to remove noise - Typically 50
%19/2-09 HH
%The signals are made of equal length if they are not already
%Assumes signal out longer than the input signal
%Note: signals must be sampled with the same sampling frequency!
%Outputs also RMS of difference between reconstruction and signal_out
%Avoid plotting if g=0!
n1=length(signalinn);
n2=length(signalut);
if n1>n2
warning('Make signal out longer than input signal!')
break
end
s2=[signalut zeros(1,n2)];
s1=[signalinn zeros(1,2*n2-n1)];
S1=fft(s1);
S2=fft(s2);
jj=max(abs(S1));
mm=find(abs(S1)>jj/N);%Finds signifikant values
Z=zeros(1,length(S2));
b=S2(mm)./S1(mm);
Z(mm)=b;%enters significant values
h=ifft(Z);
h=h(1:n2);%keep only what is relevant
B=real(conv(h,signalinn));
if g!=0
figure
plot(1:n2,B(1:n2),1:n2,signalut,'r')
xlabel('Index');
legend('Reconstruction','Original');
title(['Test of impulse response function: reconstruction and original. N = ' num2str(N)])
figure
%plot(1:n2,B(1:n2)-signalut)
diff=sqrt(sum((B(1:n2)-signalut).^2)/n2);
%title(['Difference, RMS= ' num2str(diff)])
plot(abs(fft(h))(1:70))
title(['Frequency response, RMS= ' num2str(diff)])
h1=fft(abs(signalut));
figure
plot(abs(h1))
L=input('Lengden av lavfrekvens:');
hh1=[h1(1:L) zeros(1,n2-2*L-1) h1(end-L:end)];
Env1=abs(ifft(hh1));
h2=fft(abs(B(1:n2)));
hh2=[h2(1:L) zeros(1,n2-2*L-1) h2(end-L:end)];
Env2=abs(ifft(hh2));
plot(1:n2,Env2,1:n2,Env1,'r')
title('Envelopes of reconstruction and measured')
xlabel('Index')
legend('Reconstruction','Original');
end
```

C.20   impresanal.m

Program that finds the simulated electrical signal:

```
%Benytt P=0 for å unngå plotting
%load /Home/siv16/nfyhh/work/Victor/measurements/signalinn2o.mat
load signalinn2.mat
ss=data(50:end-6);%fjerner start og slutt!
ss=ss-mean(ss);%tar bort DC

load datan.mat
y1=datan(8:end);
y1=y1-mean(y1);% fjerner DC
```

```
[h30,B]=imprespons(ss,y1,30,P);
if(P!=0)
figure
R30=conv(h30,ff);
lR=length(R30);
dt=1e-8;
plot(((1:lR)-1)*dt,real(R30))
xlabel('Time -s')
title([num2str(f/1e6) ' MHz, N=30, convolution with impulse response'])
legend('Expected electric signal from transducer')
end
```

C.21   indata4.m

Program that sets the parameter needed in `Ekko`, to calculate the pressure field from a copper reflector:

```
%script indata.m
% for setting run-parameters
clear I I2 I3 pp r RR

th0=2.5*pi/180;%3.65 degrees
f=5e6;      %frekvens (Hz)
h=0.10;        %height (m)
ka=1.61/sin(th0);
dt=1e-8;

rho=1000;  %density of water
c=1500;        %sound speed in water
k=2*pi*f/c;
rho1=8500;%2070;% sand; 8500; % density of copper
c2=5000;%1730;% sand; 5000; % sound speed in copper

dr=c*dt;
r=h:dr:2*h;
lr=length(r);
ncycl=10;
N=200;
t0=2*h/c;% offset
%reflection coefficient
z0=rho*c;
costh=h./r; % relation between angle and range
z2=c2*rho1; %impedance
h2=(c2/c)^2;
costh2=sqrt(1-h2+h2*(h./r).^2);
%RR=2*z2./costh2./(z2./costh2+z0./costh);% 1+R
RR=(z2./costh2-z0./costh)./(z2./costh2+z0./costh);

%directivity
% chose from theta_3dB:


costh=h./r; % relation between angle and range
sinth=sqrt(1-costh.^2);
D=2*(besselj(1,ka*sinth)+eps/2)./(ka*sinth+eps);
```

C.22   Ekko.m

Program that calculates the pressure fielda after reflection from a copper reflector:

```
%skript echo
%hh 28/10-09
close all
indata4; %read parameters
load datan
ff=datan;% pulse form

kern1=costh.*exp(i*k*(r))./r.*(i*k-1 ./r)*dr; % basic part of integrand

%Now directivity:
% chose from theta_3dB:

kern2=kern1.*D.^2;

%now refelction coefficient

kern3=kern2.*RR;

I=conv(kern3,ff);

tr=(2*r-h)/c;% time after arrival of pulse front

%load /Home/siv16/nfyhh/work/Victor/measurements/analysis_1Feb.mat
load signal13cm.mat %AH
msig=data10(27:end);%Målt signal
figure(1)
env1=Env(real(I));
%n=1:nm;
n=1:2001;
plot(tr(n),real(I(n)), tr(n),env1(n),'r')
title(['Simulated pressure of echo from Cu bottom, depth ' num2str(h) ' [m], ncycl ' num2str(ncycl) ', freq ' num2str(f/1000) '
%xlabel('Total range - m')
xlabel('Time - s')
ylabel('Pressure, relative')
legend('Signal','Envelope')
% Beregner signalet gjennom transduseren igjen -> elektrisk signal
P=0;% Unngå plotting
impresanal5MHz
figure
R30=conv(h30,I);
lR=length(R30);
env2=Env(real(R30));
plot(tr(n),real(R30(n)),tr(n),env2(n))
title(['Simulated signal of echo from Cu bottom, depth ' num2str(h) ' [m], ncycl ' num2str(ncycl) ', freq ' num2str(f/1000) ' [
 xlabel('Time - s')
ylabel('Voltage, relative')
figure
Dt=2e-8;
tnn=(1:length(msig))*Dt;
env3=Env(msig);
plot(tnn,msig,tnn,env3)
title(['Electric signal measured from the transducer, depth ' num2str(h) ' [m], ncycl ' num2str(ncycl) ', freq ' num2str(f/1000)
xlabel('Time - s')
ylabel('Voltage, relative')

figure
 plot(tr(n),20*log10(env1(n)/max(env1)),tr(n),20*log10(env2(n)/max(env2)),tnn,20*log10(env3/max(env3)))
title('Comparison of envelopes')
legend('Pressure signal','Electric signal','measured signal')
xlabel('Time - s')
ylabel('dB')

 %figure
A1=20*log10(env1(n)/max(env1));
D1=find(A1>-14);
T1=dt*(D1(end)-D1(1));
A1=20*log10(env2(n)/max(env2));
D1=find(A1>-14);
T2=dt*(D1(end)-D1(1));
A1=20*log10(env3/max(env3));
D1=find(A1>-14);
T3=Dt*(D1(end)-D1(1));
```

```
[-14 h T1 T2 T3]
```

C.23 Env.m

Program that finds the envelope of the simulated signal:

```
function env=Env(sig);
% funksjon for Ã¥ lage omhylningskurver av periodisk signal
n=length(sig);
A=fft(abs(hilbert(sig)));
L=floor(n/26);
hh=[A(1:L) zeros(1,n-2*L-1) A(n-L:n)];
env=abs(ifft(hh));
```

C.24 nyskewness.m (A)

Program that calculates energy and shape parameters of the intensity envelopes:

```
function skew=nyskewness(s)
        %finn skewness og kurtosis for ein
        %envelope, fourier transformerer først for
        %å finne envelope og plukkar deretter ut relevant del
        %av envelope

fff=fft(s);
ff=[fff(1:90) zeros(1,4008-180) fff(3919:4008)];
envelope=abs(ifft(ff));
nn=find(envelope>0.005*max(envelope));
diff=max(nn)-min(nn);
start=min(nn);
stop=max(nn);
diff=stop-start;
envelope=envelope(start:stop).*2;
for i=1:(diff+1)
    tellar1(i)=(envelope(i)-mean(envelope))^3;
end
for i=1:(diff+1)
    tellar2(i)=(envelope(i)-mean(envelope))^4;
end
n=1:diff+1;
nys=s(start:stop);
plot(n,nys,n,envelope,'r')
skew=sum(tellar1)/(diff*std(envelope)^3);
kurtosis=sum(tellar2)/(diff*std(envelope)^4)

%anna metode

for n=1:diff+1
    E(n)=envelope(n);
end
dt=20e-6/4000;
E=E*dt;
TE=sum(E) %total energi

for n=1:diff+1
    t=n*20e-6/4000;
    E2(n)=envelope(n)*t;
end
E2=E2*dt;
t0=(1/TE)*sum(E2); %echo center of gravity
```

```
for n=1:diff+1
    t=n*20e-6/4000;
    E3(n)=envelope(n)*(t-t0)^2;
end
E3=E3*dt;
T=sqrt((4/TE)*sum(E3)) %timespread

for n=1:diff+1
    t=n*20e-6/4000;
    E4(n)=envelope(n)*(t-t0)^3;
end
E4=E4*dt;
S=(8/(T^3*TE))*sum(E4) %skewness
```

C.25   specskewness.m (A)

Program that calculates spectral moments for the pressure envelopes:

```
function spec=specskewness(s,sampfr)

% Find echo envelope
for i=1:20
    hilb(i,:)=hilbert(s(i,:));
    hilb(i,:)=abs(hilb(i,:));
end
envelope=mean(hilb);
plot(envelope)

% Find power spectrum
fff=fft(envelope);
l=length(fff);
Pyy=fff.*conj(fff)/l;
frekvens=sampfr*(0:l/2)/l;
omega=2*pi*frekvens;
Pyy=Pyy(1:l/2+1)/max(Pyy);
plot(omega,Pyy)

%Calculate spectral moments
df=sampfr/l;
domega=2*pi*df;
m0=sum(Pyy).*domega %zero-moment, total signal energy
m1=sum(Pyy.*omega.*domega);
m2=sum(Pyy.*omega.^2.*domega);
m3=sum(Pyy.*omega.^3.*domega);
m4=sum(Pyy.*omega.^4.*domega);

%Spectral width
spw=m0*m2/m1.^2-1
spw2=(m0*m4-m2.^2)/(m0*m4)

%Spectral skewness
spec=m3/(m2.^(3/2));
```

C.26   linearplot.m (A)

Program that makes a linear plot with error bars for the measurements points:

```
%Program som lagar lineært plott av data som er lest ut
%frå signal envelope, ekkolengde vs. djubde, med errorbars

x=[0.13 0.20 0.29 0.35 0.50];
```

```
x2=0:0.01:0.60;
y6dB=[3.2e-6 3.32e-6 3.3e-6 3.06e-6 3.09e-6];
y14dB=[4.94e-6 5.18e-6 5.29e-6 4.56e-6 4.75e-6];
E6dB=[0.036e-6 0.036e-6 0.086e-6 0.028e-6 0.036e-6];
E14dB=[0.054e-6 0.036e-6 0.11e-6 0.059e-6 0.12e-6];
p6dB=polyfit(x,y6dB,1);
yline6dB=p6dB(1)*x2+p6dB(2);
p14dB=polyfit(x,y14dB,1);
yline14dB=p14dB(1)*x2+p14dB(2);

%Plotting
hold on
errorbar(x,y6dB,E6dB,'.','MarkerSize',3)
errorbar(x,y14dB,E14dB,'*','MarkerSize',3)
plot(x2,yline6dB)
plot(x2,yline14dB,':')
hold off


xlabel('Water-depth (m)')
ylabel('Measured burst length  \DeltaT (s)')
legend('-6 dB', '-14 dB','-6 dB rms','-14 dB rms')
```

C.27   usikkerheit.m (A)

Program that calculates the uncertainty in the coefficients from the linear plot:

```
%Uncertainty calculations and coefficients:
ymeas=y6dB; %y measured
x=x; %x-coordinates
n=4; %number of samples
c=1500; %sound speed in water
m=p6dB(1); %gradient (stigningstall)
b=p6dB(2); %offset
alpha=(m*c)/2
D=c*b    %effective burst length
theta=(acos(1/(alpha+1)))*180/pi %effective angle

for i = 1:n
    ysim=b+m*x(i);
    sum2(i)=(ymeas(i)-ysim)^2;
end

%sum(x(i).^2)
for i = 1:n
    sum3(i)=x(i).^2;
end

%sum(x(i))
for i = 1:n
    sum4(i)=x(i);
end

%Standard deviation y-values
sy=sqrt(sum(sum2)/(n-2));

%Standard deviations for the linear fit coefficients, effective burst
%length and alpha
sm=sy*sqrt(n/(n*sum(sum3)-sum(sum4)^2));
salpha=sqrt((c/2*sm)^2+(m/2*20)^2)

sb=sy*sqrt(sum(sum3)/(n*sum(sum3)-sum(sum4)^2));
sD=sqrt((1500*sb)^2+(b*20)^2)

%standard deviation for the effective angle
stheta=((cos(theta*pi/180))^2/sin(theta*pi/180))*salpha*180/pi
```